High Frequency Ultrasonic Device development for Non-Destructive Post-Irradiation Examination of the RHF Fuel Element

Meriem Chrifi Alaoui

▶ To cite this version:

Meriem Chrifi Alaoui. High Frequency Ultrasonic Device development for Non-Destructive Post-Irradiation Examination of the RHF Fuel Element. Other. Université Montpellier, 2018. English. NNT : 2018MONTS055 . tel-02123936

HAL Id: tel-02123936
https://theses.hal.science/tel-02123936

Submitted on 9 May 2019

HAL is a multi-disciplinary open access archive for the deposit and dissemination of scientific research documents, whether they are published or not. The documents may come from teaching and research institutions in France or abroad, or from public or private research centers.

L'archive ouverte pluridisciplinaire **HAL**, est destinée au dépôt et à la diffusion de documents scientifiques de niveau recherche, publiés ou non, émanant des établissements d'enseignement et de recherche français ou étrangers, des laboratoires publics ou privés.

THÈSE POUR OBTENIR LE GRADE DE DOCTEUR DE L'UNIVERSITE DE MONTPELLIER

En Électronique

École doctorale : Information, Structures, Systèmes

Unité de recherche IES, UMR 5214

High Frequency Ultrasonic Device development for Non-Destructive Post-Irradiation Examination of the RHF Fuel Element

Présentée par Meriem Chrifi Alaoui

Le 20 Novembre 2018

Sous la direction de Gilles DESPAUX et Emmanuel LE CLEZIO

Devant le jury composé de

Ghizlane KHAISSIDI, Maître de conférence-HDR, **LIPI, Université Sidi Mohamed Ben Abdellah, Fes, Maroc**	**Rapporteur**
Lionel HAUMESSER, Maître de conférence-HDR, **GREMAN, Université de Tours, France**	**Rapporteur**
Yoann CALZAVARA, Docteur - Chef de service, **Institut Laue Langevin, Grenoble, France**	**Examinateur**
Philippe COMBETTE, Professeur des universités, **IES, Université de Montpellier, France**	**Examinateur**
John STEVENS, Docteur - Chef de département, **Laboratoire National d'Argonne, Chicago, USA,**	**Membre Invité**
Emmanuel LE CLEZIO, Professeur des universités, **IES, Université de Montpellier, France**	**Directeur de thèse**
Gilles DESPAUX, Professeur des universités, **IES, Université de Montpellier, France**	**Directeur de thèse**

UNIVERSITÉ DE MONTPELLIER

Remerciements

C'est au terme de 3 ans que s'achèvent mes travaux de thèse que je finis avec énormément d'émotion. Nombreuses sont les personnes qui ont contribuées à la réussite de ce travail, je m'excuse de ne pouvoir toutes et tous les citer et je tiens à préciser que les mots qui suivent sont peu devant la reconnaissance et les remerciements que je voudrais exprimer.

Je tiens d'abord à témoigner de toute ma gratitude envers mes deux directeurs de thèse Gilles Despaux et Emmanuel Le Clézio, qui, par leurs vastes expériences et leurs encadrements, ont permis le succès de ce travail.

Gilles, ta présence, ta bonne humeur et tes précieuses explications durant ces trois années m'ont permis d'apprendre et de développer des compétences à tous les niveaux. Tu m'as intégrée dans le monde de la recherche et de l'enseignement avec une constante présence et confiance et tu m'as toujours épaulé de tes conseils motivants, ton partage scientifique et ta joie de vivre, et pour tout cela, je te remercie infiniment.

Emmanuel, je tiens à particulièrement te remercier et t'exprimer ma reconnaissance éternelle pour tout ce que tu as fait pour m'amener vers le bon chemin, toujours dans une très bonne ambiance. Ta générosité et tes inestimables qualités d'écoute, de patience, de pédagogie, de savoir-faire ainsi que ton partage, tant au niveau scientifique qu'au niveau humain, m'ont permis d'avancer et de prendre confiance. Tu as toujours su trouver les mots qu'il faut pour m'expliquer, m'encourager et, à tous moments, me rendre le sourire.

Je voudrais exprimer mes profonds remerciements à Yoann Calzavara pour sa confiance et pour les inestimables précisions qu'il m'a apportées tout au long de ces trois années pour que je puisse m'approprier le sujet du côté industriel. Je te remercie vivement pour ta disponibilité, ta générosité et ta bonne humeur toujours présente, ainsi que pour les multiples thématiques de discussions que l'on a pu aborder.

Pour tout ce que j'ai pu découvrir durant cette fabuleuse aventure, tout le plaisir que j'ai pris à travailler à vos côtés et tout ce que j'ai pu développer avec et grâce à vous trois, simplement et très sincèrement : mille mercis.

Je tiens à vivement remercier Madame Ghizlane Khaissidi et Monsieur Lionel Haumesser qui m'ont fait l'honneur d'être rapporteurs de cette thèse. Madame Ghizlane Khaissidi, je vous remercie vivement pour m'avoir permis de candidater à cette thèse et pour les différents échanges scientifiques qu'on a pu avoir au cours de ces dix dernières années. Monsieur Lionel Haumesser, merci de m'avoir permis d'interagir scientifiquement avec vous sur les différents aspects de ma thèse.

Je voudrais remercier John Stevens, qui, malgré ses différentes responsabilités, a fait le déplacement de Chicago pour faire partie de mon jury de thèse. Merci pour votre disponibilité et pour les différentes thématiques de discussions que l'on a pu partager. I would like to really thank you for being available from Chicago and accepting to be a member of my thesis committee and for the scientific and interesting discussions we have shared.

Je tiens à remercier Philippe Combette d'avoir accepté de présider mon jury de thèse. Vous avez su rendre cette présentation de thèse aussi scientifiquement fructueuse que fortement conviviale.

Je tiens à vivement remercier Olivier Guillemard et Yannick Launay pour leurs contributions dans la conception et la réalisation des différents systèmes mécaniques et dispositifs ultrasonores.

Mes vifs remerciements sont également dédiés à l'équipe de l'Institut Laue Langevin de Grenoble qui témoignent de leurs disponibilités et de leurs hautes contributions pour la réalisation des échantillons et des différentes expérimentations en environnement hostile.

J'exprime ma gratitude envers les doctorantes et doctorants, anciens comme actuels, ainsi que tous les membres de l'équipe pour les discussions scientifiques ainsi que les agréables moments partagés en votre compagnie. Je remercie également tous les membres de l'Institut d'Électronique et des Systèmes pour la convivialité et le partage au sein du laboratoire. Grâce à vous toutes et tous, une ambiance d'échange, de soutien et de savoir-vivre règne dans cet univers et une alarme sonne quand je souhaite sortir ailleurs. Sur cette phrase, je remercie les personnes qui veillent à notre sécurité pour leur présence et compréhension.

J'adresse mes remerciements à Laurent Cortella de l'Institut Arc-Nucléart de Grenoble pour sa compréhension et disponibilité, même en période de vacances. Un grand merci pour avoir permis d'éviter un délai de taille pour l'étude en irradiation. Je remercie également tous les membres de l'Institut Arc-Nucléart avec qui j'ai pu interagir et qui ont veillé au bon déroulement de cette étude à distance.

Je voudrais également remercier toutes les personnes qui m'ont permis d'effectuer ma Mission Complémentaire d'Enseignement et de découvrir l'échange et le partage avec les étudiants. Thomas Delaunay, Emmanuel, Gilles ainsi que toutes les personnes qui se sont chargés de la documentation administrative, je vous remercie vivement pour votre confiance.

Je tiens à exprimer mes remerciements les plus profonds et les plus sincères à tous les membres de ma famille, petite comme grande, ainsi qu'à tous mes amies et amis.

Je commencerai par ma maman chérie, ma plus grande confidente et celle qui ne cesse de chercher et surtout de trouver le meilleur pour moi. Tu me connais et tu sais parfaitement ce qui me fait le plus plaisir. Saches que tu es ma source de raisonnement et de gaîté et tu resteras, comme tu l'as toujours été, et ce pour tous les aspects possibles, mon modèle à vie.

Naturellement, et sur la même longueur d'onde, je ne remercierai jamais assez mon papa chéri pour sa présence, sa confiance et ses encouragements au quotidien. Tu es mon égal, celui à qui je peux demander, et ce à tous moments, tout ce que je désire, et tu seras toujours ma source de motivation, de réconfort continu et de joie de vivre.

Suivra évidemment mon frérot adoré, Hicham, qui me supporte constamment mais qui ne pourrait se passer de ma présence, et d'ailleurs, je l'avoue avec fierté, moi de même. Tu es la source à la fois de rationalité et d'adrénaline de la famille, celui qui connaît parfaitement mon mécanisme de fonctionnement et ma source d'inspiration.

Je tiens à particulièrement remercier mes tantes et cousines, vous êtes mes soeurs et ma bande préférée pour les soirées et le shopping, et mes amies et amis, avec qui j'ai partagé des soirées et des sorties inoubliables.

Merci à toutes et à tous d'être indéfiniment à mes côtés et tout simplement d'exister.

Chacun de vous sur ces remerciements a constamment signé présent pour moi et ma satisfaction a toujours fait partie de vos centres d'intérêts prioritaires. Vous avez été ma source de motivation première et votre fierté constitue mon objectif à l'infini.

Contents

Résumé général **11**

General introduction **21**

1 Context of the project **25**

1.1 Introduction . . . 26
1.2 Nuclear reactors . . . 27
1.2.1 The HPRR . . . 27
1.2.2 Reactors uranium enrichment . . . 29
1.3 Conversion to LEU (Low Enriched Uranium) . . . 29
1.3.1 Conversion into LEU high density fuel of the HPRR . . . 30
1.4 HERACLES Consortium . . . 31
1.4.1 HERACLES program description . . . 31
1.4.2 UMo dispersion fuel behaviour . . . 33
1.5 Plate swelling post-irradiation examination . . . 33
1.5.1 Destructive methods . . . 34
1.5.2 Non-destructive methods . . . 34
1.6 The High Flux Reactor . . . 35
1.6.1 The Reactor and its plant description . . . 35
1.6.2 The fuel element . . . 36
1.6.3 RHF conversion into LEU high density fuel . . . 38
1.6.4 PERSEUS Project . . . 38
1.7 Conclusion . . . 42

2 Ultrasonic device **43**

2.1 Introduction . . . 44
2.2 Ultrasonic device constraints . . . 44
2.3 New ultrasonic device realization . . . 45
2.3.1 Ultrasonic device principle . . . 45
2.3.2 Ultrasonic transducer . . . 47
2.3.3 Mechanical support . . . 53
2.3.4 Ultrasonic device assembly . . . 54
2.3.5 Electronic system . . . 54

2.4 Ultrasonic device positioning . . . 57
2.4.1 Laboratory measurement bench . . . 58
2.4.2 Linear cable sensor . . . 59
2.5 Conclusion . . . 60

3 Distance measurement concept **61**
3.1 Introduction . . . 62
3.2 Time of flight measurement . . . 62
3.2.1 Introduction . . . 62
3.2.2 Time of flight measurement signal processing methods . . . 63
3.2.3 Multiple echoes cross-correlation . . . 64
3.2.4 Time of flight applied measurement concept . . . 65
3.3 Ultrasound velocity measurement . . . 71
3.3.1 Introduction . . . 71
3.3.2 Ultrasound velocity measurement methods . . . 71
3.3.3 Ultrasound velocity measurement method applied . . . 71
3.4 Conclusion . . . 76

4 Proof-of-concept and reproducibility measurements **77**
4.1 Introduction . . . 78
4.2 Inter-plate distance variation measurements . . . 78
4.3 Device structure and transducers parallelism . . . 80
4.3.1 Effect of $\Theta = 1°$ over the distance measurement . . . 81
4.4 Measurement reproducibility study . . . 82
4.4.1 Configuration 1: Optimized transducer 1 alignment. . . . 82
4.4.2 Configuration 2: Optimized transducer 1 alignment with a velocity decrease of a factor of 10. . . . 83
4.4.3 Configuration 3: Optimized transducer 2 alignment. . . . 84
4.4.4 Configuration 4: simultaneous transducers alignment compromise. . . . 85
4.4.5 Configuration 5: Second measurements with simultaneous transducers alignment compromise. . . . 86
4.4.6 Reproducibility measurements conclusion . . . 88
4.5 RHF model inter-plate distance reproducibility measurements . . . 88
4.5.1 Modeling of the device positioning in the RHF element . . . 88
4.5.2 RHF model experiments . . . 90
4.6 Conclusion . . . 92

5 Ultrasonic device resistance under irradiation **93**
5.1 Introduction . . . 94
5.2 Arc-Nucléart irradiator . . . 94
5.2.1 General description of the installation . . . 94
5.2.2 Radioactive sources of gamma irradiation . . . 95

5.2.3 Irradiation cell . . . 96
5.2.4 Dosimetry . . . 97
5.3 Experimental constraints . . . 98
5.4 Experimental set-up . . . 98
5.4.1 Experimental set-up installation . . . 98
5.4.2 Experimental Analyzes . . . 102
5.5 Ultrasonic device analyzes . . . 102
5.5.1 Signal processing . . . 102
5.5.2 Measurement results . . . 103
5.6 Ultrasonic device passive components . . . 112
5.6.1 Visual inspection . . . 113
5.6.2 Microscopic imaging . . . 114
5.6.3 Mechanical properties assessment . . . 115
5.7 Conclusion . . . 116

6 High Flux Reactor experiments **119**
6.1 Introduction . . . 120
6.2 Distance measurement . . . 120
6.2.1 Measurement results . . . 120
6.3 RHF fuel element experiment . . . 121
6.3.1 Experimental set-up . . . 121
6.3.2 Experimental protocol and proof-of-concept . . . 122
6.4 Results and interpretation . . . 130
6.5 Conclusion . . . 133

Conclusion and prospects **135**

Bibliography **139**

Communications **147**

List of figures **155**

List of tables **157**

Abstract **158**

Résumé général

Les réacteurs de recherche jouent un rôle majeur dans de nombreux domaines scientifiques, de la médecine aux énergies nouvelles sans oublier la biologie et la physique fondamentale. Or, la plupart de ces réacteurs utilisent des éléments combustibles dotés d'un enrichissement d'Uranium élevé, typiquement à 93 %. L'utilisation de l'Uranium hautement enrichi constituant un risque important de prolifération, de nombreux programmes internationaux ont été lancés afin de convertir les réacteurs de recherche à l'utilisation de combustibles faiblement enrichis, c'est-à-dire avec un enrichissement inférieur à 19.75 %.

Les Réacteurs de Recherche européens à Haute Performance (HPRR) nécessitent en particulier le développement d'un nouveau type de combustible à haute densité afin de convertir leurs éléments combustibles à un faible enrichissement. Si la sûreté demeure la préoccupation principale, le maintien de leurs performances initiales avec de moindres modifications est très important. Pour cela, le consortium européen HERACLES étudie depuis plusieurs années le développement d'un combustible prometteur à base d'alliage UMo. Des irradiations sont en cours pour qualifier ce nouveau combustible.

Une fois les irradiations terminées, des examinations post-irradiations sont nécessaires à l'étude des phénomènes dévoilant le comportement du combustible. Parmi ces phénomènes, le gonflement des plaques est une source majeure d'interprétation de l'historique d'irradiation. Plusieurs méthodes destructives et non-destructives de contrôle du gonflement sont utilisées en fonction des différentes formes des éléments combustibles des réacteurs. Un exemple d'imagerie destructive de gonflement d'une plaque combustible [1] est présentée sur la figure 1.

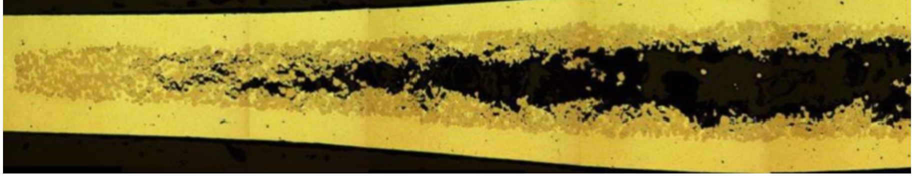

Figure 1: Imagerie d'une plaque combustible dévoilant un gonflement.

Parmi les HPRR intégrés dans le programme HERACLES, le Réacteur à Haut Flux (RHF) de l'Institut Laue Langevin (ILL), doté d'une puissance thermique de 58 MW, produit le flux de neutrons le plus intense au monde à $1.5 * 10^{15}$ n/cm^2/s. Le RHF possède un élément combustible unique composé de 280 plaques combustibles courbées et placées en développante de cercle afin de maintenir une distance constante entre les plaques. Une image de dessus de l'élément combustible du RHF [2] est présenté sur la figure 2.

Figure 2: Image de l'élément combustible du RHF.

Dans le cadre de sa conversion à un combustible faiblement enrichi, l'ILL souhaite développer des systèmes de mesure non-destructifs afin de caractériser son élément combustible prototype après irradiation. Le gonflement des plaques de ce dernier génère des modifications microscopiques de la structure ainsi que la variation de la distance inter-plaques initialement fixée à 1.8 mm. Le suivi de variation de cette distance constitue l'objectif principal du projet PERSEUS en collaboration avec l'Institut d'Électronique et des Systèmes (IES) de l'Université de Montpellier (UM). Il vise ainsi à développer un système de mesure de la distance inter-plaques par méthode ultrasonore hautes fréquences à caractère non-destructif.

Pour la mesure de la distance inter-plaques, le dispositif ultrasonore doit respecter plusieurs contraintes. Premièrement l'élément combustible est placé sous 5 m d'eau. Ensuite, les plaques sont : de forme courbée, disposées en développante de cercle au sein de l'élément combustible et séparées d'une distance nominale fixée à 1.8 mm (voir figure 2). Sachant que la résolution souhaitée est de l'ordre micrométrique pour évaluer un gonflement supposé de 25 μm par canal, l'élément combustible ne doit pas être démantelé. Enfin, à terme, la mesure est réalisée dans un environnement hautement radiatif. De ce fait, soit les éléments du système de mesure doivent présenter une résistance aux radiations, soit l'impact de cet environnement sur la mesure doit être quantifié.

Dans le cadre d'une première thèse, un dispositif ultrasonore a été développé. Destiné à s'introduire dans l'interstice séparant deux plaques, le dispositif est conçu avec les dimensions suivantes : une longueur de 1500 mm, une largeur de 10 mm et une épaisseur de 1 mm. Dans cette épaisseur sont usinées deux cavités à l'extrémité du dispositif. Chaque cavité accueille ainsi un transducteur ultrasonore opérant à des fréquences allant jusqu'à 100 MHz pour obtenir la résolution souhaitée.

L'élément combustible étant placé en piscine de refroidissement suite à l'irradiation, les ondes ultrasonores émises par chaque transducteur sont ainsi transmises dans l'eau et réfléchies sur l'interface eau/plaque combustible. Les signaux réfléchis sont ensuite réceptionnés par chaque même transducteur et acquis par un ensemble de composants électroniques. Un schéma de la composition des transducteurs et un exemple de signal ultrasonore réceptionné sont présentés sur la figure 3.

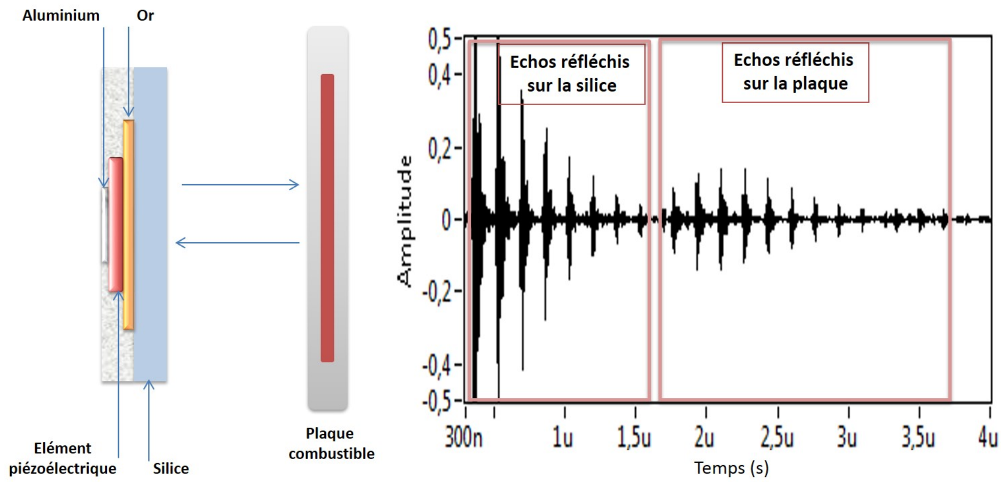

Figure 3: Composition multicouche du transducteur ultrasonore et signal reçu suite à la propagation des ondes jusqu'à l'interface eau/plaque.

Suite à un traitement du signal adapté, les mesures de temps de vol et de vitesse ultrasonore sont alors réalisées via les signaux acquis. Elles permettent ainsi de remonter à la mesure de la distance inter-plaques.

Une expérimentation in-situ a été réalisée sur un élément combustible du RHF. En dépit de la nature fortement irradiée de l'environnement, la qualité des signaux acquis a été suffisante pour assurer une stabilité des estimations de la variation relative de la distance inter-plaques. Ce qui a permis de prouver la faisabilité de la mesure de la distance inter-plaques par méthode ultrasonore hautes fréquences non-destructive.

Néanmoins, plusieurs sources d'optimisation ont pu être identifiées. Premièrement, la mesure du temps de vol est influencée par le positionnement manuel du sabre. En effet, l'insertion des transducteurs dans deux cavités induit leur non-alignement. Ceci implique une difficulté de réception simultanée des signaux par les deux transducteurs. Ensuite, ces intégrations en cavités séparées ne permettent pas d'identifier précisément la distance inter-transducteurs. De plus, la position verticale du dispositif en élément combustible n'est pas déterminée et donc la zone de la plaque analysée est inconnue. Ces éléments influencent la précision de la mesure de la distance inter-plaques et ont ainsi généré la nécessité d'une seconde thèse.

Cette nouvelle thèse a eu pour principal objectif l'optimisation du dispositif ultrasonore à des fins de fiabilité et de reproductibilité de mesures de la distance inter-plaques. C'est ainsi qu'en premier lieu, une analyse du dispositif en fonction des résultats précédents a été réalisée et a aboutie à son optimisation le long de la chaîne d'acquisition. Ensuite, son positionnement a été étudié permettant des mesures de reproductibilité. La résolution recherchée a, par la suite, été optimisée via l'amélioration du traitement du signal. D'autre part, l'environnement nucléaire a été étudié. Ainsi, une expérimentation de résistivité de plusieurs dispositifs sous irradiation à l'Institut Arc-Nucléart de Grenoble et une expérimentation de mesure de distance inter-plaques au sein du RHF ont été réalisées avec succès.

L'analyse de la conception et de la réalisation du dispositif ultrasonore en fonction des résultats antécédents a permis d'aboutir à une innovation majeure de la structure ultrasonore fournissant ainsi un nouveau prototype du dispositif. En effet, les transducteurs ultrasonores ont été disposés sur un seul et même support, unifiant ainsi la cavité d'intégration. Cette innovation apporte de nombreux avantages. Entre autres, la distance séparant les transducteurs est précisément déterminée, le parallélisme inter-transducteurs est optimisé, et leur alignement avec les plaques combustibles est optimisé.

Ensuite, la modélisation de la composition multicouche a été utilisée afin de fixer la gamme de fréquence de résonance des transducteurs ultrasonores adéquate dans le cadre de l'amélioration de la résolution de mesure. L'impact de chaque composant du système électronique sur le signal acquis a, par la suite, été étudié. Ce qui a permis une identification de la nature des échos et une analyse approfondie du signal ultrasonore. Sur la figure 4 sont présentés : une image du dispositif de mesure comprenant la nouvelle structure, et un signal ultrasonore réceptionné. Ce dernier permet de distinguer les échos électriques (en rouge) des échos acoustiques (en bleu).

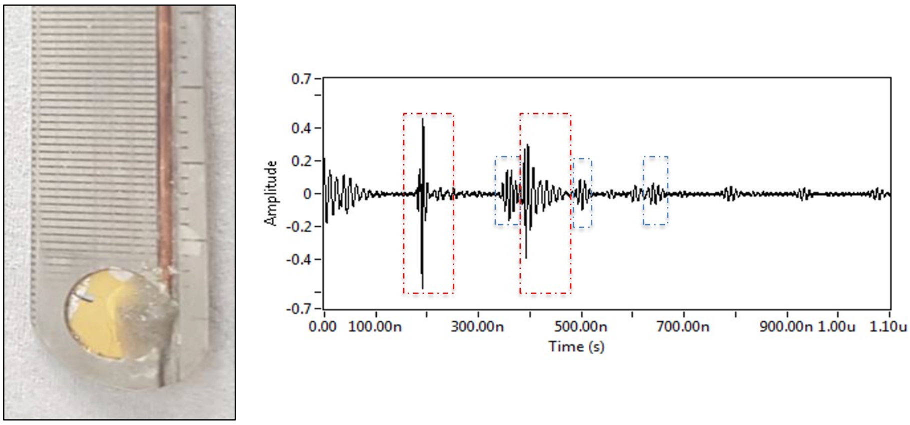

Figure 4: Image du sabre et signal ultrasonore à échos électriques (en rouge) et échos acoustiques (en bleu).

Ultérieurement, un banc de mesure motorisé a été étudié et monté. 4 axes de liberté du dispositif ultrasonore ont été motorisés et 2 axes sont contrôlés manuellement à l'échelle micrométrique. De plus, un capteur linéaire à câble destiné au suivi de la position verticale du dispositif ultrasonore a été introduit. Ce banc de mesure est présenté sur la figure 5.

Figure 5: Banc de mesure.

L'étape suivante concerne le traitement du signal. En effet, la mesure de la distance inter-plaques se base sur la mesure du temps de vol et de la vitesse ultrasonore, via les signaux acquis.

La mesure du temps de vol repose sur la corrélation croisée entre un signal de référence, comprenant la signature acoustique du transducteur, et le signal réfléchi, comprenant deux séries, notamment la signature acoustique et la réflexion de la complémentaire de cette dernière sur l'interface eau/plaque. Afin d'améliorer cette mesure, la sélection des signaux a été conditionnée par la mesure de l'énergie du signal, et une méthode optimisée de soustraction inter-signaux a été introduite. Un résultat de cette soustraction optimisée sur un signal dévoilant un recouvrement des séries est présenté sur la figure 6.

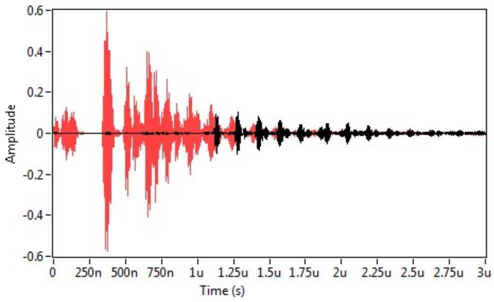

Figure 6: Superposition des signaux avant (rouge) et après (noir) soustraction optimisée de référence.

De plus, l'identification de la nature des échos, précédemment introduite, a permis de développer une méthode de vérification de la validité du résultat de la corrélation via la superposition des deux séries. Un exemple de vérification de corrélation est présenté sur la figure 7.

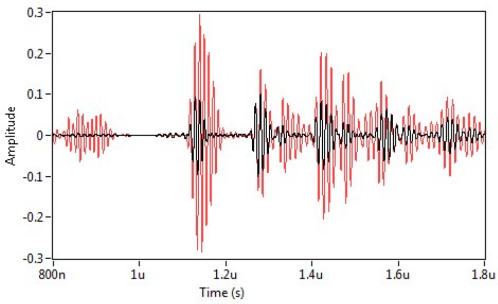

Figure 7: Résultat de corrélation via le positionnement du signal de référence (rouge) à l'emplacement de détection de la seconde série (noir).

D'autre part, pour la mesure de la vitesse ultrasonore le même dispositif est employé. En effet, la vitesse ultrasonore dépend de l'évaluation de la température de l'eau. Celle-ci est évaluée via la variation de la fréquence de résonance du transducteur. C'est ainsi que la mesure de la vitesse ultrasonore s'est améliorée de part l'identification de la nature des échos, permettant ainsi le suivi adéquat de la fréquence de résonance du transducteur.

Ces optimisations ont été testées sur des éléments représentatifs de la distance inter-plaques. Dans un premier temps, une mesure de distance a été réalisée avec succès sur un élément en titane usiné par électro-érosion dans les locaux de l'ILL et comportant des pas de 50 μm. Ensuite, la reproductibilité des mesures a été prouvée via le déploiement de la méthode sur un élément en silice doté d'une distance entre faces de 1800 μm $\pm$ 10 μm. Enfin, le dispositif ultrasonore a été testé sur un modèle du RHF à disposition au laboratoire. Un exemple de résultat de mesures de reproductibilité sur une zone de 1 cm de l'élément en silice est présenté sur la figure 8.

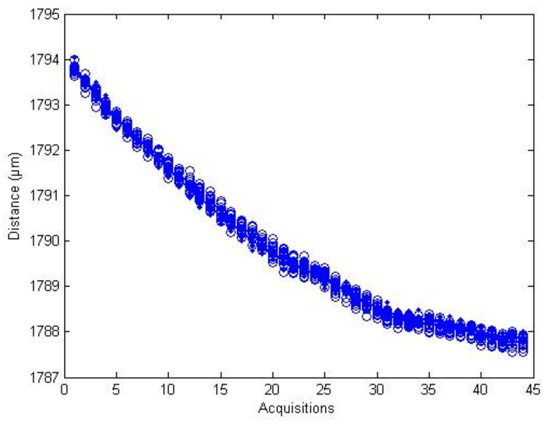

Figure 8: Résultat de 10 mesures de reproductibilité sur l'élément en silice de 1800 μm $\pm$ 10 μm d'interstice.

Les résultats présentés sur la figure 8 indiquent que l'épaisseur du canal d'eau décroit de manière quasi-linéaire. Sur la zone étudiée, la valeur moyenne de l'épaisseur est identifiée égale à 1789.9 μm, avec un écart-type de 1.8 μm et une variation globale sur les 1 cm de 5.9 μm. Pour chaque position, les mesures réalisées lors des descentes et des montées de la sonde se situent dans un intervalle de 500 nm maximum.

Toutes les expériences réalisées sur les différents éléments ont permis de prouver, d'une part, la faisabilité de la mesure de la distance inter-plaques via le nouveau dispositif ultrasonore et, d'autre part, la fiabilisation de cette mesure via la reproductibilité des résultats étudiée grâce au banc de mesure avec une résolution de 500 nm.

A ce stade, la contrainte primordiale à étudier est l'environnement hautement radiatif auquel sont soumis les composants du dispositif ultrasonore. C'est ainsi que la résistance de ce dernier aux irradiations a été caractérisée via une expérimentation de reproductibilité. Pour cela, 12 transducteurs ultrasonores dans une gamme de fréquence allant de 38 à 160 MHz et des éléments des composants du dispositif ultrasonore ont été soumis à une irradiation avec une dose de 3500 kGy durant 4 mois au sein de la cellule d'irradiation de l'Institut Arc-Nucléart de Grenoble. Cette expérimentation a nécessité un ensemble de composants électroniques contrôlé par un programme d'acquisition et d'enregistrement adéquat. Ces composants ont été disposés hors de la cellule d'irradiation.

Une image des dispositifs et des éléments disposés en cellule d'irradiation est présentée sur la figure 9 (a) et le système électronique de suivi disposé or de la cellule est présenté sur la figure 9 (b).

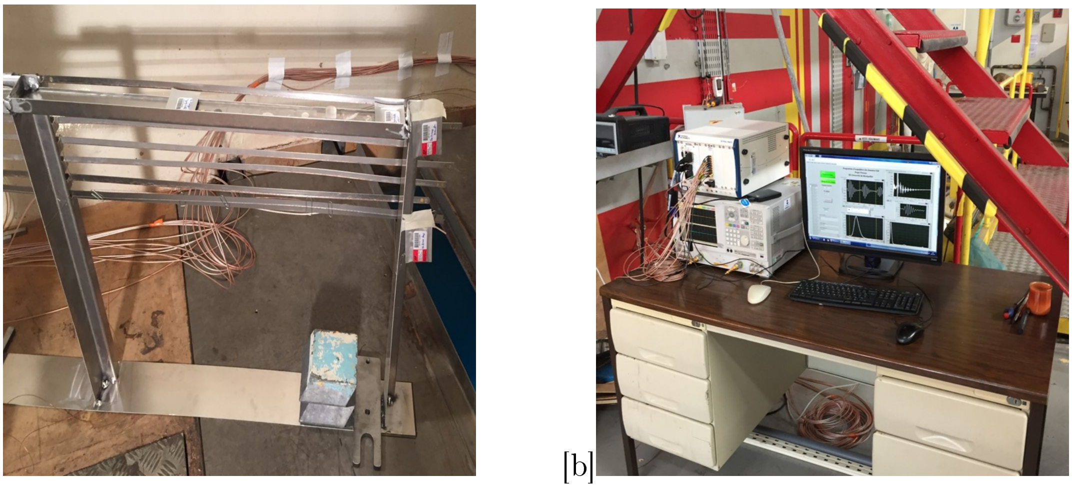

[a] [b]

Figure 9: (a) Installation des dispositifs et ses composants en cellule d'irradiation, (b) Composants électroniques pour le suivi des dispositifs sous irradiation.

La récupération des données ainsi que le suivi en continu et en temps réel de l'évolution des paramètres des transducteurs ont été réalisés lors de cette expérimentation. Celle-ci a permis de démontrer la résistivité et la stabilité du dispositif ultrasonore, de ses composants et des paramètres influençant la mesure de la distance inter-plaques sous flux radiatif.

Toujours dans le cadre de l'environnent radiatif, le traitement du signal développé a été testé sur une série de mesures réalisée lors d'une expérimentation précédente. Des valeurs définies, autrefois, comme aberrantes ont pu être rectifiées et ont permis une identification adéquate de la distance inter-plaques. Ce qui confirme l'optimisation du traitement du signal via les nouvelles étapes introduites et ses capacités à extraire des informations initialement inconnues.

Enfin, une expérimentation pour la mesure de la distance inter-plaques au sein de l'élément combustible du RHF via le nouveau dispositif ultrasonore a été réalisée et le traitement du signal optimisé a été appliqué. Une image de l'insertion du dispositif ultrasonore entre les plaques d'un élément combustible est présentée sur la figure 10 et les résultats de mesure de distance inter-plaques en fonction de la position verticale du dispositif sont présentés sur le graphe de la même figure.

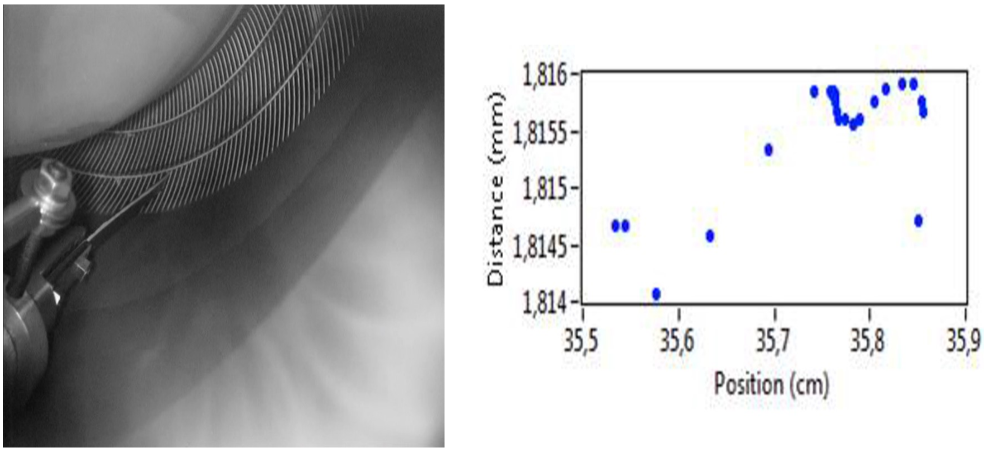

Figure 10: Image du sabre introduit entre deux plaques combustibles et graphe de mesure de distance en fonction de la position verticale.

Les résultats du graphe de la figure 10 démontrent une stabilité de mesure de la distance inter-plaques via le dispositif ultrasonore. Ainsi, une valeur moyenne de la mesure de la distance inter-plaques est estimée à $d = 1.815$ mm avec un écart-type de $\sigma = \pm\ 1\ \mu$m.

Ainsi, le nouveau dispositif ultrasonore a permis d'augmenter la fiabilité des mesures de distance inter-plaques et de température tout en effectuant le suivi de la position verticale du dispositif ultrasonore au sein de l'élément combustible. Ces mesures ont permis de dévoiler une précision sur la mesure de la variation relative de l'épaisseur du canal d'eau avec une résolution de 1 μm.

Plusieurs perspectives sont envisagées suite à ces optimisations via le nouveau dispositif ultrasonore. Premièrement, une prochaine campagne de mesure de distance inter-plaques au sein du RHF via le nouveau dispositif ultrasonore et de son banc de mesure aura pour but d'effectuer un scan de la variation de la distance inter-plaques sur la hauteur globale de l'élément combustible du RHF. Ce qui permettra éventuellement d'identifier les zones de gonflement des plaques.

Ensuite, les sources de cet éventuel gonflement seront explorées. En effet, une modélisation des transducteurs prenant en compte l'éventuelle existence d'une couche d'oxyde est en cours d'étude afin d'analyser son impact sur le signal ultrasonore reçu et de promouvoir les paramètres à développer et les compétences à déployer sur le dispositif ultrasonore.

Par la suite, l'intégration de transducteurs focalisés permettra d'explorer les possibilités d'extraire des informations en profondeur et d'utiliser le dispositif afin de remonter à la composition interne et in fine globale de la plaque combustible.

Enfin, le dispositif ultrasonore est destiné, à terme, à pouvoir caractériser l'ensemble des plaques de l'élément combustible du RHF. C'est ainsi qu'un historique d'irradiation globale d'un nouveau combustible pourra être décrit par méthode ultrasonore non-destructive.

De plus, compte-tenu des dimensions actuelles et prochaines du dispositif, celui-ci pourra facilement être intégré dans d'autres éléments combustibles et utilisé pour la caractérisation de leur irradiation.

General introduction

The nuclear reactors are nowadays extensively employed all around the world for either civilian applications such as energy production or research activities in various domains such as medical investigations. Mainly based on the fission reaction of ^{235}U isotope, a high amount of this latter element is needed, attaining 93 % of the fuel composition. Consequently, High Enriched Uranium (HEU) is used worldwide. Proliferation concerns about the HEU use have recently motivated national and international programs to replace HEU with Low Enriched Uranium (LEU). It implies a fuel type including an amount of ^{235}U isotope limited to 19.75 %, thus eliminating the proliferation risks [3]. Numerous fuel candidates are then under study in function of each nuclear reactor specifications to maintain the initial objectives.

A qualification process is necessary to validate each selected candidate. In this view, a post-irradiation examination of a LEU fuel element must be undertaken [4]. Several irradiation phenomena are then considered. Among them, the fuel swelling consists in a highly investigated phenomenon and is considered as an irradiation performance indicator. In this case, destructive examination methods are available and have widely been employed. These methods include: scanning electron microscopy (SEM) [5], electron-probe micro-analysis (EPMA) [6], optical microscopy (OM) [7], X-ray diffraction [8], etc. They have contributed to the irradiation monitoring and analysis. However, such methods are extremely costly and do not allow the element reuse. On the other hand, non-destructive methods are also employed. Among others, the main useful non-destructive techniques are: visual inspection [9], gamma-ray spectrometry [10], neutron radiography [11], Bench fOr Non-destructive Analyses of Plate And Rod Type fuel Elements (BONAPARTE) [12], etc. Each type of methods is complementary, allowing the understanding of the fuel behavior and its further development according to its performance.

Based in Grenoble (France), the Institute Laue-Langevin (ILL) is an international research organism [13] that provides the most intense neutron flux through a High Flux Reactor (RHF). Integrated in the LEU conversion program: Reduced Enrichment for Research and Test Reactors program (RERTR), the ILL has studied, under a collaboration with the Argonne National Laboratory (ANL), the LEU designs for the RHF conversion in a way to maintain the performances of the HEU. After conversion feasibility studies, a promising candidate has been selected. In particular, the RHF fuel element is constituted of involute shape plates with specific dimensions including a constant inter-plate distance. The selected candidate for the RHF allows a fuel amount increase, maintaining the same external plate dimensions [14]. In order to investigate the RHF fuel plate swelling, the methods mentioned above are clearly applicable. However, in both cases, the fuel element structure is dismantled, at least for the fuel plate removing.

Non-destructive testing of the fuel element is of high interest, especially through its great advantages such as reduced cost, improved security, possible element reuse and so on. As one of the main domains of the industrial community, ultrasonic waves can clearly carry qualitative and quantitative information about the fuel element structure irradiation. In this view, an innovative non-destructive ultrasonic method has been proposed in the framework of the PERSEUS project for Post-Examination of Reactor high flux Single Element with Ultra-Sounds under a collaboration between the Institute Laue Langevin (ILL) and the Institute of Electronics and Systems (IES) of Montpellier University (UM). The project objective consists in the development of a non-destructive high frequency ultrasonic device dedicated to the measurement of the swelling phenomenon of the fuel plates.

At the fuel element conception, the plates are disposed assuming a constant separating distance fixed at 1.8 mm. After irradiation, the fuel plates demonstrate swelling inducing micrometric modifications of the inter-plate distance. The post-irradiation monitoring of this distance will consequently provide information about the fuel element irradiation history. To address this issue, the PERSEUS device is manufactured with two high frequency ultrasonic transducers, based on the pulse-echo method, and developed respecting the High Flux Reactor fuel element access constraints. Indeed, it needs to be long enough to attain the fuel element placed under 5 m of water, thin enough to be introduced in the plates' separating interstice and resoluted enough to evaluate distance micrometric modifications.

In the early stages of the project, a first thesis has allowed the conception of the high frequency ultrasonic device according to the experimental constraints. An electronic system was also developed for the signal acquisition and processing to allow the distance measurements. It was finally tested for inter-fuel-plate distance evaluation. The proof-of-concept has then been achieved through two successful experiments allowing the estimation of both inter-plate distance and cooling water temperature. These experiments have however allowed the determination of several flaws of the first device prototype. Consequently, to optimize the first ultrasonic device reliability and measurement resolution, a second thesis was set-up to analyze each component of the measurement chain and finally leads to a new ultrasonic device prototype. The realization and testing results of this second device are presented in the current document.

Chapters' overview

The High Flux Reactor fuel element, dedicated to research activities, is composed of separated fuel plates. After an irradiation cycle, the plates demonstrate swelling, inducing a modification of the initial fixed inter-plate distance. The swelling phenomenon needs to be evaluated according to the fuel type in order to analyze a LEU conversion ability. A high frequency ultrasonic device was developed to estimate the inter-plate distance and its testing demonstrated its proof-of-concept. Its optimization according an experimental feedback is realized through the second thesis. This latter is here composed of two parts. While the first one deals with the complete characterization and optimization of the ultrasonic device at the laboratory through the first four chapters, the second part is constituted of the fifth and sixth chapters displaying the ultrasonic device testing under the experimental conditions. An overview over all chapters is here presented.

In the first chapter, the nuclear reactors' concept and the principle components are first presented. Then, the conversion to LEU objective is developed through the conditions to be fulfilled and the fuel candidates. For this, several programs were established, including the HERACLES program: the European Reactors' conversion program. A main fuel behavior revealed during the conversion program HERACLES is the fuel plate swelling. Its examination methods are then displayed. In this view, an innovative method was proposed through the PERSEUS project, through a collaboration between the Institute Laue-Langevin (ILL) and the Institute of Electronics and Systems (IES) of Montpellier University (UM). It consists in the post-irradiation measurement of the initially fixed inter-fuel-plate distance through the development of a non-destructive high frequency ultrasonic device. For this, the ILL High Flux Reactor and its fuel element are described, thus displaying the device experimental constraints. Then, the project first thesis feedback is presented, leading to the objectives' description of the project second thesis.

The second chapter describes in details the new high frequency ultrasonic device prototype. First, the experimental constraints are briefly reminded. After that, the modification advances in comparison with the first ultrasonic device and facing the initial measurement flaws are displayed. The ultrasonic device is a combination of ultrasonic components, a mechanical part and electronic instruments. Each component of this measurement chain is discussed according to its parameters in the objective of a micrometric distance measurement resolution. Then, a motorized measurement bench is discussed in a way to identify the prominent axes for the device positioning, according to the inter-faces distance estimation. Finally, a linear cable sensor is added to the measurement bench, allowing the device vertical position monitoring. This position is then matched with the distance measurement, enabling samples' characterization.

The third chapter deals with the distance measurement concept. Based on the pulse-echo method, two elements are then needed: the time of flight and the ultrasound velocity. An overview of both parameters' measurement methods are discussed. Then, the methods applied in the current case are developed. Indeed, the signal processing steps and advances are illustrated and justified.

After that, in the fourth chapter, the distance measurement concept is applied in the laboratory on three representative samples. The first one implies abrupt distance variations and allows the verification of the device ability to measure important distance variations. The second sample is representative of the nominal inter-plate distance value at 1.8 mm and the third one consists in a model of the fuel element to be characterized. On these samples, transducers' parallelism is analyzed and reproducibility distance measurements are achieved.

After the laboratory characterization of the new ultrasonic device, it was tested in the radiative environment through two different experiments. The first experiment was realized in order to evaluate the ultrasonic transducers' resistivity under irradiation and the second experiment allowed inter-plate distance estimations in the RHF fuel element.

In the fifth chapter, a radiation impact on the device reproducibility experiment realized in the Arc-Nucleart Institute is developed. First, the Arc-Nucleart Institute and installation are presented. Then, the experimental constraints for a continuous distant monitoring and the pre-irradiation characteristics of the 12 tested ultrasonic transducers and the device components are displayed. Indeed, 4 months of irradiation were necessary to expose the transducers and device components to a 3500 kGray irradiation. A continuous monitoring of the main parameters influencing the inter-plate distance estimation is then realized. The post-irradiation results are displayed and the radiation impact on the ultrasonic device is finally discussed.

In the sixth chapter, two elements are discussed. First, the advanced signal processing steps developed in the third chapter are applied to experimental data acquired on the ILL High Flux Reactor fuel element. Consequently, its modifications over the inter-fuel-plate distance measurement results are observed and analyzed. Moreover, an experiment realized in a fuel element of the RHF is exposed. A vertical position monitoring device was then introduced and the new ultrasonic device was tested. The full experimental protocol and proof-of-concept are displayed and the distance measurement results employing the new signal processing are discussed.

Chapter 1

Context of the project

Contents

1.1 Introduction **26**

1.2 Nuclear reactors **27**

1.2.1 The HPRR 27

1.2.2 Reactors uranium enrichment 29

1.3 Conversion to LEU (Low Enriched Uranium) **29**

1.3.1 Conversion into LEU high density fuel of the HPRR . . . 30

1.4 HERACLES Consortium **31**

1.4.1 HERACLES program description 31

1.4.2 UMo dispersion fuel behaviour 33

1.5 Plate swelling post-irradiation examination **33**

1.5.1 Destructive methods 34

1.5.2 Non-destructive methods 34

1.6 The High Flux Reactor **35**

1.6.1 The Reactor and its plant description 35

1.6.2 The fuel element 36

1.6.3 RHF conversion into LEU high density fuel 38

1.6.4 PERSEUS Project 38

1.7 Conclusion **42**

1.1 Introduction

Nowadays, radioisotopes highly contribute to save hundreds of lives [4]. Their production constitutes one of the multitudes outstanding services provided by the European High Performance Research Reactors (HPRR). Several problematics are then explored and improved such as the development of new materials, the engineering solutions for energy, automative, computational and environmental domains and so on. In particular, the HPRR are concerned by nuclear proliferation risks. Consequently, they have joined in an international project so as to reduce the enrichment of their fuels [15] [16]. The main objective is to remove Highly Enriched Uranium (HEU) fuel from the civil nuclear fuel cycle as far as reasonable.

Most of the HPRR are currently using HEU bored fuels made of aluminide (UAl_x) or silicide (U_3Si_2) dispersed in a pure Al matrix. Converting them to LEU is challenging, assuming that the conversion should achieve the initial fuels' performance or with minor losses [17] [18]. In fact, a minimum increase of the cores' fuel load of a factor 5 or more could be expected. Thus, a reasonable solution could be to develop a fuel material with a higher Uranium density. The UMo alloy is one of the most promising candidates and is being investigated by the HERACLES fuel development group.

The conversion program includes several steps in order to qualify a developed fuel candidate. For this, the Post Irradiation Examination (PIE) of the new fuel element is required. While destructive PIE methods are commonly employed, the development of non-destructive (ND) PIE tools appeared to be more adapted to the ILL needs and expectations, the ILL fuel element having a particular complex configuration. Thus, the ILL has launched a collaboration 6 years ago with the Institute of Electronics and Systems (IES) of Montpellier University (UM) through the PERSEUS Project, for Post Examination of the RHF Single Element with Ultra-Sounds, involved in the HERACLES program.

In this first chapter, a general description of nuclear reactors' components and process are exposed. As the deep problematic of this thesis is the ND PIE of HPRR LEU fuel elements, the conversion of HPRR to LEU is discussed thereafter and followed by the HERACLES program development. The fuel behaviour PIE methods are then briefly presented. One of the main fuel behaviour phenomena is the fuel swelling. For its investigation, the PERSEUS Project non-destructive ultrasonic device has already proved its measurement feasibility in the RHF fuel element through a first thesis. The RHF installation and fuel element are presented and followed by a summary of the first thesis feedback [19] [20]. This latter leads to the project second thesis problematic determination further exposed.

1.2 Nuclear reactors

1.2.1 The HPRR

A nuclear reactor is a combined structure made to initiate, moderate and control a nuclear fuel chain reaction. Two categories of nuclear reactors are distinguished:

- nuclear power reactors: Their primary purpose is to employ the released energy as heat for electric power generation [21].
- nuclear research reactors (RR): they are usually under the control of a research organism. The primary objective of RR is to provide a neutron source for several purposes such as medical diagnosis and therapy, testing materials and conducting basic research [22], [23], [24], [25]. This nuclear reactor category is the main environment of study for this project, in particular the High Performance Research Reactors (HPRR).

The major steps of the nuclear reaction are presented in the following and an example of the entire installation of a HPRR is presented in figure 1.1 [13].

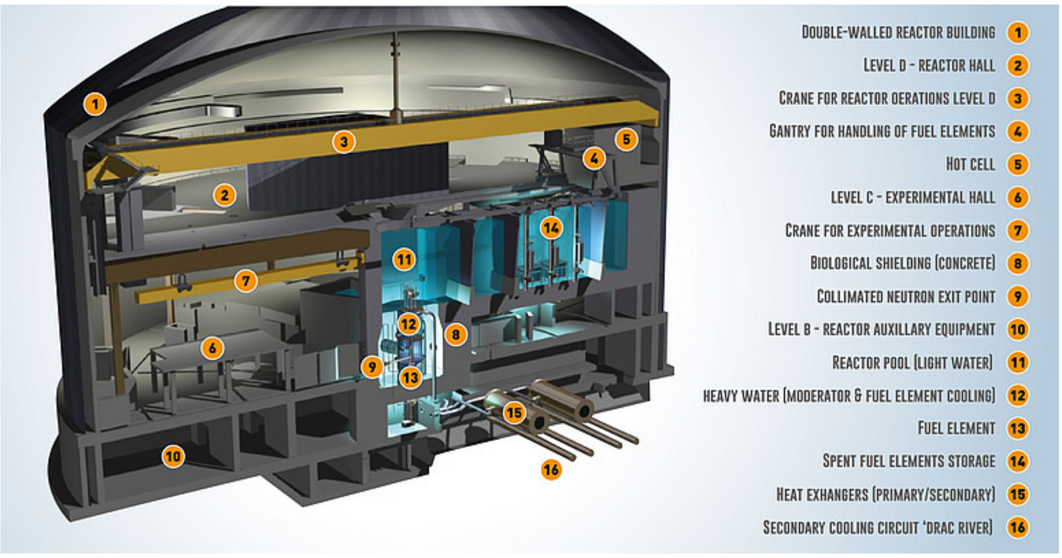

Figure 1.1: Scheme of the High Flux Reactor installation of the Institute Laue Langevin of Grenoble in France.

The nuclear reactor process is based on the fission reaction. It is a nuclear reaction in which the nucleus of a fuel atom splits in two parts after its collision with a first generated neutron. The fission process thus releases a large amount of energy and 2 or 3 free neutrons. The fission principle is represented in figure 1.2.

Energy and neutrons are generated in a fuel container and surrounded by a moderator. This latter allows to slow down the neutrons. Consequently, they are captured

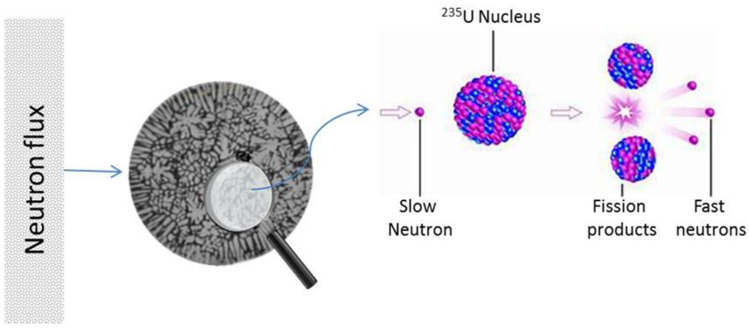

Figure 1.2: Schematic overview of the neutron capture by a ^{235} U nucleus [26].

by another atom. Indeed, each neutron produces a new fission, hence creating the chain reaction.

In order for the chain reaction not to increase indefinitely, a neutron absorbing material, such as boron, in the form of control rods is employed. The reactor can then be controlled by introducing or removing these bars into the reactor core.

Most of the times, the fuel is made of dispersed particles enclosed in a curved or flat metal matrix, generally made of pure aluminum. An assembly of several matrices constitutes a fuel element which may have various configurations, most of them being unique. Examples of plate assemblies are displayed on figure 1.3.

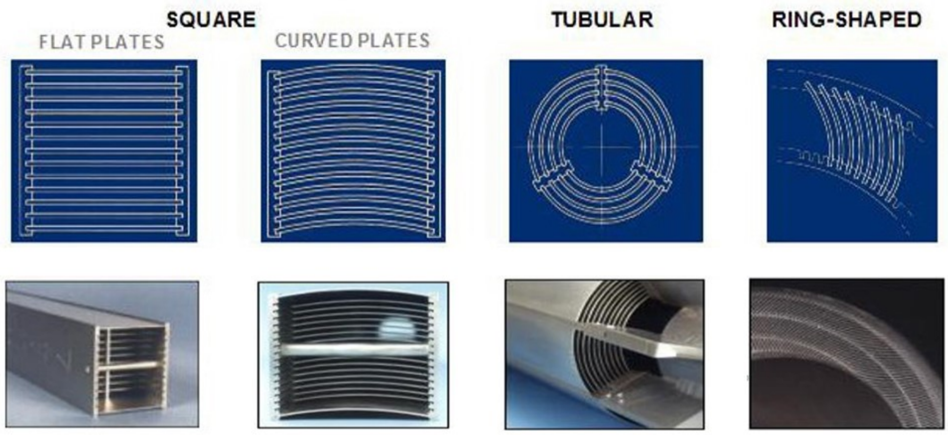

Figure 1.3: Curved and flat fuel plate assemblies [27].

Most of HPRR are plate-type reactors, with a large variety of fuel configurations (one or several elements, curvature, material ...) [28] [27]. They generally employ highly enriched uranium for their core.

1.2.2 Reactors uranium enrichment

Uranium found in nature is composed of two main isotopes, ^{235}U and ^{238}U. In nuclear reactors, the energy and neutrons are generated from the fission of the ^{235}U isotope, the main fissile isotope of uranium.

Natural uranium contains 0.7 % of the ^{235}U isotope. Most of the remaining 99.3 % is made of ^{238}U isotope which does not significantly contribute to nuclear fission process for reactors using thermal neutrons. Enriching uranium means increasing the ratio of ^{235}U isotope relatively to the ^{238}U isotope typically by isotope separation physical process [29].

During the second half of the previous century, research reactors showed a considerable expansion over the world. Either the United Stated or the USSR provided significant amount of Highly Enriched Uranium (HEU) to support these experimental reactors. The uranium enrichment attained an amount of 93 % of ^{235}U in order to maximize the neutron flux, constituting the essential characteristic of experimental reactors.

The high enrichment induces proliferation risks such as misemployment or theft. The International Atomic Energy Agency (IAEA) evaluated the difficulty of the construction of a nuclear weapon or an explosive device in function of the enrichment rate. Thus, highly enriched uranium (HEU) and low-enriched uranium (LEU) have been introduced, considering this latter as enriched uranium containing less than 19.75 % of the ^{235}U isotope [3].

In order to reduce the proliferation risks, the United States established in 1978 the program Reduced Enrichment for Research and Test Reactors (RERTR). In the same purpose, the Nuclear Security Summit (NSS), held in 2010, focuses on improving the safeguard weapons-grade plutonium and uranium while the Research Reactor Fuel Management conference (RRFM), initiated in 1997 by the European Nuclear Society (ENS), aims to promote advances in peaceful uses of nuclear energy. A common objective is the conversion of Research Reactors from HEU to LEU. The conversion programs imply the investigation of numerous further discussed phenomena.

1.3 Conversion to LEU (Low Enriched Uranium)

The conversion of HPRR to LEU [26] requires specific conditions. First, new fuel safety margins and reliability should be comparable to those of the existing design based on HEU. Moreover, only limited losses of the reactor performances and marginal increases of operational costs can be accepted.

Most of time, a mere replacement of the HEU by LEU is not possible because of the reactors performance losses that may be dramatic, especially for the HPRR. One conversion solution could thus be to increase the amount of fuel in a fuel element. This can be achieved by increasing either (1) the volume occupied by the fuel or (2) the fuel density.

The first option requires to explore whether the fuel assembly geometry can be modified to increase the available fuel volume, e.g. using thicker plates, larger plates, more plates per assembly, etc. Reactor operators and safety authorities will only endorse this option if the modifications are minor and do not affect the safety margins of reactor operation.

Under the second option, two solutions can be proposed:

- Increasing the volume fraction of fuel compound in a dispersion fuel,
- Introducing or developing a different fuel compound with a proportional increased Uranium density for use in a dispersed fuel,

All Research Reactors that required uranium densities lower than the technological limit have already converted. For the others, conversion programs are handling the development and qualification of high density LEU fuels.

1.3.1 Conversion into LEU high density fuel of the HPRR

LEU high density fuel types

In order to reach the desired power density of the fuel element with LEU, an increase of the fuel density remains necessary. In this view, two types of fuel are being considered:

- Monolithic fuel: it is composed of an uranium-containing alloy foil (fuel foil) surrounded by a cladding. The density of a fuel foil of a particular alloy is fixed by the alloy composition. Consequently, to increase the uranium mass in a monolithic fuel plate, the fuel foil thickness must be increased. A cross section scheme of a monolithic fuel plate is provided in figure 1.4 (a).

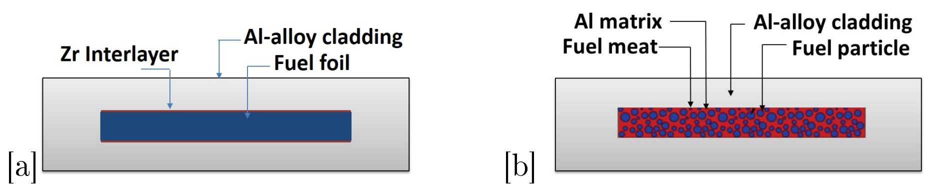

Figure 1.4: (a) Monolithic Fuel Cross-section, (b) Dispersion Fuel Cross-section.

- Dispersed fuel: the fuel meat is made of particles of an uranium-containing compound or alloy. These particles are dispersed within a metallic matrix. The uranium density can be increased by selecting particles with higher uranium density or by increasing the volume fraction of uranium-containing particles within the fuel meat. A cross section scheme of a dispersion fuel plate is provided in the figure 1.4 (b) [30].

Both types were experimented over the years to develop high density fuel. Some candidates qualification results are presented in the following paragraph.

LEU high density fuel candidates

In the 1980's, the high density fuel development studies [26] were mainly on the uranium silicides such as U_3Si [31]. After experiments, only UAl_x and U_3Si_2 proved to remain stable up to high fission densities. The U_3Si_2 dispersion fuel was further evaluated and consequently plate fuels could be fabricated with U_3Si_2/Al dispersion compacts with uranium loadings up to 4.8 g/cm^3 [32], [33].

For HPRR [15], it was not possible to manufacture the fuel plates using the U_3Si_2 with a density of uranium sufficient to avoid the performance losses associated with the initial qualified fuel configurations. The development of a new fuel, based on a metallic uranium-molybdenum alloy (UMo) with very high density was initiated nearly twenty years ago. In this view, the goal of establishing UMo as an accepted and approved standard fuel for HPRR is much nearer but still a couple of steps away. Consequently, it was chosen for the HERACLES European Reactors conversion program study, developed in section 1.4.

1.4 HERACLES Consortium

In the framework of the European HERACLES Consortium program (Highly enriched European Reactor Action for their Conversion into Lower Enriched Solution), the UMo candidate is being developed among other options like the high loaded U_3Si_2.

1.4.1 HERACLES program description

The HERACLES program was launched in 2013, when CEA (Commissariat à l'énergie atomique), CERCA (Compagnie pour l'Etude et la Réalisation de Combustibles Atomiques), ILL (Institut Laue Langevin), SCK-CEN (Dutch: Studiecentrum voor Kernenergie; French: Centre d'Étude de l'énergie Nucléaire) and TUM (The Technische Universität München, a research university in Munich) have teamed-up to optimally share experience and equipment. The U.S./DoE (Department of Energy) is a partner of the HERACLES program.

The HERACLES program aims to improve the understanding of the fuel irradiation behavior [30]. It consequently consists in the main foundation for the manufacturing/industrialization process planning. Concerning UMo, two fuel types are under study:

- Monolithic UMo fuel: it consists in metallic UMo foils with a uranium density of 15.5 gU/cm^3. The U.S. reactors are developping this LEU fuel candidate.
- UMo dispersion fuel: it is a UMo alloy dispersed in an Al matrix with uranium densities up to 8.5 gU/cm^3. This LEU fuel is developed for the RHF, BR2 and JHR2 european reactors conversion.

The manufacturing challenges concern both the fuel types' production process and the plate manufacturing. In this view, the main objectives of the program are:

- Irradiation test technology and analysis tools development,
- Irradiation test realization,
- Post-Irradiation Examinations (PIE) performance.

The validation of a LEU fuel conversion is directly related to its irradiation performance. This performance is manifested through the fuel behavior after the step of PIE performance, naturally following the fuel irradiation testing. The HERACLES general program scheme is presented in figure 1.5.

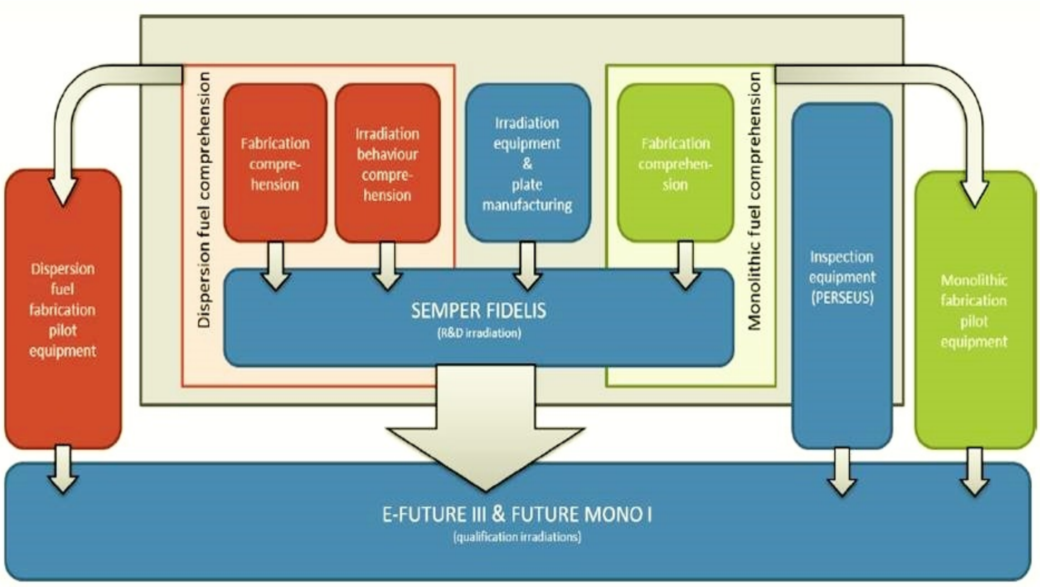

Figure 1.5: Irradiation comprehension phase steps of the HERACLES program.

The post-irradiation fuel behaviour of UMo dispersion fuel, the dispersion fuel dedicated to the European Research reactors, is presented hereafter.

1.4.2 UMo dispersion fuel behaviour

Fission reactions produce a large number of atoms called fission products. Approximately 25 % of these fission products are xenon or krypton gas atoms [34]. Over time, these atoms coalesce into bubbles resulting in swelling phenomenon which may have crucial importance for the fuel plates behavior. This phenomenon increases with burn-up [35].

For UMo/Al fuels, the irradiation experiments realized on the UMo/Al dispersion fuel reveal mainly three phenomena: the fuel-matrix interaction, fission product swelling of the fuel plate, and finally cladding corrosion. Indeed, the swelling of the cladding is relatively low. However, the swelling of the uranium-molybdenum alloys as a function of burn-up is more considerable. Then, Aluminum cladding corrosion by water results in a reaction product that is a mixture of alumina hydrates, but is often assumed to be either totally or predominantly boehmite ($Al_2O_3H_2O$). Boehmite has a low thermal conductivity (0.002 W/cm-°C). Thus, even relatively thin layers on the cladding surface, referred to as the oxide layers, can lead to significant increases in fuel temperatures.

The previous phenomena are visible through a combined behaviour: the fuel plate volume increase, commonly known as the fuel plate swelling. This latter is an unavoidable consequence of fission. Mechanical constraints on the plates' borders minimize their dimensional changes in width and length. Consequently, fuel plate swelling is essentially exhibited through a plate thickness increase, leading to a decrease of the inter-plate distance.

The fuel plate swelling is considered as a major aspect of fuel qualification. Consequently, it is of paramount importance to evaluate and estimate this parameter, bearing information on the irradiation history. This is the main objective of this thesis. To inspect this phenomenon, several post-irradiation examination methods were developed. These methods are displayed in the following section.

1.5 Plate swelling post-irradiation examination

The LEU fuel swelling can only be understood through post-irradiation examinations. In this view, many post-irradiation examination methods are employed and/or compared to improve the irradiation performance investigations.

The post-irradiation examination methods are identified according to a prominent characteristic: the non-destructive aspect. Two technique types are thus proposed and presented: non-destructive and destructive methods.

1.5.1 Destructive methods

First, the fuel plate is cut perpendicularly to the fuel meat layer in a way to visualize all the plate layer composition. Then the examination method is applied. The main useful destructive examination methods are briefly described in the following:

- The scanning electron microscopy (SEM) [36], [37],[5]: It generates electron focused beams that interact with the polished samples. The acquired signals allow the sample topography and distribution imaging within a depth of 1.0 – 1.5 μm from the surface and with a 1 μm lateral resolution.

- The electron-probe micro-analysis (EPMA) [6], [38]: The EPMA has the same principle as the SEM, with additional chemical analysis performances. It allows quantitative elemental analyzes and high resoluted images of the samples.

- The optical microscopy (OM) [7]: It employs visible light and a system of lenses to magnify surface images of cutted plate samples. These images are captured by normal light-sensitive cameras to generate a micrograph. This latter allows the micro-structural behaviour characterization such as manufacturing porosity and fuel swelling.

- The radiochemical technique [39]: Chemical separation of the samples and spectrometry measurements are employed in this method in order to evaluate the % loss of initial ^{235}U, linked to the fuel element burn-up.

1.5.2 Non-destructive methods

The main non-destructive examination methods of the fuel plates are:

- Visual inspection [9] [40]: Features are observed through a video recording and noted, on the external constituents and through the channels with element backlighted. This inspection allows visualisation of defects such as bowing, cladding blisters or cracks on the plate.

- Gamma-ray spectrometry [10], [41], [42], [43]: This system consists of a collimator tube, a lead shielding, a high-purity germanium (HPGe) detector with electronics and an acquisition module. The collimator is placed between the plate and the detector. Detected Gamma-ray spectra are accumulated according to axial and transversal positions. They provide the amount of each fission product, related to the plate absolute burn-up.

- Bench fOr Non-destructive Analyses of Plate And Rod Type fuel Elements [12], [44]: The BONAPARTE bench of the SCK-CEN belgian nuclear research centre performs analyzes of irradiated curved or flat plates. It consists of a modular plate clamping system which allows plate rotation and a modular measurement head with motorized X- and Y-movements. Positioning feedback is provided to the stepper motors by a magnetic ruler system with a repeatability of $\pm$ 100 μm (68 % confidence interval). The measuring head holds probes for plate thickness measurement under eddy current principle, and oxide thickness measurements based on a magnetic ruler.

Discussion

According to the section 1.4.2, the fuel swelling is a highly important irradiation consequence to be considered for fuel qualification. The non-destructive PIE methods may assess the plate swelling and the destructive PIE methods go deeper in the analyzes. However, these methods require to remove fuel plates from the fuel element. The fuel element structure is then obviously destructed. As a consequence, in the first part of the project, the Institute of Electronics and Systems (IES) of University of Montpellier (UM) has been developing a device allowing the **in-situ** non-destructive control of the plates inside the fuel element. It is based on the water-channel thickness measurement. This device is the ultrasound probe of the PERSEUS project for PIE of the 'RHF' with Ultra-Sounds. The description of the RHF and the first proof-of-concept validation results are presented in the following sections.

1.6 The High Flux Reactor

1.6.1 The Reactor and its plant description

The Institute Laue Langevin (ILL) is an international research organization operating the worldwide most intense neutron source, primarily dedicated to fundamental sciences. It is the High Flux Reactor (RHF), generating an unperturbed thermal neutron flux of $1.5 * 10^{15}$ n/cm^2/s. The RHF scheme is showed on figure 1.6.

The reactor is composed of three concentric regions and centralized in a cylindrical building of a 60 m diameter. This building, displayed on part (a) of figure 1.6, is constituted of 4 main parts:

- part 1: storage pool,
- part 2: light water pool,
- part 3: experimental hall,
- part 4: reactor tank.

The light water pool is of 6 m diameter and 4 m height. In this water pool, a heavy water tank, with a diameter of 2.50 m, contains the fuel element. It is consequently cooled and moderated. A more detailed scheme of the reactor components is displayed on part (b) of figure 1.6.

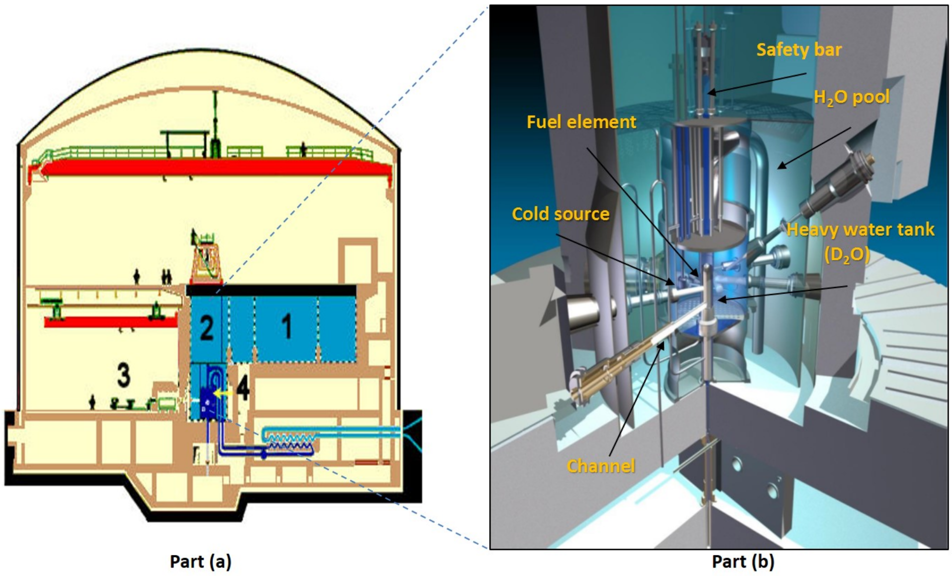

Figure 1.6: The High Flux Reactor structure [13], (a) main components of the reactor building, (b) specified components of the High Flux Reactor.

The reactor is controlled by an absorbing control rod extracted during the uranium consumption [14]. Five other bars are dedicated to the emergency shutdown of the reactor. Hot and cold neutrons are respectively slowed down by graphite and liquid deuterium volumes set up in the heavy water tank and linked to beam tubes. Neutrons are then collected by twenty channels, some of them for the cold sources and others for hot ones. The hot, cold and ultra cold neutron sources are respectively of 10^{-1} eV, 10^{-3} eV and 10^{-7} eV. Neutron guides then extend these channels to the experimental instruments located 100 meters away from the reactor fuel element.

1.6.2 The fuel element

The High Flux Reactor has one fuel element made of 280 curved plates, similar to that of the Oak Ridge National Laboratory (ORNL) High Flux Isotope Reactor (HFIR) [14]. It is manufactured by CERCA (Compagnie pour l'Etude et la Réalisation de Combustibles Atomiques, AREVA group) and showed on figure 1.7.

Each fuel plate is bent into an involute shape with an originating radius of 13.681 ± 0.005 cm [45]. The involute shape advantage is to maintain a constant distance between each plate. This distance optimizes the thermal-hydraulic cooling of the compact core. Nominally fixed at 1.8 mm, this distance has uncertainties specified locally of $\pm$ 0.3 mm and in average for the outer dimensions of $\pm$ 0.25 mm. The fuel plates are then welded to two concentric aluminum tubes, forming the fuel element. The internal and external diameters of the element are 26.08 cm and 41.36 cm.

[a] 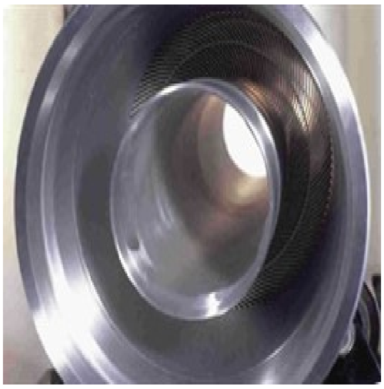 [b] 

Figure 1.7: (a) General structure of the RHF fuel element [13], (b) zoom over fuel plates.

The fuel plate has a total height of 90.3 ± 0.02 cm including a fuel part height of 81.3 ± 0.02 cm. This fuel part is centrally located between two borated zones, at the upper and lower extremities. The borated zones act as a reactivity reserve for the end of cycles and moderate the peak of flux on the edges of the plate. The total fuel plate thickness is 1.27 ± 0.035 mm. It is composed of a 0.51 ± 0.08 mm thick dispersed UAlx fuel, situated between two zones of 0.38 ± 0.08 mm thick AlFeNi cladding. The fuel plate dimensions are presented on the figure 1.8.

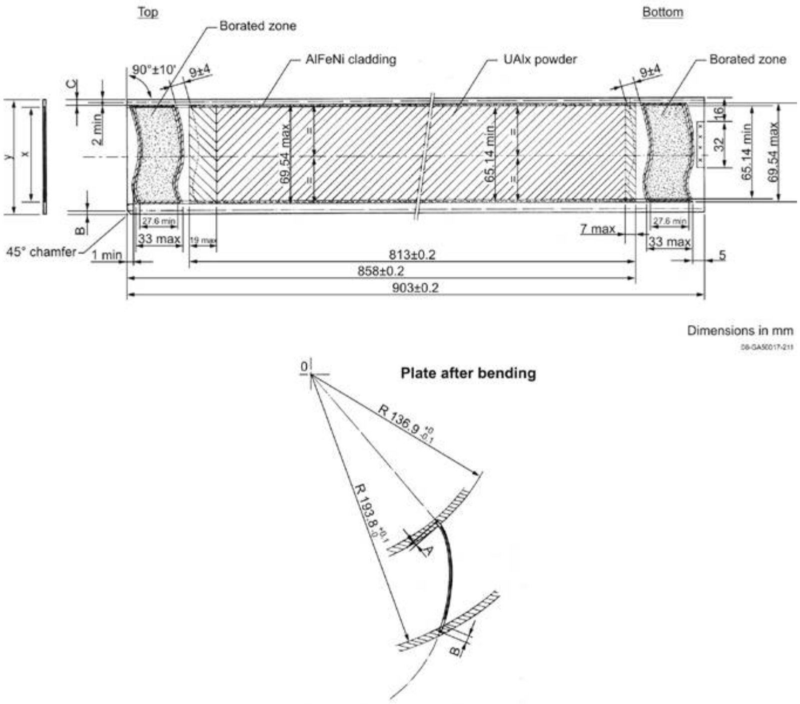

Figure 1.8: The fuel plate dimensions [45].

1.6.3 RHF conversion into LEU high density fuel

The current RHF HEU fuel is a UAlx powder dispersed in an Al matrix. It is enriched at 93 % in ^{235}U leading to 30.6 g of ^{235}U per plate. It was designed for continuous operation of 45 day cycles with a thermal power of 58.3 MW. The new LEU UMo fuel proposed is based on a dispersed technology, a UMo powder mixed in an Al matrix.

For the RHF, performances are defined by the cycle length and the neutron flux magnitude in the beam tubes [45] [14]. Direct replacement by U−7Mo fuel would lead to a loss of performance, the cycle length would be shortened and the magnitude of the flux would be too decreased for being acceptable.

To address this issue, in the framework of a conversion study into LEU, the ILL and the ANL have collaborated to investigate LEU designs for the RHF [46]. A promising candidate has been selected and studied. It would allow the increase of the total amount of fuel without changing the external plate dimensions by relocating the burnable poison. This proposed LEU design has been called TOUTATIS. Both preliminary hydraulic safety margins and performance losses for the neutron flux have been evaluated with favorable results. In fact, there are still several conditions to fulfill for the RHF conversion ability, such as the experimental validation of the UMo in normal and transient operating conditions for which PIE would be necessary.

In this view, the ILL and the IES are collaborating in the PERSEUS Project to develop a non-destructive high frequency ultrasonic device. It allowed inter-plate distance measurements and was first tested on an ILL fuel element [47]. The measurement set-up and the first thesis feedback are following.

1.6.4 PERSEUS Project

Ultrasonic device constraints

For inter-plate distance measurements, several constraints need to be considered. First, the fuel element is placed under, at least, 5 m of moderating water. Moreover, the plates are manufactured in involute shapes in order to maintain constant inter-plate distances of 1.8 mm. Both of these constraints induce waterproof and height parameter aspects of the measuring device.

Besides, the fuel element must not be dismantled to observe accurate inter-plate distances. These latter measurements necessitate a micrometric resolution due to the microscopic plate structural modifications expected at 25 μm. These constraints imply a non-destructive aspect, limiting the device thickness at 1 mm, and a measuring objective of a 1 μm resolution.

Finally, the radiative environment must be taken into account for the whole measurement system components. In this view, its influence over the distance measurement, obviously on the ultrasonic device components, should be determined.

Ultrasonic device principle

In the early stages of the project, the developed device was mainly constituted of two ultrasonic transducers with frequencies around 100 MHz to achieve the expected resolution. These latter were introduced in two cavities realized on a steel blade. This latter was intended to be inserted between two fuel plates. Consequently, the blade was designed with a thickness/width/length of 1/10/1500 mm. As the fuel element is placed in cooling water, ultrasonic waves transmitted by each transducer propagates through water and then reflect on the water/plate interface. Reflected signals are then received by the same transducer and acquired by a set of electronic instruments. The measurement principle is presented in figure 1.9.

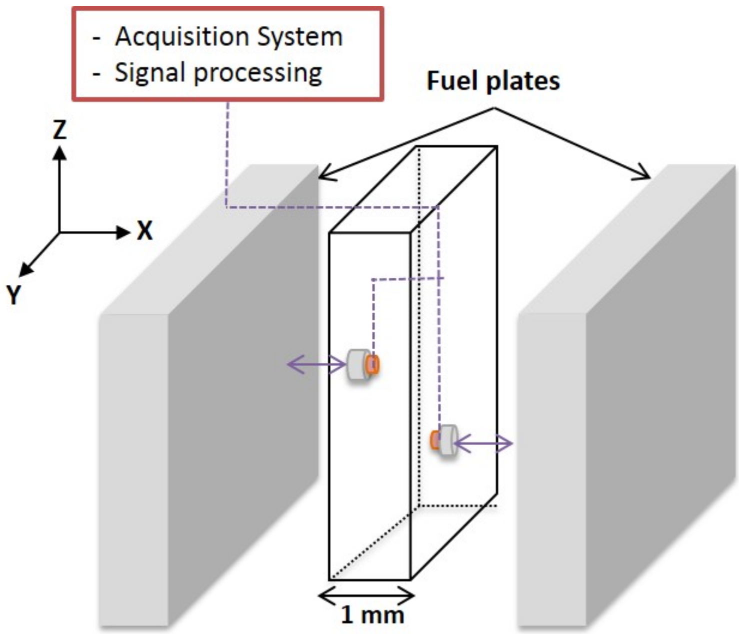

Figure 1.9: General principle of inter-plate distance measurement.

Consequently, the inter-plate distance measurement d depends on the following parameters: the time of flight (ToF) [48] of the ultrasonic wave propagating in the coupling medium (t_1 and t_2), the ultrasound velocity V and the distance separating the two ultrasonic transducers h, via the following equation (1.6.4):

$$d = h + V * (\frac{t_1 + t_2}{2}). \tag{1.1}$$

Experimental results

The ultrasonic device was first tested in RHF spent fuel element in December 2013 and July 2015. Both experiments were successfully handled proving the measurement feasibility of both the time of flight and the ultrasonic velocity parameters in a high radiative environment. Indeed, for each transducer, the acquired signal has the shape of figure 1.10.

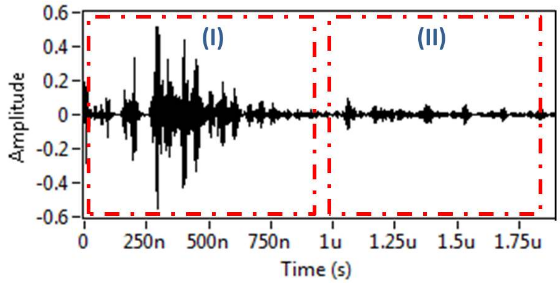

Figure 1.10: Experimental ultrasonic signal displaying two echo series, (I) reflected echo series on the silica support, (II) reflected echo series on the plate.

In figure 1.10, the acquired signal is composed of two identified echo series: the first series (I) corresponds to the transducer ultrasonic signature and allows resonance frequency monitoring. This frequency is related to the water temperature, enabling ultrasound velocity estimation. More details are presented in the chapter 3 and in the articles [49] and [50]. Then, the second series (II) corresponds to the reflection of the first series' complement on the fuel plates. Time of flight evaluation is realized thanks to a cross-correlation of these two series, allowing inter-plate distance estimations through the equation (1.6.4).

An example of an inter-plate distance measurement realized inside a water channel, during the July 2015 experiment, is shown in figure 1.11. Blue points represent raw data and the red line corresponds to an average value measured every 10 acquisitions.

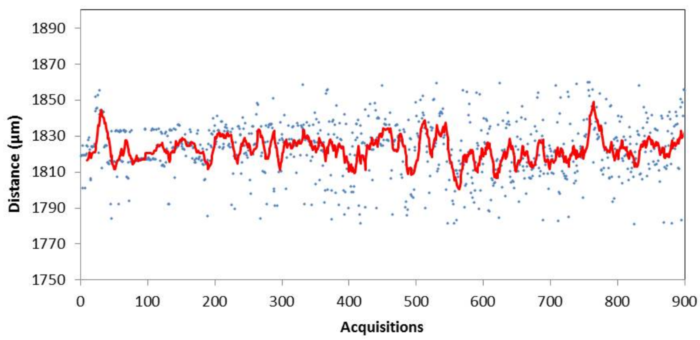

Figure 1.11: Inter-plate distance measurements.

Here, the blade was positioned in the water channel with no control over the blade displacement velocity. On the average line the water channel thickness varies from 1.81 ± 0.01 mm to 1.84 ± 0.01 mm with a local standard deviation of 15 μm. The first thesis then allows the proof-of-concept on the feasibility measurement of the inter-plate distance using a high frequency ultrasonic method. More information are available in the first thesis manuscript [51].

First thesis feedback and second thesis objectives

In a way to briefly summarize the feedback of the first thesis, it is clearly important to mention the challenge of the conception of a device combining mechanical, electronic and ultrasonic performances to be introduced in a hostile environment respecting fuel element constraints. The ultrasonic transducer structure was modeled allowing the understanding of its behaviour and its optimization.

The device components demonstrated radiation resistance during the experiments. The signal to noise ratio quality was clearly sufficient to obtain a stable estimation of inter-plate distance and water temperature. Despite the difficult conditions of the experiment, appropriate relative variation measurements of the inter-plate distance were obtained as the one presented on the previous figure 1.11. These relative measurements were consequently estimated with a global precision of 20 μm.

On the other hand, the experiments allowed the identification of several flaws. It was first observed that the time of flight measurements were influenced by the ultrasonic device handling. Indeed, it can be observed in figure 1.9 that ultrasonic transducers are inserted in different cavities of the blade. This fact implies a difficult simultaneous alignment of both ultrasonic transducers to the facing plates. Consequently, either a variation or a lack of the signals is observed and impacts time of flight estimations. Secondly, the ultrasonic velocity identification depends on the water temperature estimation based on an analysis of the transducer frequency variation measured through the acquired signals. These signals include electrical reflections and noise that complicate the transducer frequency identification. Thirdly, the inter-transducer distance influences the distance measurement accuracy. Finally, the ultrasonic device vertical position inside the fuel element is not determined. Consequently, the plate zone where the distance is measured is not identified.

All these issues are clearly affecting the inter-plate distance measurements' accuracy. A second thesis has consequently been set-up in a way to improve the first ultrasonic device reliability and measurement reproducibility. In this view, a deep reflection over the ultrasonic device conception and realization has been undertaken according to the previous experimental results. Each part of the measurement chain has been analyzed and optimized to respect the measurement constraints and has consequently led to a second ultrasonic device prototype. A monitoring of the ultrasonic device vertical position has been introduced. The signal acquisition and processing have been optimized, consequently improving the measurement resolution. A study of the ultrasonic device resistivity under the high radiations has also been carried out in a way to precisely quantify the impact over the ultrasonic measurements. Finally, inter-plate distance measurement experiments were realized on the High Flux Reactor fuel element by the second prototype ultrasonic device. These different points will be presented in the following chapters.

1.7 Conclusion

The conversion from HEU to LEU of HPRR requires a LEU high density fuel development and qualification. For this, the HERACLES program has several steps. In particular, it includes PIE methods to monitor irradiation fuel behaviour phenomena. Among these latters, the fuel swelling is considered as a highly significant parameter to be examined. For this purpose, several methods, either destructing the fuel plate or not, have been employed.

For plate swelling characterization, a new method has been proposed in the early stages of the project, focusing on the inter-fuel-plate distance evaluation. This method has the great advantage of being non-destructive. It is the PERSEUS project being a collaboration between the Electronics and Systems Institute of Montpellier University and the Institute Laue Langevin. As a part of the HERACLES consortium, the ILL allowed the test of the PERSEUS device in the High Flux Reactor fuel element for a first thesis project.

During the first thesis, the high frequency ultrasonic device was modeled, developed according to the experimental constraints and tested over the High Flux Reactor fuel element. These experiments allowed the validation of the inter-plate distance proof-of-concept feasibility. They also allowed the identification of several flaws to be optimized in order to increase the distance measurement reliability and resolution, consequently leading to a new ultrasonic device prototype. This new ultrasonic device is the actual objective of this thesis project. The new structure of the ultrasonic device including all the optimizing elements will be presented in the following chapter.

Chapter 2

Ultrasonic device

Contents

2.1 Introduction **44**
2.2 Ultrasonic device constraints **44**
2.3 New ultrasonic device realization **45**
2.3.1 Ultrasonic device principle 45
2.3.2 Ultrasonic transducer 47
2.3.3 Mechanical support 53
2.3.4 Ultrasonic device assembly 54
2.3.5 Electronic system 54
2.4 Ultrasonic device positioning **57**
2.4.1 Laboratory measurement bench 58
2.4.2 Linear cable sensor 59
2.5 Conclusion **60**

2.1 Introduction

The High Flux Reactor (RHF) of the Institute Laue-Langevin (ILL) [13] is made of a unique fuel element presented on figure 1.7 of the first chapter. This element is constituted of 280 curved aluminum plates. Initially, two adjacent plates are separated by a nominal distance of 1.8 ± 0.3 mm and each plate includes high enriched Uranium.

After a radiation cycle, the fuel element is placed in a moderating water pool so that its nuclear activity can cool down safely. According to the previous chapter, one of the main irradiation behaviour phenomena is the plate swelling. Consequently, its examination is necessary. For this, as previously mentioned, an ultrasonic device was developed to allow inter-plate channel thickness measurement. Considering the previous thesis experimental feedback, a new prototype high frequency ultrasonic device has been developed allowing a significant performance improvement.

In this chapter, an overview of the inter-plate distance experimental constraints is first reminded. Then, the manufacturing process of the new non-destructive high frequency ultrasonic device prototype is detailed with an emphasis on each initial flaw of the measurement chain components. Several parameters are discussed in a way to achieve distance measurement with a micrometric resolution. After that, a new measurement bench is developed in the laboratory according to the determined axes influencing the measurement and allowing element inter-faces distance characterization.

2.2 Ultrasonic device constraints

The ultrasonic device experimental constraints are briefly reminded. First, the measurements take place in the RHF radiative environment. Second, the fuel element is situated 5 meters below the surface of the water pool. Third, the fuel element structure is made of involute curved plates that have constant inter-plate pre-irradiation distances of 1.8 ± 0.3 mm. The device thickness was limited to 1 mm. Finally, a micrometric resolution is the end-goal due to the microscopic structure modifications of curved plates.

Moreover, the previous experiment feedback comes up with several flaws [52] [53]. Indeed, the insertion of the transducers in separate cavities induces misalignment. This misalignment is amplified by the device handling. Consequently, this induces difficulties in the optimization of both transducers' signals and influences time of flight estimation reliability. Besides, electrical reflections in the cables interfere with both the time of flight and the ultrasonic velocity estimations. Furthermore, the influence of the irradiated environment on distance parameters is not identified. Finally, the vertical device position identification remains necessary to link the distance measurement to the analyzed plate zone.

2.3 New ultrasonic device realization

The ultrasonic device is composed of three main parts : the active ultrasonic part, the electronic part, and the mechanical part. In the following is presented the conception of each part of the new ultrasonic device prototype realization.

2.3.1 Ultrasonic device principle

For the new ultrasonic device, the distance measurement is bazed on the principle presented in figure 2.1. In comparison with the first ultrasonic device principle of figure 1.9, the new ultrasonic device in figure 2.1 displays the device position monitoring, and the transducers' structure modification as two principle innovations.

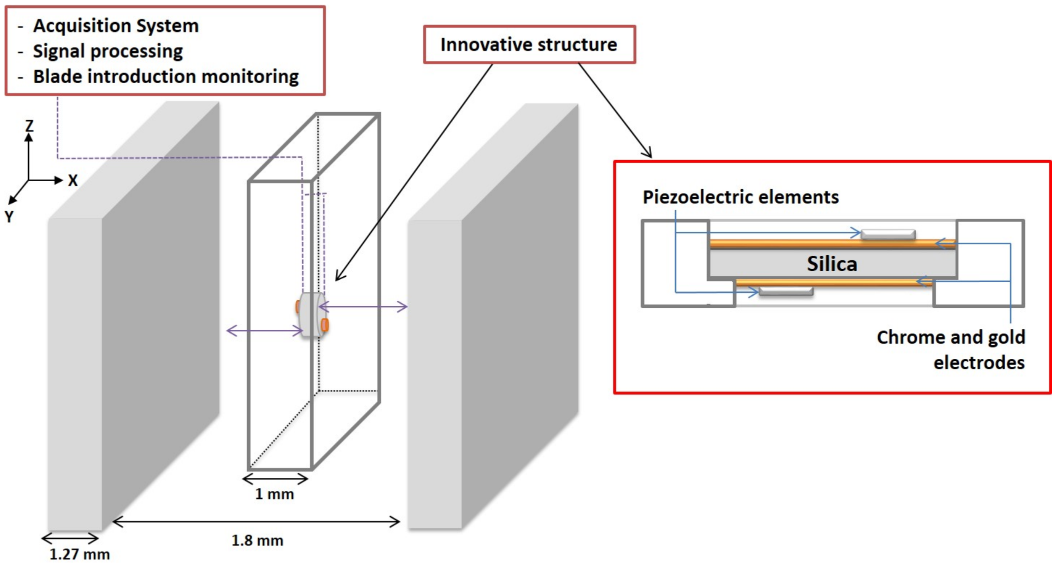

Figure 2.1: General principle of inter-plate distance measurement.

The inter-plate distance measurement depends on: time of flight [54] in water, the ultrasound velocity in water, and inter-transducer distance. Except for the ultrasound velocity, the other parameters are directly optimized thanks to the innovative transducer structure and their advances are described in the following.

Innovative structure and its advances

In the first ultrasonic device prototype, transducers were independent, fixed to silica supports and integrated into two different cavities of the mechanical support as presented in figure 2.2 (a). This separated integration induced an uncertainty on the inter-transducer distance denominated h in the distance equation (2.1) refering to figure 2.2:

$$d = h + d_1 + d_2. \tag{2.1}$$

It also influences the transducer alignments yielding potential errors on the estimation of the transducer to plate distances d_1 and d_2.

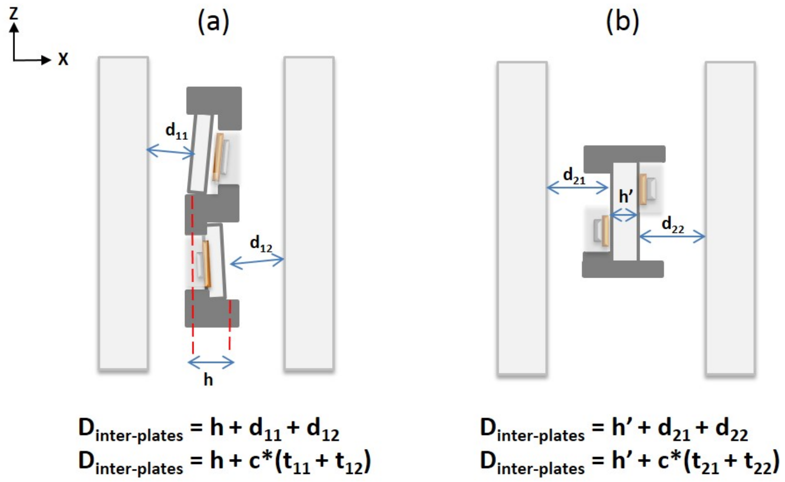

Figure 2.2: Innovative structure improvement illustration.

In the new structure of figure 2.2.(b), the silica support diameter has been fixed to 6 mm and the transducers miniaturized to a diameter of 2 mm so that they can be positioned vertically as close as possible. The main advantages of this new device structure are:

- The inter-transducer distance, nominated h' in figure 2.2 (b), is precisely known and equal to the silica thickness of $h' = 400$ μm,
- The unique support optimizes the inter-transducer-parallelism,
- A simultaneous alignment of both transducers' ultrasonic beams to the fuel plates is optimized,
- A smaller zone of the plates is analyzed since the transducers' separating distance is reduced from 8 mm to 2 mm,
- A deeper hole is realized for the new structure insertion, allowing a 300 μm increase of the water distance, to limit echo overlapping and simplify signal processing,
- Temperature measurements are performed for both sensors on the same silica support.

Both transducers possess the same structure and behavior presented in the following.

2.3.2 Ultrasonic transducer

The two transducers of figure 2.2 are mainly composed of a piezoelectric element linked to a unique silica support such as:

- The piezoelectric elements chosen in this project are of $LiNbO_3$, due to its high stability in hostile environments [55].
- The silica support element is made of high pure SiO_2. As previously mentioned, its thickness is of 400 μm and its diameter of 6 mm.

Ultrasonic transducer manufacturing

The transducer manufacturing process starts with the metallization of both piezoelectric elements and of the silica support. It consists in chrome and gold deposits, ensuring the electrical conductivity. The piezoelectric element and the silica support are then bonded.

The following step consists in the thinning of the piezoelectric element downto a specified thickness. This thinning is realized through polishing. The resulting piezoelectric element thickness, referred to as e_{piezo}, is of a paramount importance as it is the parameter directly related to the transducer resonant frequency, referred to as f_{piezo}. This parameter is developed in the following section. The final step consists in the second face metalization. It is realized thanks to an aluminum thickness deposit.

Ultrasonic transducer resonant frequency

The following equation 2.2 links e_{piezo} and f_{piezo} through the piezoelectric element longitudinal velocity, referred to as c_{piezo}:

$$f_{piezo} = \frac{c_{piezo}}{2 * e_{piezo}}. \tag{2.2}$$

To achieve a specified resonance frequency, the piezoelectric element then should be thinned down to the corresponding thickness.

As a matter of fact, the resonance frequency is one of the most relevant parameters influencing the measurement accuracy. Indeed, it is related to the ultrasonic wavelength in the propagation medium. This latter, known as λ_{water} constitutes the double of the acoustic resolution. The wavelength relates, through the equation 2.3, the frequency and the longitudinal velocity in the environment the wave is going through.

$$\lambda_{water} = \frac{c_{water}}{f_{piezo}}. \tag{2.3}$$

For instance, for a frequency range from 75 MHz to 150 MHz, the distance measurement resolution goes from 10 μm to 5 μm. As a consequence, to achieve the highest resolution, the first choice would be to increase as much as possible the resonant frequency. However, the higher is the frequency the more important are the attenuation phenomena manifested in the water and in the electric cables. These phenomena are investigated in the following parts.

Transducer structure impact on the resonance frequency

The transducer resonant frequency defines the generated acoustic echo form. This echo then propagates in the transducer multilayered structure. This latter comprises: the piezoelectric element, the chrome and gold electrode layers, the adhesive layer and finally the silica support. The multilayered structure is displayed in the scheme of figure 2.3.

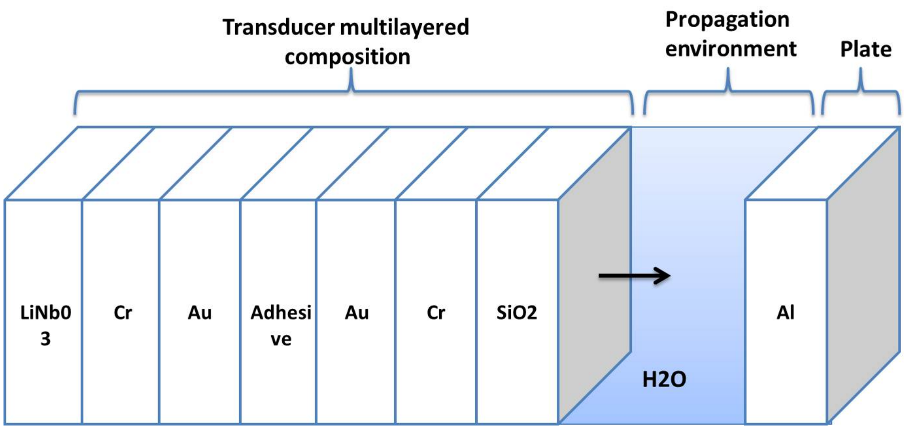

Figure 2.3: Multilayered composition of the transducer.

At the high working frequencies of the device, the structure of the multilayered sensor is of the order of the ultrasonic wavelength and plays a crucial role in the shape of transmitted and received signals. Their complex nature and the expected resolution then imply a close understanding of the structure of the sensor ultrasonic signature. The modeling of the acoustic behavior of the transducers has been made thanks to the transfer matrix method [50], [56], [57], [58] and results are presented in the following section.

Utrasonic signal modeling

When an ultrasonic wave is generated by the ultrasonic element, it propagates through the layers to the Silica/Water interface where some of its energy is reflected.

Multiple reflections then occur in the silica support leading to an echo series, denoted SW for Silica/Water. It is presented in figure 2.4 (a). The complement of this series is transmitted into the water and reflects on the plate, generating a second series, denoted in the following as WP for Water/Plate. It is presented in figure 2.4 (b).

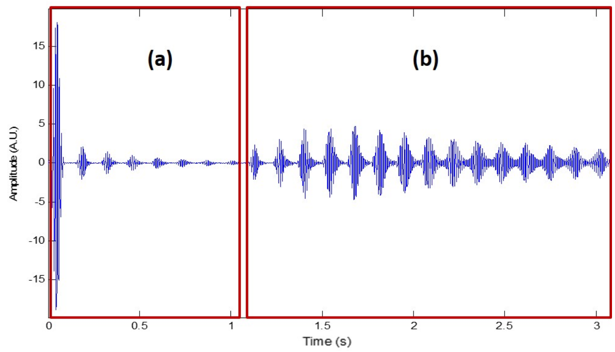

Figure 2.4: Modeled ultrasonic signal of a 90 MHz central frequency transducer displaying two echo series, (a) reflected echo series on the silica/water interface, (b) reflected echo series on the water/plate interface.

The following example allows the visualization of the adhesive material impact. The ultrasonic signal is modeled assuming a resonant frequency of $f = 90$ MHz and the corresponding thickness of the piezoelectric element is:

$$e_{piezo} = \frac{c}{2 * f} = \frac{7331}{2 * 90 * 10^6} = 40.5\ \mu m. \tag{2.4}$$

In the transducer manufacturing process, the adhesive layer thickness is of the order of 10 μm. Moreover, the acoustic wavelength in the glue is equal to:

$$\lambda_{adh} = \frac{c}{f} = \frac{2400}{90 * 10^6} = 26\ \mu m. \tag{2.5}$$

This indicates that the adhesive layer thickness is of the order of $\lambda_{adh}/2$, possibly yielding resonance phenomena. To understand the influence of the adhesive thickness on the ultrasonic signal, a first modeling is performed with a glue thickness fixed to 13 μm. The resulting ultrasonic series are presented in figure 2.5 (a) and a zoom of the WP series is displayed in figure 2.5 (b) where the adhesive layer resonance is clearly visible through an echoes' overlapping.

A second modeling of the transducer response is now proposed with an adhesive layer thickness of 10 μm. The resulting signal is displayed in figures 2.6 (a) and (b). The echoes are now clearly separated, facilitating the future time of flight evaluation. Consequently, in the manufacturing process, attention must be paid to the relation between the frequency and the adhesive layer thickness. The adhesive layer thickness

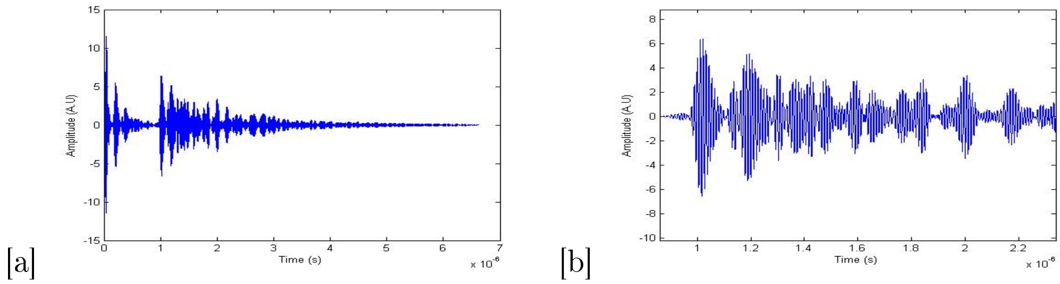

Figure 2.5: (a) Modeled received ultrasonic signal with an adhesive layer thickness of 13 μm; (b) Reflected series on the WP interface.

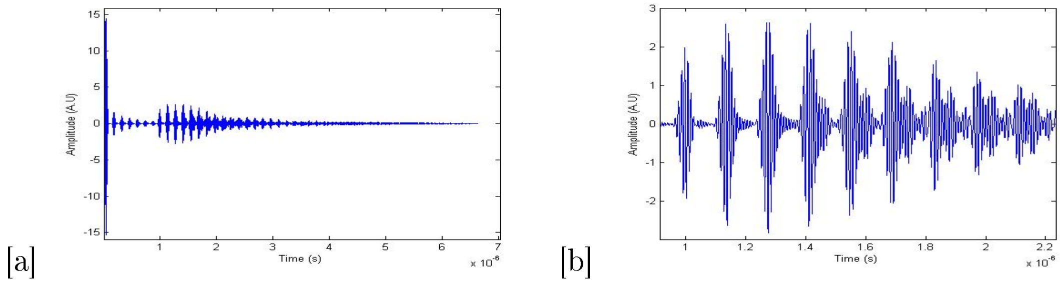

Figure 2.6: Modeled received ultrasonic signal with an adhesive layer thickness of 10 μm; (b) Reflected series on the WP interface.

is then initially measured to determine the convenient frequency range. If the allowed frequency range is not compliant with the expected resolution, the piezoelectric element is removed to modify the adhesive layer thickness. This operation is also applied during the second transducer manufacturing if its bandwidth frequency does not match the first transducer one.

Signal attenuation

The electrical cable attenuation influences the signal acquisition. In this view, an adequate electric cable has been chosen. Indeed, its specification assumes that for the frequency range from 70 MHz to 150 MHz, the attenuation goes from 0.14 dB/m to 0.30 dB/m. The cable length is the second relevant parameter influencing the attenuation and will be investigated in section 2.3.5. However, considering the electrical cable length in a range of 8 m to 20 m to position the electrical devices away from the radiative environment, the consequent attenuation level goes from 1 dB for a 70 MHz resonant frequency, to 6 dB for a 150 MHz resonant frequency.

The ultrasonic signal will also be influenced by attenuation in water which is given as a function of the frequency through the following equation 2.6 [59]:

$$\alpha = 2.17 * 10^{-16} * f^2 \quad dB/mm. \tag{2.6}$$

This corresponds, in the [70-150] MHz frequency bandwidth, to an attenuation ranging from 1 dB/mm to 4.8 dB/mm. As a consequence, the maximum attenuation underwent by the ultrasonic signal is of the order of 20 dB, propagation in the cables and water corresponding to 12 dB and 8 dB, respectively.

Ultrasonic field

This section presents the ultrasonic field generated by the transducer in the silica delay line and water. The objective is, in particular, to quantify the effect of the electrodes' dimensions on the device radiation. To do so, each point of the piezoelectric element surface is considered as an ultrasonic spherical source. The multiple waves consequently generated interact to form the ultrasonic field [60]. This is known as the Huygens-Fresnel principle. The ultrasonic pressure P at a point from the space with the coordinate r, provided from a surface S, is calculated from the pulsation ω, the propagation environment density ρ_0, the velocity normal to the surface V_n, the wave vector K and the distance R separating the point r and the radiation surface points, under the following equation 2.7:

$$P(r,t) = \frac{j\omega\rho_0}{2\pi}\int_S \frac{V_n(r)e^{-jKR}}{R}dS. \tag{2.7}$$

In the case of a plane surface radiating in water, the ultrasonic fields possess the form presented in Figure 2.7. The characteristics of the radiated surface are here : 1 mm diameter and a 90 MHz central frequency. Figure 2.7 shows that the ultrasonic field

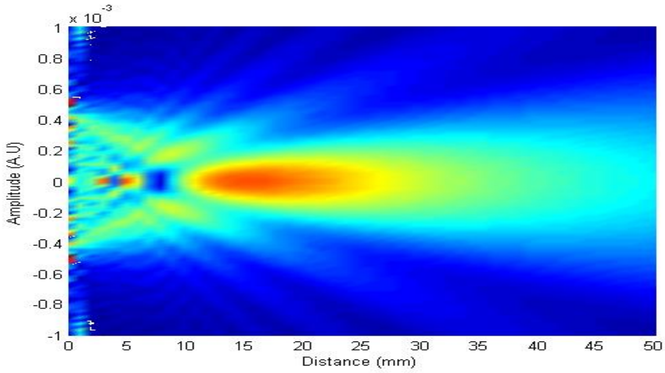

Figure 2.7: Ultrasonic field generated in water by a 1 mm diameter plane surface at 90 MHz.

consists of two parts. The first one, for which the field intensity is mostly affected by constructive and destructive wave interferences, is known as the near field or Fresnel zone. The ultrasonic field is more uniform far from the transducer in the second part known as the far field or Fraunhofer zone [61]. The transition between the near field and the far field occurs at a distance Z_m related to the piezoelectric element disc radius, a, and the ultrasonic wavelength, λ, through the following equation 2.8:

$$Z_m = \frac{a^2}{\lambda}. \tag{2.8}$$

Figure 2.8 now presents the transducer ultrasonic field modeled considering the following parameters: the piezoelectric element diameter is of 1 mm, the resonant frequency is of 90 MHz, and the silica thickness is of 400 μm. The two media contributing to the propagation of ultrasonic waves are then taken into account. Figure 2.8 (a) shows that, in the silica support, the ultrasonic field corresponds to

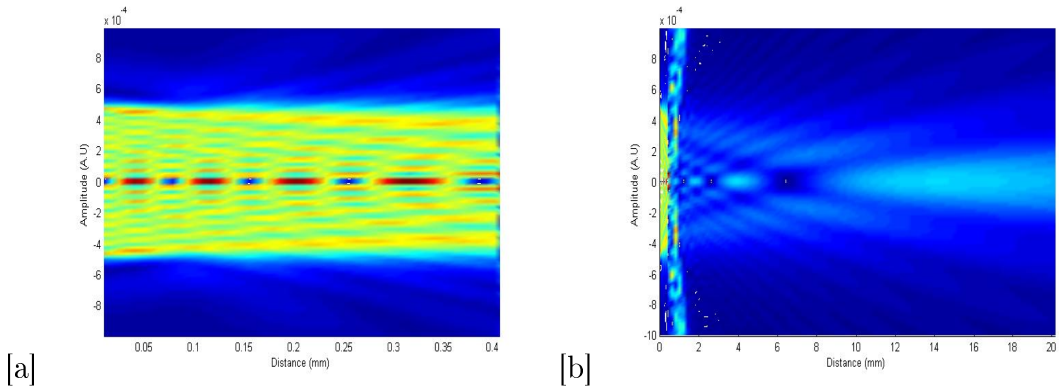

Figure 2.8: Ultrasonic field generated in silica and water by a 1 mm diameter plane surface at 90 MHz. (a) displayed in the silica of 0.4 mm, (b) displayed until 20 mm.

the near field. Moreover, the Huygens model indicates a far field beginning at the distance of $Z_m = 15$ mm in water, consistent with the ultrasonic field presented in figure 2.8 (b). Assuming that the inter-plate distance to identify is of the order of 2 mm, the measurement will have to be made in the near field. Note however that the above computation is performed at a single frequency and that the ultrasonic field in a frequency bandwidth would integrate the radiation of the source for each frequency, smoothing the near-field energy distribution.

The experimental constraints fixing the device geometry, most of the measurements presented in this manuscript have been done in this configuration. However, the distance Z_m can be optimized by either increasing the wavelength λ or reducing the piezoelectric element disc radius a. Both solutions possess drawbacks. The first one will reduce the resolution and the second one decreases the energy surface reception.

On the other hand, reducing the disc radius a modifies the opening angle θ of the acoustic field defined by the equation 2.9:

$$\sin\theta = 0.6 * \frac{\lambda}{a}. \tag{2.9}$$

While increasing the acoustic spot dimensions on the plate, this could help the device alignment with the plates, as discussed in the last chapter. As an example, the figure 2.9 presents the ultrasonic field corresponding to a transducer with a disc diameter reduced from 1 mm to 500 μm.

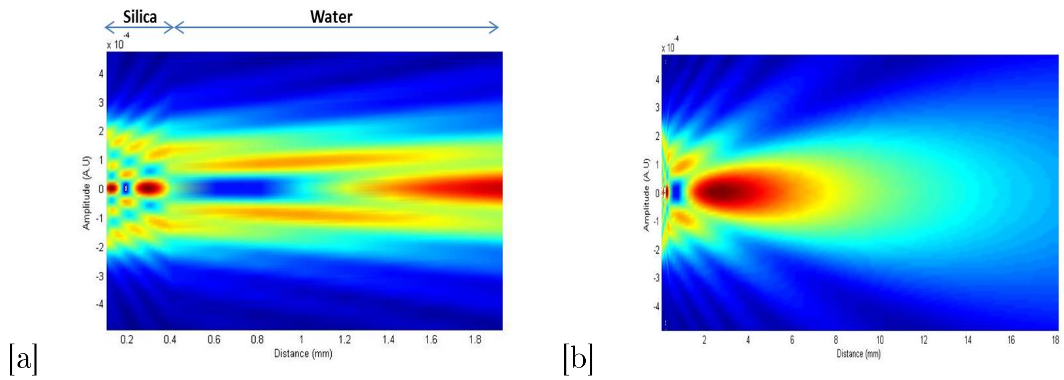

Figure 2.9: Ultrasonic field generated in silica and water by a 0.5 mm diameter plane surface at 90 MHz. (a) displayed until 2 mm, (b) displayed until 20 mm.

Note that the far field distance is reduced to $Z_m = 3.75$ mm, possibly increasing the ultrasonic energy on the plate surfaces. This has to be tempered by the fact that a pressure local minimum exists at $Z_m/2$ close to the expected device/plate distance. This discussion will be reconsidered in the last chapter when analyzing in-situ measurements.

2.3.3 Mechanical support

The mechanical support, named here as the blade, is designed to respect the experimental constraints. First, a tube support of 4 m is provided to handle the device and to allow the access to the fuel element. Second, to be introduced into the inter-curved-plate nominal 1.8 mm water-channel, the device is manufactured of stainless steel with the dimensions 1 mm thick, 10 mm wide and 750 mm long. This latter was chosen to estimate the inter-plate distances of the first height half of the plate. Third, one hole is realized on the blade to comprise the new ultrasonic structure. Finally, a groove is made on each face of the blade to integrate cable. A scheme of the mechanical support is presented in figure 2.10.

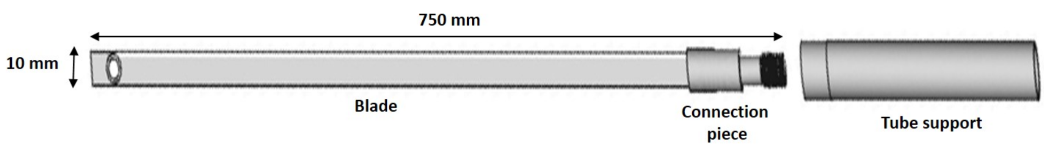

Figure 2.10: Blade to support connection and stainless tube support.

2.3.4 Ultrasonic device assembly

The ultrasonic structure is introduced in its blade emplacement. Then, a semi-rigid coax cable of 750 mm long is placed in the groove. This cable is characterized by a 0.6 mm diameter, allowing its insertion in the 1 mm blade thickness. Then, the ultrasonic transducer of each face is linked to this cable via a conducting material. Finally, an insulator material, forming the backing element, is deposited. It allows the attenuation of ultrasonic waves generated in the inverse direction of the silica support. In fact, if reflected, these waves could be superposed with the ones transmitted through the silica support. It is also a protection of the electric contact.

Figure 2.11: Assembled ultrasonic device.

The coax cable is related to a second cable connected to the electronic system described in 2.3.5. This second cable is not constrained by the fuel element dimensions. However, its length needs to be at least of the distance between the fuel element and the electronic system. In fact, the cable length influences the acquired signals. The electronic system components and their impact on the signals are further discussed.

2.3.5 Electronic system

The acquisition chain starts by a dual transmitter/receiver board designed and produced by IES generating the excitation signal. It is transmitted through a coaxial cable connected to the transducer. The reflection is acquired and converted into a digital form by the NI PXIe−5162 acquisition card. It was chosen for its 2∗2.5 GS/s sampling frequency and 10 bits resolution. Then, digital signal processing is applied.

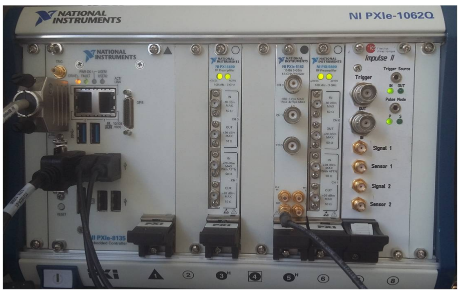

Figure 2.12: The chassis including electronic instruments.

The acquisition chain implies that the signal includes electric and acoustic echoes. Indeed, reflections on cable/piezoelectric element interface form electric echoes and reflections on silica/air interface form acoustic ones. While only acoustic echoes are required for ToF evaluation, implicitly for cross-correlation with water/plate series, both types' distinction is necessary. System components' impacts are then analyzed.

Signal generated in the cable

The excitation signal is transmitted through a 8 m cable. One cable side is related to the excitation signal transmitter while the other one is free. This later fact was intentional to acquire reflected echoes from impedance difference between the cable and the air. The cable response with and without digital filtering is presented in figure 2.13.

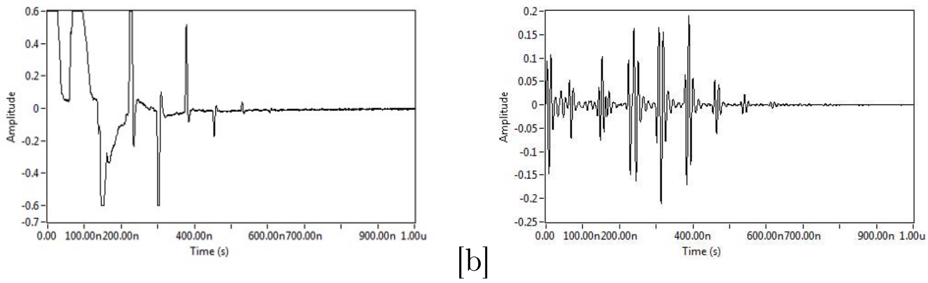

[a] [b]

Figure 2.13: Signal received through a cable of 8 m: (a) before (b) after filtering.

The time interval between each echoes' pair is of 80 ns. It corresponds to the time of flight of the electromagnetic wave in the 8 m cable. To distinguish electric from acoustic echoes, a simulation of time arrival values follows.

Simulation of the electric and acoustic echoes considering a cable of 8 m:

In figure 2.14, the black signal presents electric reflections through a 8 m cable while the red signal is the acoustic signal generated only from the first electric echo.

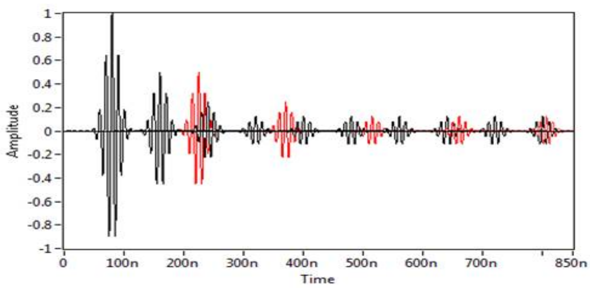

Figure 2.14: Electric (black) and acoustic (red) echoes considering a cable of 8 m.

In figure 2.14, while acoustic echoes are separated by $\Delta t = 145$ ns, electric ones are separated by $\Delta t = 80$ ns. The comparison of electric and acoustic echoes displays an overlapping of the first acoustic echo, at 225 ns, and of the third electric echo, before other following echoes' overlappings.

To avoid echoes' overlapping, two solutions can be proposed, implying either ultrasonic or electric ToF control. The first one deals with silica support thickness modification, while the second one modifies the cable length. Due to experimental constraint of the blade introduction in the fuel element, the second solution is favored. Simulations with different lengths were tested leading to a convenient value of 20 m. It was applied for the device realization and results are following.

Experimental signal analysis

The figure 2.15 (a) displays electric echoes using only the cable. This signal is transmitted through the transducer leading to acoustic echoes of figure 2.15 (b).

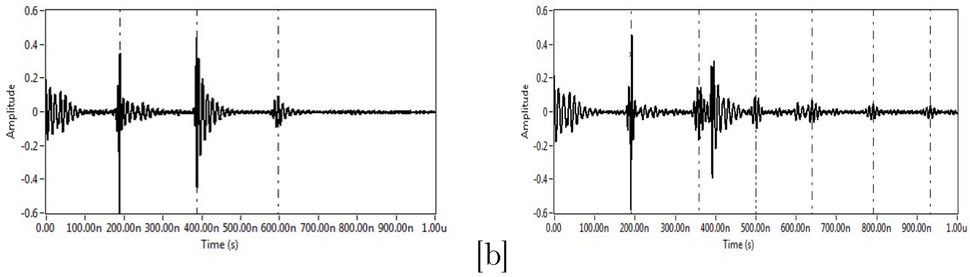

[a] [b]

Figure 2.15: (a) Reflected signal on the cable (b) reflected signal through the transducer.

Electric echoes are separated of $\Delta t = 200$ ns corresponding to ToF in the cable and acoustic echoes are separated by $\Delta t = 145$ ns, the ToF in silica support. These latters form the first acoustic echo series, necessary for ToF evaluation.
To verify the echo type identification, a comparison of the signal of figure 2.15 (b) with and without digital filtering is realized in figure 2.16.

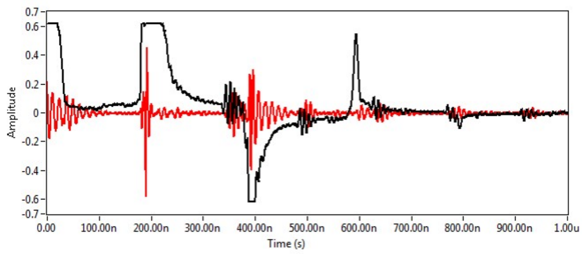

Figure 2.16: Two signals: (red) signal received after the transducer excitation and filtered; (black) signal received after the transducer excitation without filtering.

This comparison confirms the previous identification of electric and acoustic echoes. To sum up, in this section the new ultrasonic device structure advantages were presented. Then, the mechanical modifications were displayed. Finally, the electric system analyzes and modifications induced a better understanding of the signal. The next section deals with the ultrasonic device positioning stabilization.

2.4 Ultrasonic device positioning

In order to ensure an adequate and stabilized positioning of the ultrasonic device, its automatic control is required. This latter is subjected to three main objectives:

- Analyzing the impact of identified freedom axis over the ultrasonic field alignment and consequently the distance measurement: the main required movements in this case are referred to in figure 2.17 as R(x), R(y) and R(z).
- Realizing inter-faces distance measurements of calibrated samples according to the axes Y and Z: the main required movements in this case are the translation according to the axes Y and Z, referred to in figure 2.17 as T(y) and T(z).
- Distance estimation according to transducers' horizontal positions: translation movement according to X axis and presented in figure 2.17 as T(x) is necessary.

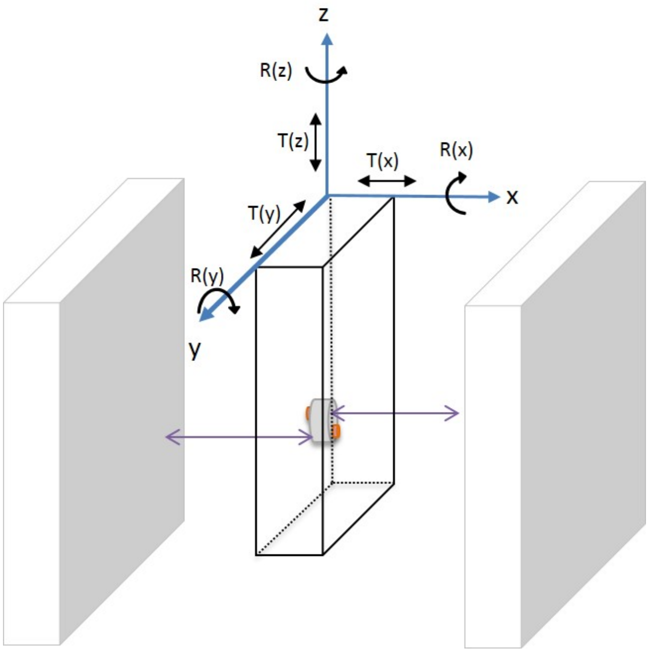

Figure 2.17: Scheme of the blade positioning between two plates.

In the laboratory experiences, the movements corresponding to a motorized control are: T(x), T(y), T(z) and R(z), consequently allowing adequate inter-faces distance estimation, ultrasonic field characterization and reproducibility measurements. For the other movements, a manual micrometric real-time control will allow a convenient alignment between the transducer and the sample faces.

2.4.1 Laboratory measurement bench

According to the previous movements' analysis, a mechanical bench has been designed and its scheme is presented in the figure 2.18.

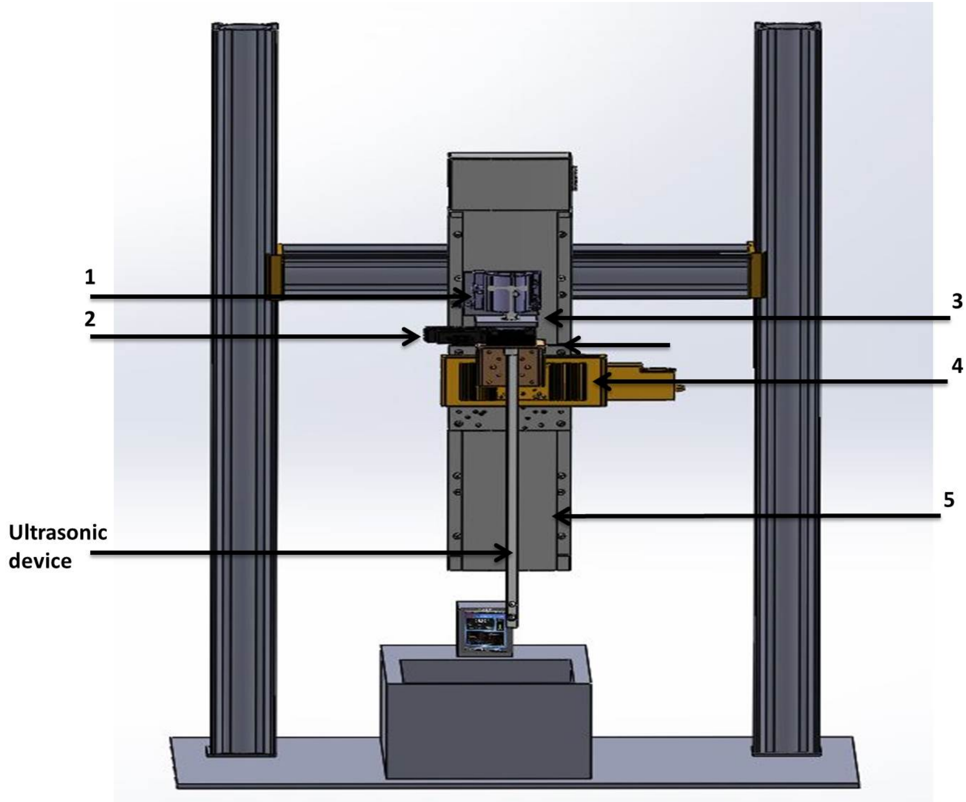

Figure 2.18: Measurement bench design: (1) ULM-TILT, (2) rotational motor, (3) mounting support, (4) dual translation plates, (5) translation plate.

To ensure the precited movement of the ultrasonic device, this latter is inserted in a containing piece assuring its relation to a first element called ULM−TILT and presented as the element 1 in figure 2.18. This element provides two axes of angular adjustment, namely R(x) and R(y) and allows a tilt control of ± 4.5 °.

The ULM−TILT element is related to a rotational motor, the element 2 in figure 2.18, in which the ultrasonic device is inserted. This motor allows the R(z) movement with a resolution of 0.00016 ° and a unidirectional reproducibility of 0.002 °. It is fixed on a mounting support, the element 3 in figure 2.18, with a central opening for the ultrasonic device insertion.

The mounting support is fixed on dual translation plates, the element 4 in figure 2.18. These plates are perpendicularly linked in order to assure the T(x) and T(y) translations. Finally, the whole structure is placed on a translation plate, the element 5 in figure 2.18, assuring the T(z) movement with a 1.25 μm resolution.

A controller allows the monitoring of all of these aforesaid elements. It is also configured to be controlled by the acquisition program. This mechanical system has been mounted in the laboratory and allows measurement experiences with a precised monitoring of the ultrasonic device positioning.

In a view to assure the ultrasonic device height in-situ monitoring along inter-plate distance measurements, a new component was included in the measurement bench and is described in the following section.

2.4.2 Linear cable sensor

New components were related to the ultrasonic device in order to identify the blade emplacement inside the element interstice. These elements are:

- Linear cable sensor: It consists mainly in an incremental encoder and a linear cable of 5 m. While the cable is related to the device introduced between the plates, the coder allows the monitoring and recording of the blade vertical position with a resolution of 0.05 mm. It is presented on figure 2.19 (b).
- High-speed counter and position indicator: This element consists in the NI−9411 card and allows the retrieving of the linear cable sensor signal. It makes the transmission of positions to the acquisition system with an update rate of 500 ns. It is presented on figure 2.19 (a).

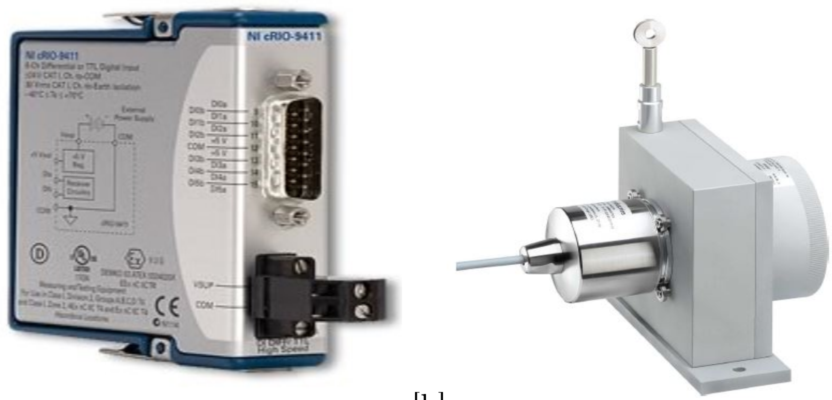

[a] [b]

Figure 2.19: (a) NI−9411 card for counting and position indicating; (b) Linear cable sensor.

The positioning element was installed in the laboratory experimental bench in a way to quantify its precision. It was then tested and integrated in the acquisition program, thus allowing a direct relation between each acquisition and the corresponding blade position with a precision of 100 μm. An image of the full experimental bench of the laboratory is presented in the following figure 2.20.

Figure 2.20: Laboratory experimental bench.

2.5 Conclusion

This chapter has presented in details the new prototype of the high frequency ultrasonic device, allowing the measurement of the water channel thickness variations inside the RHF fuel element. It consists of two ultrasonic transducers both implemented on one unique silica support, consequently allowing an improved precision distance measurement. The transducers' frequency has been investigated in a way to obtain the best resolution, considering the acquisition noise and attenuation sources.

The ultrasonic device, with a thickness of 1 mm, was designed and will be introduced between two fuel plates thanks to a manipulating holder. Its 750 mm height will permit to inspect more than the half of the fuel element. Moreover, the convenient electrical cable length has been modeled and optimized according to the ultrasonic signals acquisition, in a way that will clearly allow to distinguish the electric and the acoustic echoes. Furthermore, the device vertical position inside the element will be controlled with a linear cable sensor. A whole ultrasonic device measurement bench was also designed and will allow the specific characterization of each axis influence on distance measurements and the adequate positioning of the ultrasonic device.
In the following chapter, the developped device applied to distance measurements and the signal processing are presented.

Chapter 3

Distance measurement concept

Contents

3.1 Introduction **62**

3.2 Time of flight measurement **62**

3.2.1 Introduction 62

3.2.2 Time of flight measurement signal processing methods . . 63

3.2.3 Multiple echoes cross-correlation 64

3.2.4 Time of flight applied measurement concept 65

3.3 Ultrasound velocity measurement **71**

3.3.1 Introduction 71

3.3.2 Ultrasound velocity measurement methods 71

3.3.3 Ultrasound velocity measurement method applied 71

3.4 Conclusion **76**

3.1 Introduction

To measure the inter-plate distance, reflected signals are subjected to a specific signal processing. Indeed, two parameters need to be evaluated for distance evaluation, namely the time of flight and the ultrasonic velocity. First, an overview of the signal processing methods allowing either the time of flight or the ultrasonic velocity estimations are exposed. Then, the proposed methods applied in this current case are presented and developed.

3.2 Time of flight measurement

3.2.1 Introduction

For ToF estimation, the pulse echo method is applied. Indeed, the transducer is mainly composed of the piezoelectric element and the silica support. The interface silica/water implies reflections, constituting a first echo series received by the transducer. Its complementary is then completely transmitted through the water, and reflects on the plate. The principle is presented in figure 3.1.

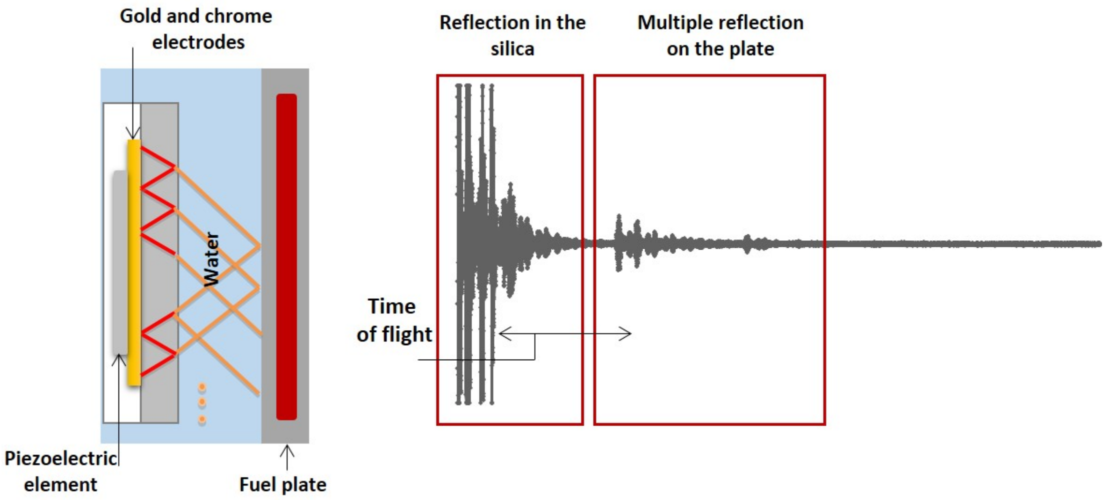

Figure 3.1: Ultrasonic wave propagation through the mediums and the corresponding acquired signal including two echo series.

For inter-plate distance estimation, the distance to be measured by each ultrasonic transducer constitutes the interval distance between the silica support interface with the water and the water interface with the fuel plate. In this view, the time of flight to be investigated is the time between the first echo series reception and the second echo series reception.

3.2.2 Time of flight measurement signal processing methods

For the time of flight estimation, several signal processing methods can be applied. The main useful ones are briefly presented in the following.

Signal Envelope method

The signal envelope method consists in using the analytical signal of the experimental signal. This latter is calculated by the Hilbert Transform and its modulus permits to obtain the envelope of the experimental signal. This envelope method allows the elimination of the negative parts of the signals and smooths both echo series. An identification of both the series maximum peaks would allow a time-of-flight estimation.

For the current ToF evaluation, the envelope method can be employed. However, it has been found that the first echo series include electrical echoes that should not be considered. The envelope method can unfortunately lead to inaccurate ToF estimations.

Curve-fitting method

Time of flight measurements can be achieved through the curve fitting method. This latter employs a nonlinear least-squares method to calculate a fitting curve according to the received acoustic echo onset. The calculated curve consists in a parabolic curve of the form $a_0*(t - t_0)^2$ fitted to the signal envelope around the rising echo edge. In this view, both the parameters t_0 and a_0 are estimated.

While for the first parameter estimation a thresholding method is applied [62], the second parameter estimation is realized through the second derivative approximation around the threshold point. Employing both parameters, an iterative numerical method is exploited: the Levenberg-Marquardt nonlinear least-squares method [63].The final value obtained for t_0 is taken as the ToF.

The curve-fitting method depends mainly on the thresholding step. Assuming high frequency signals, the thresholding method is highly influenced by the noise, therefore impacting the ToF measurements.

Cross-correlation method

Cross-correlation is a standard method to estimate the similarity between two series [64] [65] [66]. For ToF achievement, this similarity degree is calculated through the correlation between the two received signals. It allows the determination of the time delay. This method advantages mainly consist in its high robustness over the random noise and its significant measurement resolution.

Knowing that the transducer structure implies two echo series and assuming the high accuracy of the cross-correlation method, this latter is employed for inter-plate distance estimation.

In the signals presented in figure 3.1, the presence of the silica support implies multiple reflections of the ultrasonic signals on the silica/water interface. In the following is presented a comparison between the time of flight estimation with and without the silica support presence.

3.2.3 Multiple echoes cross-correlation

To compare the ToF estimation for both the cases with and without the silica support presence, the time delay corresponding to the distance to be measured is noted θ.

In the first case, the reflection is realized directly on the fuel plate interface. The time of flight is then calculated through the cross-correlation between the excitation signal $x(t)$ and the echo reflected by the fuel plate $y(t)$. The equation displaying the cross-correlation is:

$$R_{xy}(t) = x(t) \otimes y(t) = \int_{-\infty}^{+\infty} x^*(\tau) * y(t+\tau)\,\mathrm{d}\tau. \tag{3.1}$$

The second case includes the presence of the silica support. Consequently, multiple reflections occur on the silica/water interface. Indeed, $x(t)$ and $y(t)$ are series constituted of several echoes such as $x(t) = \Sigma_{i=1}^{n} x_i(t)$ and $y(t) = \Sigma_{j=1}^{n} y_j(t)$.

Noting the time of flight in the silica support as $t = \tau$, the parameters are then $x_i(t) = a_i s(t - i\tau)$ and $y_j(t) = b_j s(t - j\tau - \theta)$ where a_i and b_j are the echoes' amplitudes of the elementary bursts s(t). The cross-correlation is then realized between the first echo series and the second echo series. The equation displaying this cross-correlation is presented in the following (3.2):

$$R_{xy}(t) = \Sigma_{i=1}^{n} x_i(t) \otimes \Sigma_{j=1}^{n} y_j(t), \tag{3.2}$$

$$R_{xy}(t) = \Sigma_{i=1}^{n} \Sigma_{j=1}^{n} a_i b_j s(t - i\tau) \otimes s(t - j\tau - \theta). \tag{3.3}$$

Compared to the previous correlation $abs(t) \otimes s(t - \theta)$ of two single bursts of amplitudes a and b separated by the time of flight θ, the maximum of similarity of the two composite signals is strenghtened through the contribution of each pair of bursts increasing the signal to noise ratio in the correlation result. In other terms, the more reflections available and considered, the more accurate the correlation result.

3.2.4 Time of flight applied measurement concept

The signal processing adopted for the time of flight evaluation is here developed. After the ultrasonic device insertion in water, the same signal processing steps are applied to both the ultrasonic transducers' signals. These steps are presented hereafter. At each step, signals are displayed in a way to illustrate the impact of each process.

Signal bandpass filtering

The ultrasonic device is first inserted in water environment. For each transducer, the ultrasonic signal is acquired with a sampling frequency of F_{sam}=2.5 GHz. A digital filtering is then applied to this signal according to the transducer bandwidth. The filtering result is visualized in figures 3.2 (a) and (b).

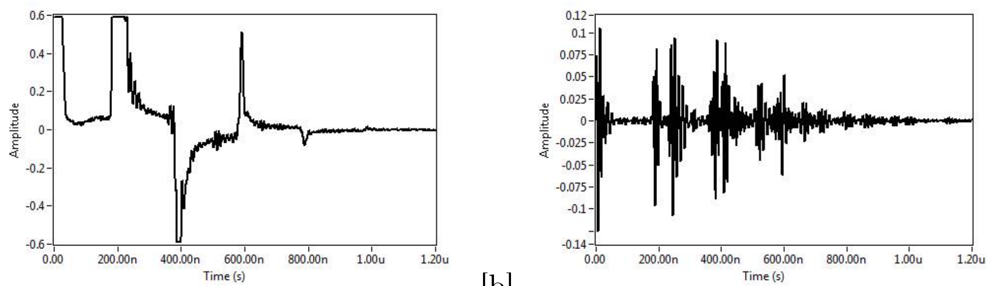

[a] [b]

Figure 3.2: (a) Acquired ultrasonic signal before bandpass filtering; (b) Acquired ultrasonic signal after bandpass filtering.

The numerical filtering remains necessary to decrease the noise and to identify the acoustic echoes. The ultrasonic transducer signature, presented in figure 3.2 (b) is then recorded. It constitutes the reference ultrasonic signal and consists in the first main element for the cross-correlation measurement.

Signal energy measurement

Secondly, the ultrasonic device is inserted in a silica sample consisting of a predefined interstice distance. The transducers' orientation is controlled to optimize the amplitude of the received signals, corresponding to an alignment of the acoustic beam with the normal to the silica sample surface. An example of a maximum alignment allowing three reflected echo series from the facing surface is presented in figure 3.3. For each signal $S(t)$ similar to that of figure 3.3, the energy is computed thanks to the following equation (3.4).

$$E(S(t)) = \sum_{i=1}^{n} (x_i(t))^2. \tag{3.4}$$

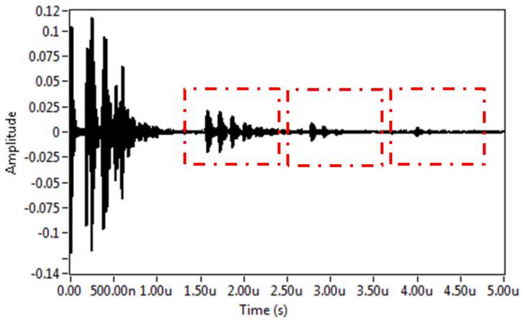

Figure 3.3: An ultrasonic signal with three reflected echo series from the facing sample surface.

where $x_i(t)$ is the echo amplitude of the elementary burst (see equation 3.4).
This energy estimation will be used in the following to fix a threshold allowing the selection of adequate ultrasonic signals.

Reference signal subtraction

For time of flight evaluation, the signal processing consists in the cross-correlation between the series of echoes coming from the silica/water interface, denoted as SW series, and that coming from the water/plate interface, denoted WP series.
Two cases can be observed and are displayed in the following figures 3.4 (a) and (b).

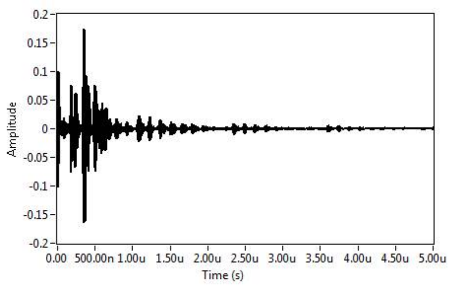

[a]

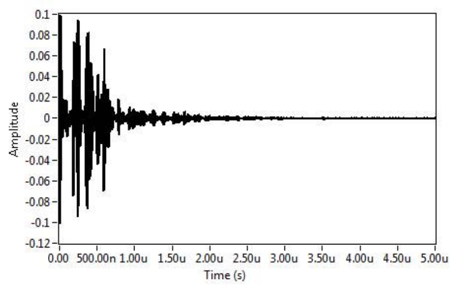

[b]

Figure 3.4: (a) Acquired ultrasonic signal with distinguished reflected series; (b) Acquired ultrasonic signal with overlapped reflected series.

For the first experimental signal of figure 3.4 (a), the two series are completely separated, yielding an easy identification of the time of flight. The second signal of 3.4 (b) displays an overlapping that occurs between the SW and the WP echo series because of the close positioning of the ultrasonic transducer with the facing surface. To overcome this problem, it is here proposed to subtract from these signals the reference signal of figure 3.2. The results are presented in figures 3.5 (a) and (b).

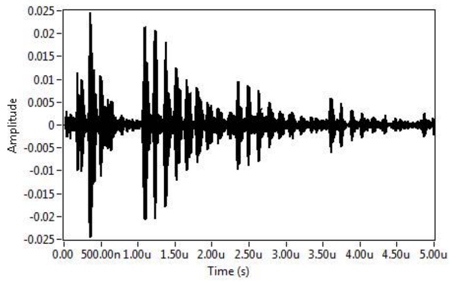

[a]

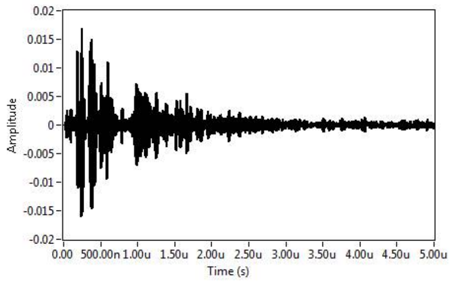

[b]

Figure 3.5: (a) First case ultrasonic signal after reference signal subtraction; (b) Second case ultrasonic signal after reference signal subtraction.

- For the first case, it is clearly observed that the subtraction does not allow a total removal of the SW series, leaving a residual part.
- For the second case, not only the residual part is still present but it interferes with the beginning of the WP echo series.

To understand the origin of this problem, a comparison between the reference signal and the SW series of each experimental signal is realized and displayed in the figures 3.6 (a) and (b). Figure 3.6 (a) displays the superposed signals in lines where figure 3.6 (b) displays one time period of both the signals in points.

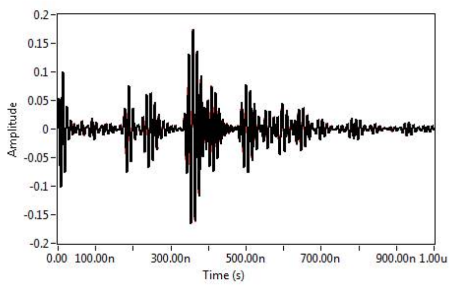

[a]

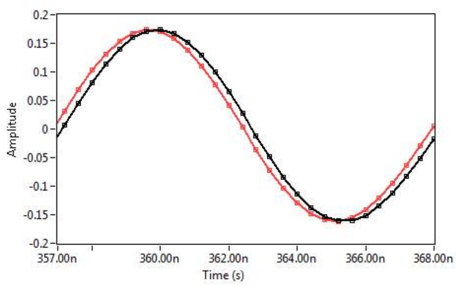

[b]

Figure 3.6: (a) Supperposition of the acquired ultrasonic signal and the reference signal; (b) One time period of both the signals in points.

A first visualization of the signals superposition in figure 3.6 (a) suggests that they perfectly match. However, on figure 3.6 (b), a shift is clearly observed. This is due to a non synchronization of the electronic trigger with the sampling frequency.

The fact that the whole signal is delayed would lead to the cross correlation between a non-delayed reference and a delayed experimental signal. Consequently, the time of flight measurement is inaccurate as presented in the graph of figure 3.7 where a step-like structure can be observed. It is linked to this non-synchronization. Knowing that the adequate time of flight is 2.4 μs, two inaccurate time of flight are observed: 2.39 μs and 2.25 μs. These results are explained here.

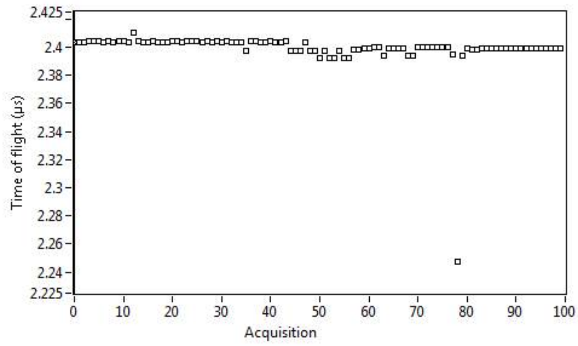

Figure 3.7: Time of flight measurement results.

- Knowing that the analyzed transducer central frequency is of $F_c = 90$ MHz, the first one corresponds to an artificial time of flight equal to $1/F_c = 0.01$ μs leading to time of flight values of 2.39 μs in figure 3.7.
- The second one corresponds to a propagation in the silica support equal to 0.145 μs leading to time of flight values of 2.25 μs in figure 3.7.

To limit these errors, a numerical method has been developed and allows the constitution of the convenient reference signal. It is bazed on the signal oversampling and is presented in the following.

Signal oversampling

- Oversampling of the reference signal with a factor 200, which corresponds to an artificial sampling frequency of F$_{subsam}$ = 500 GHz. Reference echoes before and after the oversampling are superposed in figure 3.8.

[a] 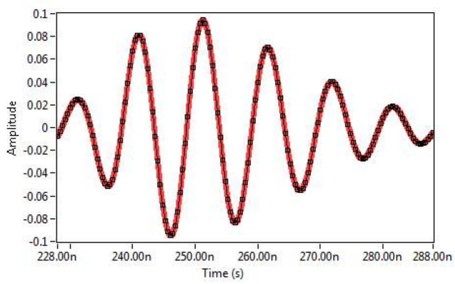

[b] 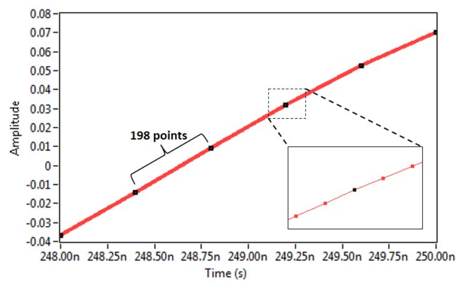

Figure 3.8: An ultrasonic signal superposed with its oversampled signal, (a) ultrasonic echo, (b) a zoom over 2 ns.

- Due to the oversampling, 198 points are artificially inserted between each pair of points. Sub-sampled signals are then extracted and substracted to the experimental signal. The signal with the smallest residue is then considered as the local reference signal.

These previous steps are applied to both cases previously presented on figures 3.5 (a) and (b). Results of both cases are displayed on figures 3.9 and 3.10.

First case

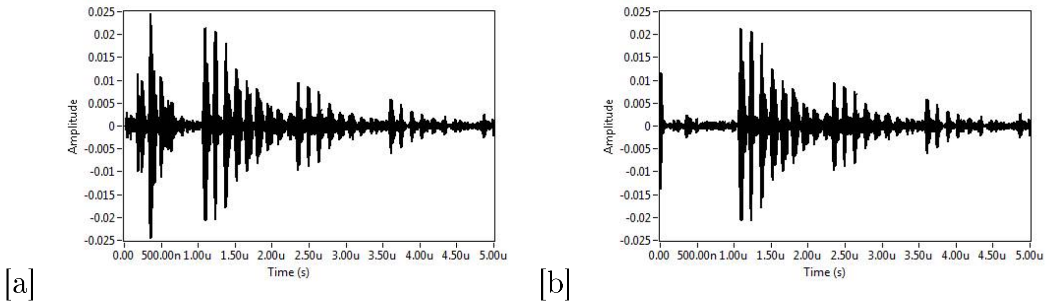

Figure 3.9: First case after reference signal subtraction; (a) without oversampling, (b) with oversampling.

For the first case, the SW echo series is appropriately removed from the experimental signal. The WP echo series is therefore correctly extracted. A negligible residual part can be observed on the beginning of the subtracted signal. It is mainly due to the electrical saturation of the acquisition cards but does not affect the following steps.

Second case

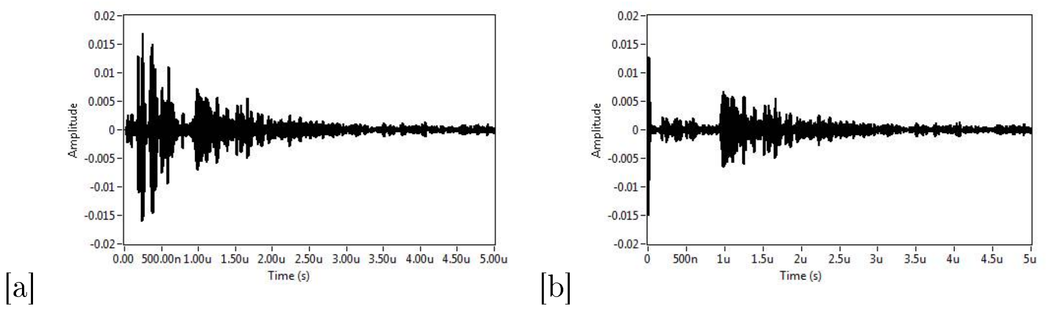

Figure 3.10: Second case after reference signal subtraction; (a) without oversampling, (b) with oversampling.

For the second case, the SW echo series has also been adequately eliminated. The most important advantage of this oversampling subtraction operation is demonstrated through the second part of the resulting signal. Indeed, the beginning of the second echo series, initially completely covered is now clearly identified.

- This oversampling before subtraction is then used, in the following of the manuscript where its profits will be proved.

Cross-correlation operation

After the adequate subtraction of the reference series from the experimental signal, the cross-correlation operation can be applied. The artificial reference sub-series, considered as the most convenient reference for the SW echo series subtraction, is employed as a local reference signal for the cross-correlation.

In a way to verify the cross-correlation results, the reference signal is delayed by the time identified by the cross-correlation operation. Then, it is superposed on the experimental signal after the reference subtraction. A graph with both the signals superposed is presented in the following figure 3.11.

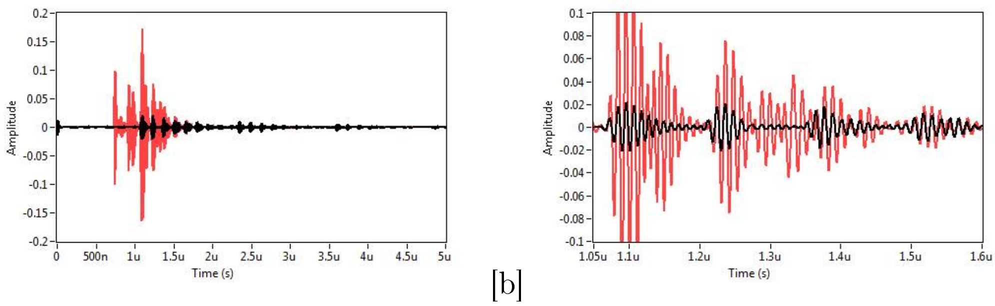

[a] [b]

Figure 3.11: Superposed reference and experimental signals: delayed reference signal in red and subtracted signal in black, (a) visualization of complete signals (b) a zoom on the WP series.

The superposition of the signals allows the verification of the quality of the cross-correlation operation. Indeed, from this superposition, it is displayed that the acoustical echoes of the SW echo series match with the ones of the WP echo series without being disturbed by the electrical echoes, with shapes different from those of the acoustic echoes. They are positioned at the beginning of the red signal of the figure 3.11 and are not considered as relevant by the cross-correlation.

3.3 Ultrasound velocity measurement

3.3.1 Introduction

For inter-plate distance estimation, the second element to be measured is ultrasound velocity, knowing that the medium to be crossed by ultrasonic waves is demineralized water. Several methods are available to estimate that ultrasound velocity.

In the following, an overview of the ultrasound velocity measurement methods is first displayed. Then, the applied one is presented and developed.

3.3.2 Ultrasound velocity measurement methods

Temperature-velocity relation

Assuming a direct relation between the temperature and the velocity parameters of a fluid, the temperature measurement can be employed to infer the ultrasound velocity. Several temperature measurement methods are available. The most famous devices are: thermocouples [67] [68], thermal resistances [69], and optical devices[70]. According to the experiment, only the thermocouples can be immersed and positionned next to the measurement area. Indeed, the thermocouples analyze temperatures over wide ranges from -180 to 2320 °C. Moreover, they are acknowledged for their high robustness, their miniaturized diameters, and their high tolerance.

For local temperature estimations, introducing an additional sensor with the ultrasonic device in the experimental area, such as thermocouples, remains problematic. Moreover, evenif this proposition is supposed available, the differences in the emplacement of both types of sensors could lead to some errors.

In these conditions, an ultrasound velocity measurement method has been developed with the main advantage of employing the ultrasonic device. The theoretical part of this method is first discussed before further displaying the experimental setup.

3.3.3 Ultrasound velocity measurement method applied

The ultrasound velocity-temperature relation

The influence of the temperature on the sound velocity has already been confirmed in the literature. According to [71], the velocity dependence on the temperature can be computed as in the following equation 3.5:

$$c = a_0 + a_1T + a_2T^2 + a_3T^3 + a_4T^4 + a_5T^5, \tag{3.5}$$

such as the a_i coefficients are given in the following table 3.1:

Coefficient	a$_0$	a$_1$	$10^2 * a_0$	$10^4 * a_3$	$10^6 * a_4$	$10^9 * a_5$	Error	$°C$ range
Value	1402.388	5.037	-5.808	3.342	-1.478	3.146	0.002	0 - 100

Table 3.1: Coefficients of the polynomial approximation of the temperature dependance of the ultrasonic velocity in water.

The ultrasound velocity variation curve in function of the experimental temperature range, according to the previous equation 3.5 is presented in the graph 3.12.

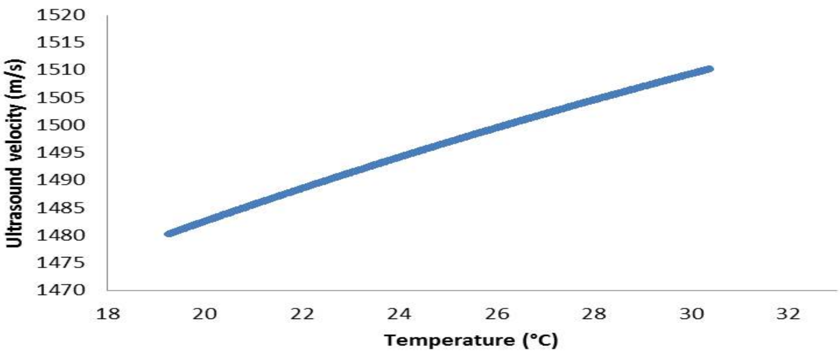

Figure 3.12: Ultrasound velocity in function of temperature.

Thanks to the previous curve 3.12, the ultrasound velocity will be calculated after the water temperature identification.

The temperature measurement theory

The thermal expansion of the transducer layers is affected by the temperature. From their thicknesses, the chrome, gold, adhesive and aluminum layers are negligible in comparison to those of the silica support and the piezoelectric element. While the piezoelectric element thermal expansion coefficient ranges between $\alpha_{LiNbO_3} = 7.5 * 10^{-6}$ /°C and $\alpha_{LiNbO_3} = 15 * 10^{-6}$ /°C [72], the silica thermal expansion is of $\alpha_{SiO_2} = 4.1 * 10^{-7}$ /°C [73] [74]. This means that the silica thermal expansion is negligible according to that of the piezoelectric element.

Assuming that the piezoelectric element manifests a thermal expansion α_{LiNbO_3}, its thickness is modified in function of the medium temperature. Moreover, this has an influence on its resonance frequency. In order to investigate the frequency-temperature equation [51], the resonance frequency is first related to the piezoelectric element velocity V and its thickness d according to the following equation 3.6:

$$f = \frac{V}{2d}. \tag{3.6}$$

The frequency variation $\delta f/f$ is then calculated as the following:

$$\frac{\delta f}{f} = \frac{\delta V}{V} - \frac{\delta d}{d}. \tag{3.7}$$

Each part of the equation 3.7 is further developed.

The piezoelectric element velocity is related to its young modulus E and its density ρ by $V = \sqrt{\frac{E}{\rho}}$. Consequently, the first part is expressed thanks to equation 3.8:

$$\frac{\delta V}{V} = 1/2(\frac{\delta E}{E} - \frac{\delta \rho}{\rho}). \tag{3.8}$$

- The young modulus is related to elastic moduli S_{11} as $E = 1/S_{11}$ [75]. Knowing that a is temperature coefficient in a range of $[0.8 - 8.9] * 10^{-4}/°C$ [76]:

$$\frac{\delta E}{E} = -\frac{\delta S_{11}}{S_{11}} = -a\delta T. \tag{3.9}$$

- The piezoelectric element density is as: $\rho = \frac{m}{v}$. Knowing that the piezoelectric element volume is expressed as $v = v_0(1 + \gamma\delta T)$, with $\gamma = 36.5 * 10^{-6}/°C$ the volume expansion coefficient [77], the density variation is under equation 3.10:

$$\frac{\delta \rho}{\rho} = -\gamma\delta T. \tag{3.10}$$

According to both the equations 3.10 and 3.9, the first part of the equation 3.7 is:

$$\frac{\delta V}{V} = -1/2 * (a - \gamma)\delta T. \tag{3.11}$$

The second part of the equation 3.7 concerns the variation of the piezoelectric element thickness $\frac{\delta d}{d}$. Indeed, at a constant pressure the piezoelectric element thickness is modified according to the thermal expansion law [78] [79] as in the following:

$$\delta d = \alpha * \delta T * d(T_0). \tag{3.12}$$

Consequently, the thickness variation is expressed as in the following equation 3.13:

$$\frac{\delta d}{d} = \frac{\alpha * \delta T}{1 + \alpha * \delta T}. \tag{3.13}$$

According to equations 3.11 and 3.13, frequency variation of equation 3.7 becomes:

$$\frac{\delta f}{f} = -1/2 * (a - \gamma)\delta T - \frac{\alpha * \delta T}{1 + \alpha * \delta T}, \tag{3.14}$$

$$\frac{\delta f}{f} = -1/2 * (a - \gamma + \frac{2 * \alpha}{1 + \alpha * \delta T})\delta T. \tag{3.15}$$

Thanks to the previous equation 3.15, the frequency variation is expressed in function of the temperature variation. Consequently, knowing the frequency allows the estimation of the water temperature and obviously the ultrasonic velocity. In a way to obtain a local ultrasonic velocity estimation, an experimental method based on a local temperature estimation has been developed.

In the following, the simulation curve of frequency in function of temperature is compared to an experimental curve realized with a laboratory measurement bench.

The ultrasound velocity experimental measurement

Measurement bench

To identify temperature dependance of the transducer frequency, a measurement bench has been developed. It consists of the previous ToF acquisition system joined to a specific temperature bath that allows the water temperature modification. This measurement bench is employed to verify the simulation curve. The water variation bath allows the variation of the temperature with a step of 0.02 °C. An image of the temperature measurement bench is presented on the figure 3.13.

Figure 3.13: Temperature measurement bench.

Frequency variation measurement concept

In order to evaluate the ultrasonic transducer frequency variation in function of the temperature, one echo is studied and displayed on the figure 3.14 (a). The measurement of the corresponding resonance frequency is then realized through the Fast Fourier Transform presented in figure 3.14 (b).

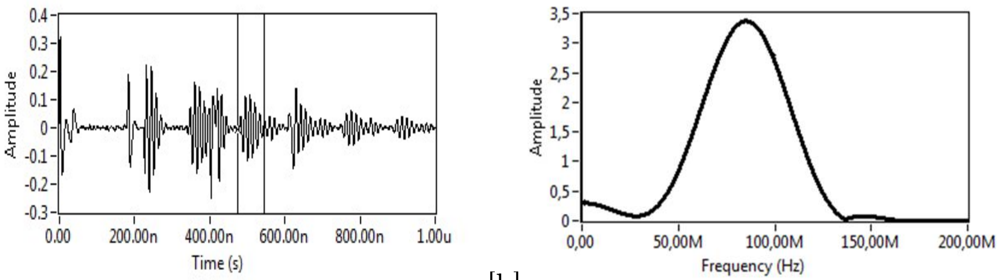

[a] [b]

Figure 3.14: Ultrasonic signals received by the transducer 1 (a) and the transducer 2 (b) under the first device positioning 1.

The resonance frequency of the ultrasonic transducer is then monitored while varying the temperature of the water medium. This experiment enables to come up with an experimental curve of the frequency variation in function of the temperature variation. This experimental curve is compared to the frequency variation simulation curve for which the employed temperature coefficient value is $a = 8 * 10^{-4}$, the expansion coefficient value is $\alpha = 15 * 10^{-6}$ and the volume expansion coefficient is $\gamma = 36.5 * 10^{-6}$. Both curves are presented in figure 3.15.

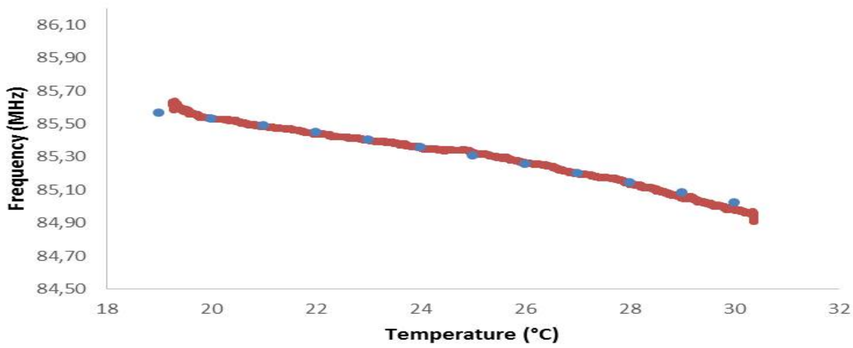

Figure 3.15: Frequency variation according to the temperature. Blue squares correspond to the simulated values and red points to the experimental data

On the previous graph, a good concordance between simulated and experimental values can be observed. This curve is realized for each ultrasonic transducer and enables to retrieve the temperature according to the in-situ and real-time frequency estimation experiments.

The previous curve of figure 3.12 allows then the determination of the in-situ ultrasound velocity corresponding to the identified temperature. As a consequence, a curve of the ultrasound velocity variation in function of the central frequency variation can be obtained. It is presented in figure 3.16.

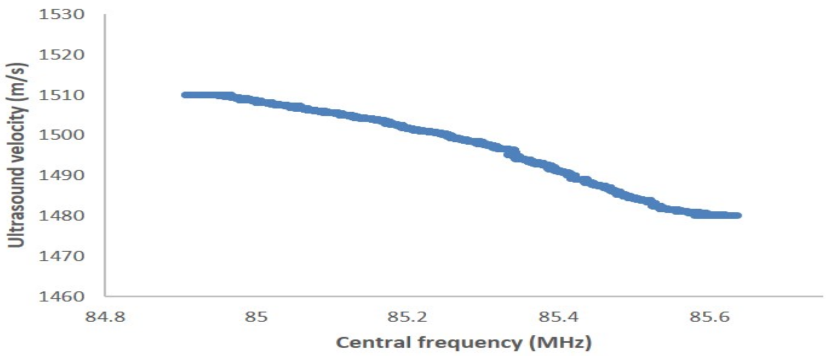

Figure 3.16: Ultrasound velocity in function of central frequency.

After the ToF and the ultrasonic velocity evaluation, the inter-plate distance estimations will be performed in the following chapter to validate the developed methods.

3.4 Conclusion

In the framework of inter-fuel-plate distance evaluation, a new non-destructive high frequency ultrasonic device has been developed and its measurement chain was optimized.

The signal processing must allow the determination of two parameters: the ToF and the ultrasonic velocity. For the ToF, the measurement process has been optimized. Indeed, the energy parameter has been introduced to select the adequate signals for the distance measurements. The SW echo series subtraction has been optimized thanks to the signal oversampling, corresponding to a numerical sampling frequency of 500 GHz. Finally, the echo type identification, either electrical or acoustical, allows the optimization of the cross-correlation and obviously the time of flight evaluation. For the ultrasound velocity, the new ultrasonic device simultaneously allows the identification of this second main parameter. Indeed, the ultrasonic velocity is directly related to the temperature. Consequently, this latter has been investigated and a relevant link was established with the transducer resonance frequency, leading to the elaboration of an experimental relation between frequency and temperature.

After the distance signal processing development, the following step is the validation of the distance measurement concept through reproducibility and reliability experiences presented in the following chapter.

Chapter 4

Proof-of-concept and reproducibility measurements

Contents

4.1 Introduction 78

4.2 Inter-plate distance variation measurements 78

4.3 Device structure and transducers parallelism 80

4.3.1 Effect of $\Theta = 1\,°$ over the distance measurement 81

4.4 Measurement reproducibility study 82

4.4.1 Configuration 1: Optimized transducer 1 alignment. . . . 82

4.4.2 Configuration 2: Optimized transducer 1 alignment with a velocity decrease of a factor of 10. 83

4.4.3 Configuration 3: Optimized transducer 2 alignment. . . . 84

4.4.4 Configuration 4: simultaneous transducers alignment compromise. 85

4.4.5 Configuration 5: Second measurements with simultaneous transducers alignment compromise. 86

4.4.6 Reproducibility measurements conclusion 88

4.5 RHF model inter-plate distance reproducibility measurements 88

4.5.1 Modeling of the device positioning in the RHF element . . 88

4.5.2 RHF model experiments 90

4.6 Conclusion 92

4.1 Introduction

After the presentation of the distance measurement principle, here are presented reproducibility and reliability experiences. For this, inter-plate distance is estimated on several samples. They were manufactured to allow the estimation of the ultrasonic device measurement accuracy and resolution. In this view, the device is tested under a process of three steps:

- the first one allows the validation of the device ability to detect defined distance variations,
- the second one is employed for reproducibility estimation on a distance representative of the water channel thickness,
- the third one consists in a RHF fuel element model available in the laboratory, including the involute shape constraint.

4.2 Inter-plate distance variation measurements

In a way to first estimate the accuracy of the ultrasonic device on distance variation, measurements have been realized on a first sample. This latter was realized from titanium and includes 4 steps of 50 μm manufactured by electro-erosion [80] assuming a resolution of 1 μm at the Laue-Langevin Institute (ILL). The scheme of this element is presented on figure 4.1 (a). It was first analyzed by optic imaging in a way to visualize the different steps. It is displayed in figure 4.1 (b).

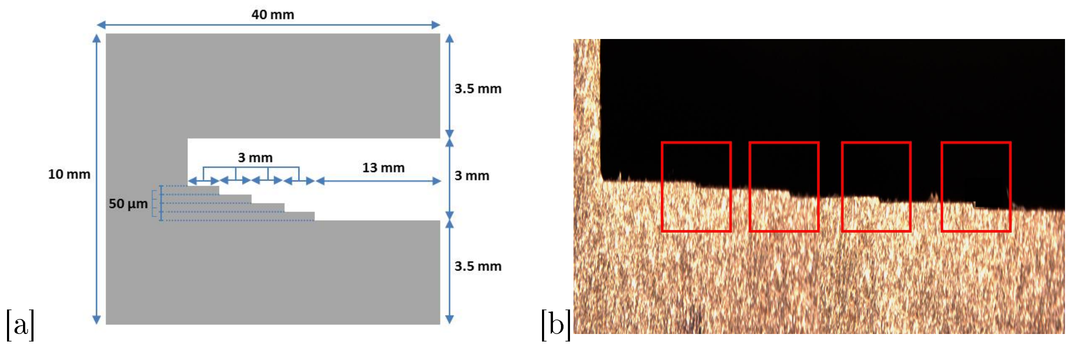

Figure 4.1: (a) Titanium element scheme (b) Optic imaging of the titanium element steps.

On the optical image of figure 4.1 (b), the five abrupt 50 μm steps are clearly observed. To achieve distance measurements over the titanium element with the ultrasonic device, several experimental steps are followed. First the ultrasonic device is introduced in the titanium element in front of the deepest step. Second, its parallelism to this latter step is controlled through the WP echo series reception. Finally, the acquisition program is launched simultaneously with the controlled displacement of the ultrasonic device all along the titanium steps.

For each transducer, distance measurements are realized over the side including the steps. The distance separating the transducer to the first step is then subtracted in order to display relative measurement results. They are presented in figure 4.2.

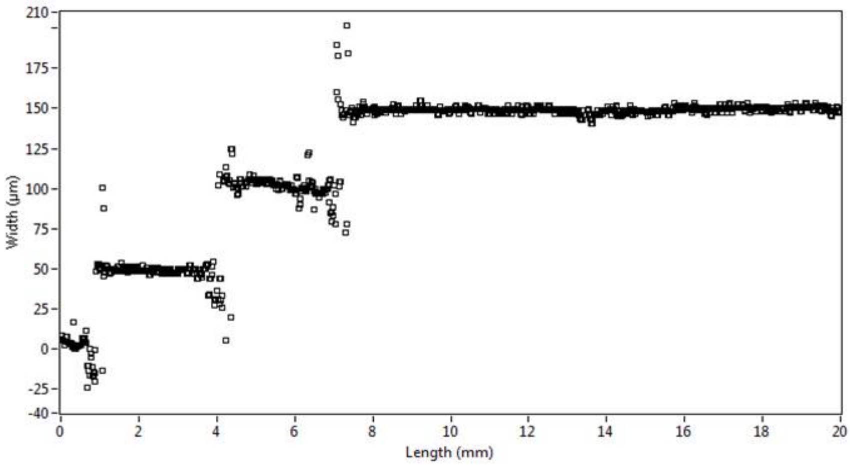

Figure 4.2: Titanium element relative measurements.

First, on figure 4.2, four of the five 50 μm steps of titanium element are clearly observed. In fact, due to the first step length of 3 mm and the transducer manufacturing, the first step cannot be observed. Then, between each pair of steps, namely around the variation emplacements, aberrant values are displayed. These values are due to the 50 μm abrupt variation of the width, inducing either diffraction or interference phenomena. Such abrupt variations are not present in the fuel element but are clearly required for transducer characterization.

For the first step, the measurements manifest a standard deviation of $\sigma = 2.2$ μm and an average difference distance of $\Delta d_1 = 47$ μm with the second step. This second step is estimated with a standard deviation of $\sigma = 2.9$ μm and an average difference distance of $\Delta d_2 = 51$ μm with the third one. While the third step shows a $\sigma = 3$ μm standard deviation, its average difference to the fourth step is of $\Delta d_3 = 48$ μm. Finally the fourth step displays a standard deviation of $\sigma = 1.9$ μm.

To conclude, this first measurement experiment over the step-composition titanium element enables the confirmation of the high ultrasonic device ability to detect width variations. The 50 μm steps were clearly observed with a general resolution of 3 μm during the positioning system displacement.

After this first validation, the next step consists in the realization of inter-plate distance reproducibility measurements. For this, the device structure is first analyzed.

4.3 Device structure and transducers parallelism

In a view to analyze the inter-transducer beam alignment, the ultrasonic device is tested on an experimental silica sample with parallel faces and an inter-faces distance of 1800 ± 10 μm. The acquired signals reflected on the faces of the sample allow the analysis of the transducer parallelism. The signals received under a first positioning of the ultrasonic device are presented in figures 4.3 (a) and (b).

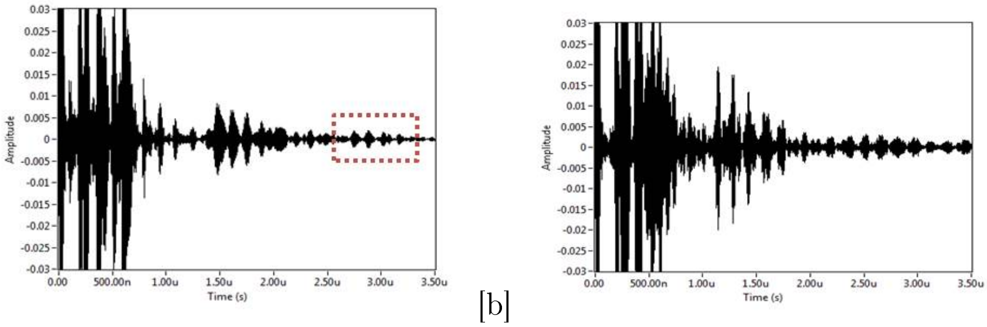

[a] [b]

Figure 4.3: Ultrasonic signals received by the transducer 1 (a) and the transducer 2 (b) under the first device positioning 1.

The two previous figures display the WP echo series of both transducers. The identification of the beginning of the second WP echo series displayed in red on figure (a) confirms the adequate parallelism of the transducer 1 to the sample surface. On the signal of figure 4.3 (b), the second WP echo series are received, however a weak misalignment can be observed between the transducer and the sample face leading to a small amplitude of the echoes.

In a view to quantify this misalignment, a modification of the device positioning is realized in order to improve the alignment of the second transducer. The consequent received signals are presented in the following figures 4.4 (a) and (b). This modification consists in the device rotation with an angle of 1 °.

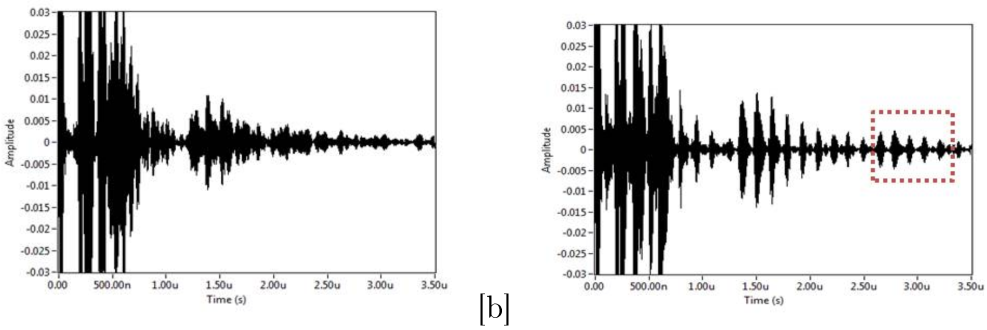

[a] [b]

Figure 4.4: Ultrasonic signals received by the transducer 1 (a) and the transducer 2 (b) under the second device positioning

After the second device positioning, both transducers maintain the WP echo series. On the transducer 2 signal, a distinguished reception and identification of the second WP series are observed, confirming an adequate parallelism to the surface. On the transducer 1 signal, the WP series are clearly influenced, confirming a misalignment as presented in the scheme of figure 4.5.

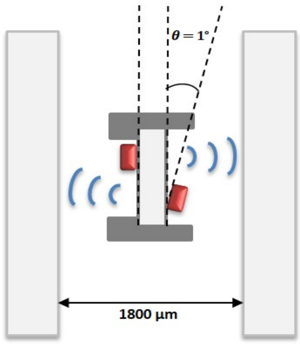

Figure 4.5: Scheme of the ultrasonic device inside the silica sample assuming a $\Theta = 1\,^{\circ}$ transducers' parallelism difference.

To conclude, the above study indicates that the ultrasonic device transducer alignment is achieved with a $1\,^{\circ}$ precision clearly indicating the quality of the manufacturing process. However due to the high precision required in the experiments and the corresponding ultrasonic frequency, this $1\,^{\circ}$ misalignment induces significant modifications in ultrasonic signals' shapes. These effects are quantified hereafter.

4.3.1 Effect of $\Theta = 1\,^{\circ}$ over the distance measurement

The figure 4.6 presents a scheme of a transducer beam misalignment with a facing surface.

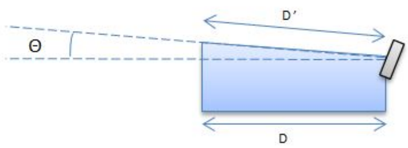

Figure 4.6: Scheme of the ultrasonic transducer positioning.

Under the misalignment of $\Theta = 1\,^{\circ}$, the distance D' previously presented is:

$$D' = \frac{D}{cos(\Theta)}. \tag{4.1}$$

With a maximal value of D equal to 1400 μm:

$$D' = \frac{1400}{cos(1)}, \tag{4.2}$$

$$D' = 1400.3\ \mu m. \tag{4.3}$$

Consequently, a measurement effect on distance due to transducers' misalignment is of $e = 0.3\ \mu m$. Considering the project objective, this effect is found negligible.

4.4 Measurement reproducibility study

To evaluate the system reproducibility, five measurement series were realized the same day and at the same position in the sample, in three different configurations of the transducers positioning inside the water channel:

1. Alignment optimization of one transducer (referred to as transducer 1),
2. Alignment optimization of the second transducer (transducer 2),
3. Mean alignment over both the transducers.

This positioning study aims to quantify the transducer alignment impact over the reproducibility of distance measurements. To simulate the final conditions, this study is realized on a silica sample representing a 1.8 mm water channel. The distance measurements are realized on distances of at least 1 cm length. The measurement conditions are here presented and the results are interpreted.

4.4.1 Configuration 1: Optimized transducer 1 alignment.

During the first measurement series, 10 device ascending and descending movements were realized on a 1 cm zone in the sample center. The thickness measurement at each vertical position are indexed and are presented in figure 4.7. The ascending measurements are presented in points and the descending ones are showed in circles.

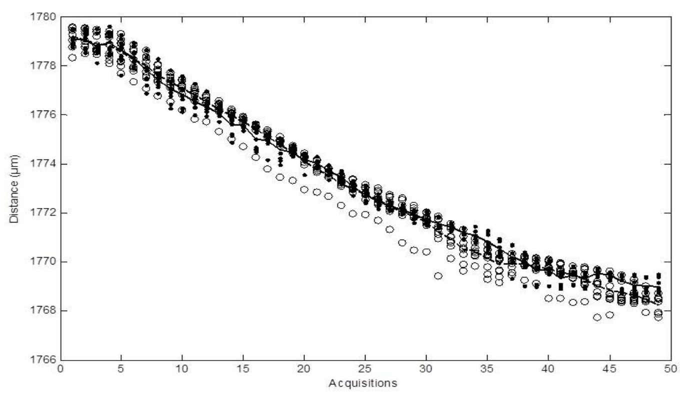

Figure 4.7: Configuration 1 measurement results.

The results presented in figure 4.7 imply that the water channel thickness decreases in a quasi-linear way. On the studied zone, the thickness average value is identified at 1773.26 μm with a local standard deviation of 3.40 μm and a global variation over the 1 cm of 11.90 μm. For each position, the measurements realized during the device ascending and descending movements are situated in a maximum vertical interval of 2 μm.

The quality of the above result indicates that the transducer's alignment is not influenced by the positioning of the device.

These elements imply that, in this experimental configuration, the water channel thickness is estimated with a precision of 2 μm.

4.4.2 Configuration 2: Optimized transducer 1 alignment with a velocity decrease of a factor of 10.

During these experiments, one device ascending and descending movement was realized over the same zone with a reduced device displacement velocity allowing ten times more measurements. The measurement results are presented on the following figure 4.8.

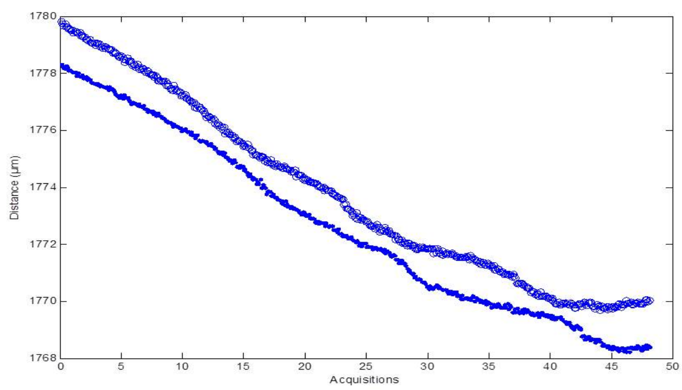

Figure 4.8: Configuration 2 measurement results.

These results confirm the linear decrease of the water channel thickness measurement. The average value is equal to 1773.18 μm with a global variation of 11.59 μm and a standard deviation of 3.13 μm.

Results of configurations 1 and 2 are superimposed in the following figure 4.9 and then compared.

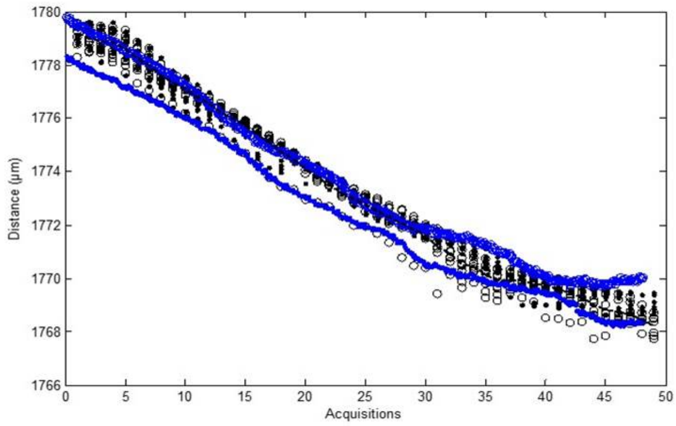

Figure 4.9: Configurations 1 and 2 measurement results.

The comparison of both configurations presents an average values' difference of 0.08 μm and a perfect concordance of the standard deviation and the global variation results. The reproducibility over the ascending and descending movements of the configuration 2 is in a 2.2 μm interval, in concordance with the configuration 1 values.

This reproducibility confirms the non-influence of the motors displacement velocity over thickness measurements.

4.4.3 Configuration 3: Optimized transducer 2 alignment.

A third measurement series was realized over the same zone by optimizing the transducer 2 alignment. The results are presented in figure 4.10.

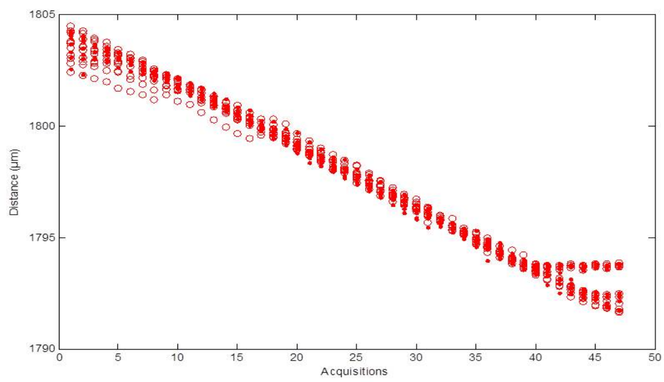

Figure 4.10: Configuration 3 measurement results.

These results confirm the linear decrease of the channel thickness. Its average value is of 1798.01 μm with a global variation of 12.81 μm and a 3.57 μm standard deviation. Despite the 24 μm difference with the configuration 1 average value, the global variation value is confirmed. Indeed, the device alignment induces a modification of the absolute thickness measurement while the relative variations show reproducibility. This latter is identified in a 2.5 μm interval, in concordance with the configuration 1 value.

4.4.4 Configuration 4: simultaneous transducers alignment compromise.

A fourth measurement series is realized on the same zone with a device positioning allowing a compromise between the alignment of both transducers. The results are presented on the figure 4.11.

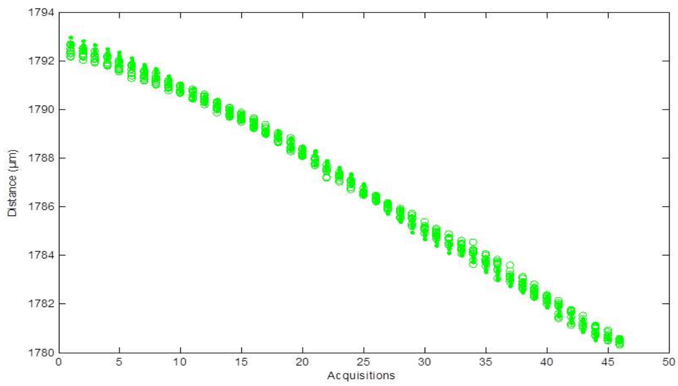

Figure 4.11: Configuration 4 measurement results.

These results confirm the linear decrease of the water channel thickness. The average value is equal to 1786.94 μm with a global variation of 12.6 μm and a standard deviation of 3.79 μm.

An average difference of 12 μm is identified with the measurement results of both the two previous sections. However, the previous global variation values are confirmed. This fact proves the device misalignment impact over the absolute values but also confirms the reproducibility of the relative variations. This reproducibility displays a local measurement dispersion of $\pm$ 500 nm.

This positioning configuration highly improves the local measurement precision. Consequently, an optimized positioning of both transducers during the experiments must be favored.

4.4.5 Configuration 5: Second measurements with simultaneous transducers alignment compromise.

In the framework of the reproducibility study, other measurement series were realized the following day. 4 ascending and descending movements were realized over a distance of 2 cm from the beginning of the previous zone. A comparison with the previous measurements along the 1^{st} centimeter, referred to as zone (a), and a study along the 2^{nd} centimeter, referred to as zone (b), are presented.

The device alignment configuration corresponds to the optimization of the configuration 3 and the measurement results are presented in figure 4.12.

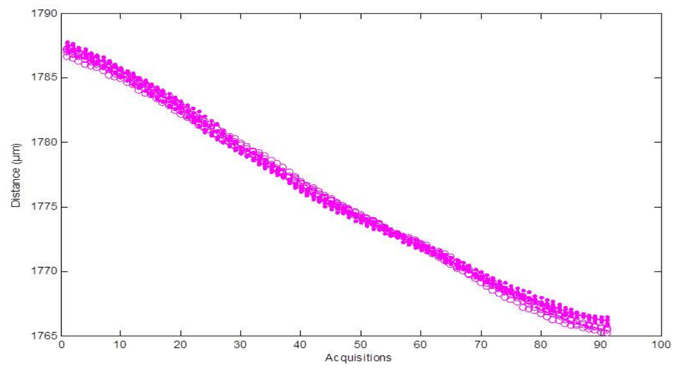

Figure 4.12: Configuration 5 measurement results.

Study of the zone (a)

First, the measurement results realized over the zone (a) are presented on the following figure 4.13.

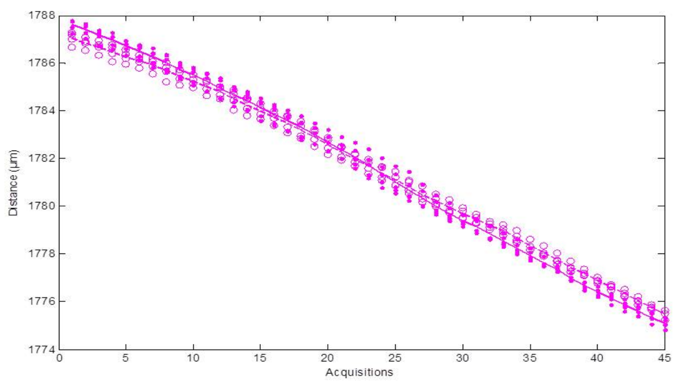

Figure 4.13: Configuration 5 measurement results over the zone (a).

These results confirm the linear decrease of the water channel thickness measurement. The average value is equal to 1781.57 μm with a standard deviation of 3.72 μm and a global variation of 12.44 μm . Even if a difference of 8.39 μm is identified with the average value of the previous configuration, the global variations are confirmed. This fact confirms the device misalignment impact over the absolute values but proves the reproducibility of the relative values. This reproducibility is identified in the interval of 1.3 μm.

Study of the zone (b)

The results of the measurement realized over zone (b) are presented on the following figure 4.14.

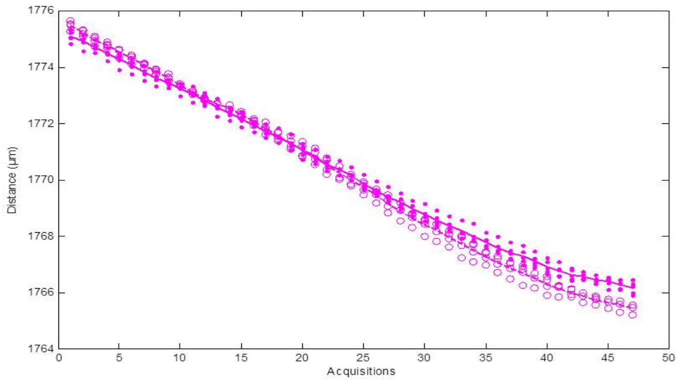

Figure 4.14: Configuration 5 measurement results over the zone (b).

The previous results of figure 4.14 demonstrate the continuous linear decrease of the water channel thickness previously observed. The average value of the thickness measurement over this zone is equal to 1770.05 μm with a standard deviation of 2.93 μm and a global variation of 9.68 μm over the zone (b). For each position, the measurements realized over the ascending and descending displacements are situated in an interval of 1.2 μm.

Consequently, first, the relative thickness estimations are highly reproducible and reliable in a maximum interval of 2 μm. Second, the linear decrease of the water channel thickness over all the measurement series and positioning configurations confirms the funnel form of the experimental sample. This non-parallelism is quantified to be at maximum equal to 20 μm along the studied 2 cm. This corresponds to a parallelism default of 0.1%, clearly demonstrating the high sensitivity of the proposed ultrasonic device.

4.4.6 Reproducibility measurements conclusion

An overview of all the previous measurement series results is displayed in figure 4.15.

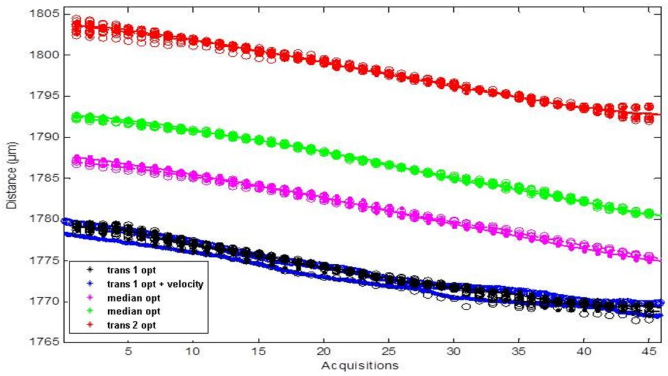

Figure 4.15: All positioning configurations measurement results.

To conclude:

- The ultrasonic device displacement parameters (velocity and direction) do not influence the thickness measurement,
- The absolute thickness measurements depend on the transducers alignment to the experimental sample,
- The accuracy of this measurement can be estimated to ± 20 μm
- In an optimized alignment of the transducers with respect to the sample faces, the relative variations of the thickness measurements are reproducible at ± 2 μm.

4.5 RHF model inter-plate distance reproducibility measurements

In order to investigate the ultrasonic device ability to measure inter-plate distances in the real experimental constraints, especially to quantify the plate curvature influence, a RHF model has been used in the laboratory. An image of this model is presented in figure 4.16.

4.5.1 Modeling of the device positioning in the RHF element

The RHF fuel element is constituted of involute shape plates positioned under involute of circle form. The inter-plate distance is fixed at 1.8 mm. In order to analyze

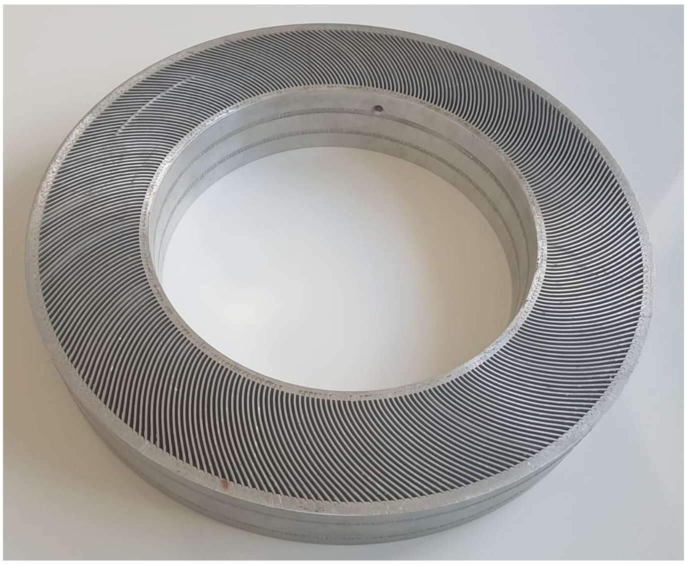

Figure 4.16: The RHF fuel element model.

the adequate positioning of the ultrasonic device in that specific form of the plates' interstice, it has been modeled.

A curve in an involute of circle shape is presented in the figure 4.17 (a). Then, the case of two parallel plates is considered. They are represented by the two red thin lines in figure 4.17 (b). Then, the ultrasonic device is assumed to be positionned on the centering bold red line of the figure 4.17 (b). Finally, the blue segments are the perpendicular segments of each point of the involute shape curve and are of 1.8 mm length. They represent the inter-plate distances to be measured.

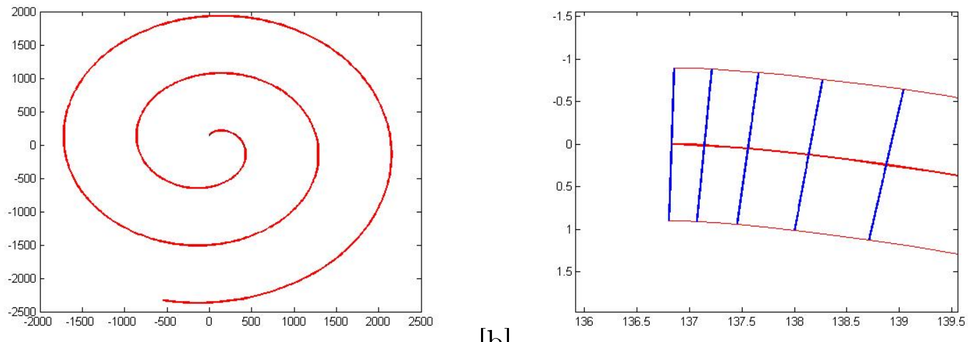

[a] [b]

Figure 4.17: (a) Developing circle form modeling (b) Two plates with 1.8 mm segments.

After the determination of the 1.8 mm segment emplacements along the involute shape curve, the next step is the identification of the ultrasonic device positioning that allows the adequate measurements. The corresponding device aligned positions with the plates are presented in figure 4.18 in black segments.

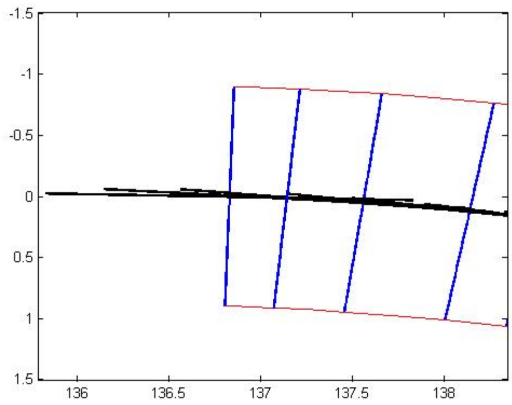

Figure 4.18: Ultrasonic device emplacements' modeling between two plates.

On figure 4.18, it can easily be observed that the adequate device positioning differs from a 1.8 mm segment emplacement to another. Indeed, the black segments are differently oriented. Consequently, the ultrasonic device alignment with the plates is highly sensitive and localized.

The convenient positioning of the device for the signal reception is clearly more challenging than that for the parallel faces samples. Indeed, the measurement bench employment is required to achieve the adequate positioning and optimize the signal reception.

4.5.2 RHF model experiments

During the experiments on the RHF model, the ultrasonic device is introduced between two plates. It is positioned with the measurement bench in order to optimize both transducers' signals. Two measurement series realized in two different water channels are presented in the following.

First experimental measurement series

In this first measurement series, 5 ascending and descending movements were realized inside an inter-plate interstice along a distance of 1 cm. The measurement results are presented in figure 4.19. The ascending measurements are presented in points while the descending ones are presented in circles.

The results of figure 4.19 display a variation of the water channel thickness over the

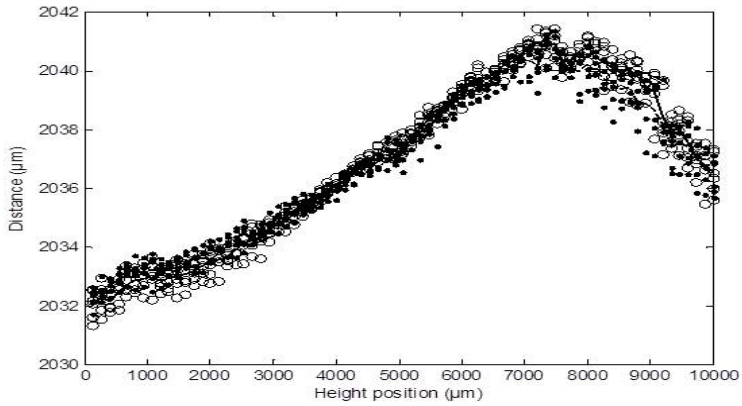

Figure 4.19: Results of a RHF model water channel thickness measurements.

analyzed 1 cm. This variation consists in a first increase, followed by a decrease. The measured average distance value is of 2036.84 μm, with a local standard deviation of 2.73 μm while the global variation is of 10.09 μm. The measurement reproducibility over the positions at the ascending and the descending displacements are in an interval of 2 μm.

Second experimental measurement series

In this second measurement series, 5 other ascending and descending movements were realized in a different water channel of the RHF element along a distance of 1 cm. The results are presented in figure 4.20 with the same legend than that of figure 4.19.

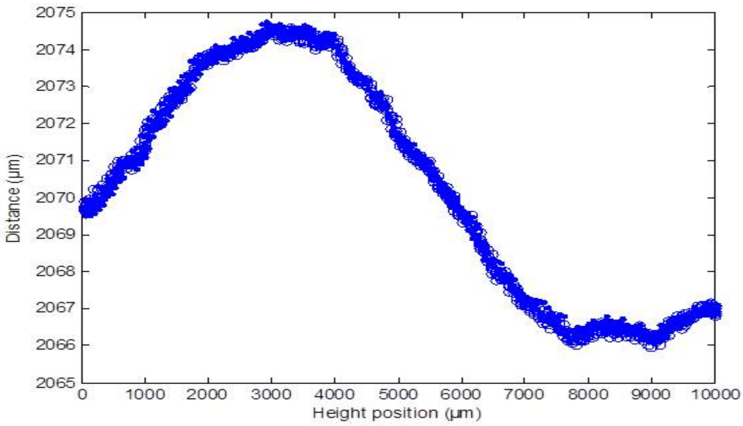

Figure 4.20: Results of a RHF model water channel thickness measurements.

The results of figure 4.20 display a variation of the water channel thickness over the analyzed 1 cm. This variation consists in a first distance increase smoothly followed by a decrease. The average distance value is of 2070.32 μm with a local standard deviation of 3.05 μm. The global variation is of 8.66 μm and the measurement reproducibility over the positions at the ascending and the descending displacements are situated in a maximum interval of 500 nm.

RHF model reproducibility conclusion

Thanks to the RHF fuel element model, the influence of the plate curvature on the inter-plate distance measurements was analyzed. The experiences allow the ultrasonic device response to the real experimental constraints. Both transducers' WP echo series reception necessitate an accurate device positioning. This allowed measurements with a relative distance resolution of 500 nm. Consequently, the ultrasonic device respects all experimental constraints and enables high accurate inter-plate distance measurements.

4.6 Conclusion

After the distance signal processing development, validation experiences were realized in the laboratory over three representative samples.

First, the identification of the distance measurement accuracy was performed due to a 50 μm steps manufactured in a titanium element. This experience allowed the estimation of the resolution to $\pm$ 1.5 μm during the device displacement. Second, distance reproducibility was studied with a plate silica element with an inter-faces distance of 1800 μm $\pm$ 10 μm, corresponding to that of the fuel plates' interstice. The device structure analysis allowed the estimation of the device transducers' parallelism to $\theta = 1\ ^{\circ}$. Then reproducibility measurements on this silica element allowed to visualize an interstice distance maximum variation of 20 μm over 2 cm, which corresponds to a parallelism default of 0.1%. Moreover, this experience enabled to identify the convenient device configuration for the most accurate relative distance resolution of $\pm$ 500 nm. Finally, measurements were realized in water channels of the RHF fuel element model to investigate the influence of the plate curvature constraint. This last experience demonstrates inter-plate distance measurements displaying thickness variations with a relative distance resolution of $\pm$ 250 nm.

The next fundamental step for inter-plate distance measurements consists in the identification of the radiation impact on the ultrasonic device components. In this view, a qualitative and quantitative experiment has been realized in a highly qualified organism. This experiment is described in the following chapter.

Chapter 5

Ultrasonic device resistance under irradiation

Contents

5.1 Introduction **94**
5.2 Arc-Nucléart irradiator **94**
5.2.1 General description of the installation 94
5.2.2 Radioactive sources of gamma irradiation 95
5.2.3 Irradiation cell 96
5.2.4 Dosimetry 97
5.3 Experimental constraints **98**
5.4 Experimental set-up **98**
5.4.1 Experimental set-up installation 98
5.4.2 Experimental Analyzes 102
5.5 Ultrasonic device analyzes **102**
5.5.1 Signal processing 102
5.5.2 Measurement results 103
5.6 Ultrasonic device passive components **112**
5.6.1 Visual inspection 113
5.6.2 Microscopic imaging 114
5.6.3 Mechanical properties assessment 115
5.7 Conclusion **116**

5.1 Introduction

In a way to complete the characterization of the ultrasonic device, it is necessary to evaluate its interaction with the environment it is exposed to. In the context of inter-fuel-plate distance evaluation, the ultrasonic device is subjected to high radiations. Consequently, the influence of this radiative environment on the characteristics of each ultrasonic device component must be identified.

To evaluate such important phenomenon, an experiment evaluating and quantifying the device resistance under irradiation is realized. In a view to observe the repeatability of the radiation impacts, six ultrasonic devices are mounted, leading to the irradiation of 12 ultrasonic transducers. They are exposed to a 3500 kGray irradiation during 4 months. Their initial characteristics are evaluated and compared to the post-irradiation modifications. A reference ultrasonic device, which is not exposed to radiation, is inserted in this experiment in order to take into account environmental phenomena.

In this chapter, the general installation and the irradiation concept of the Arc-Nucleart Institute is presented. Then, the whole aspects of the experiment are developed. After that, the experimental results are displayed and discussed, allowing the visualization and the interpretation of the ultrasonic device components' behavior under the irradiated environment.

5.2 Arc-Nucléart irradiator

5.2.1 General description of the installation

The Arc-Nucléart institute is a Public Interest Group supported by four partners: the CEA of Grenoble, the ministry of culture, the city of Grenoble and the ProNucléart association. Its main mission consists in the conservation and restoration of objects made of organic materials (wood, leather, fibers) by exposing them to gamma radiation. New methods are also under development for degraded materials in the Arc-Nucléart laboratory.

The Arc-Nucléart installation is mainly constituted of a pool irradiator [81]. It consists of a water pool where radioactive sources of Cobalt ^{60}Co are placed and generate intense beams of gamma radiation. The second installation element is an irradiation concrete cell related by an underground channel to the water pool. When the radiative sources are placed in the water pool, this latter allows gamma protection. They allow the irradiation of the contained samples. The source displacement between the water pool and the irradiation cell is controlled through a mobile cart. The scheme of the installation is illustrated on figure 5.1.

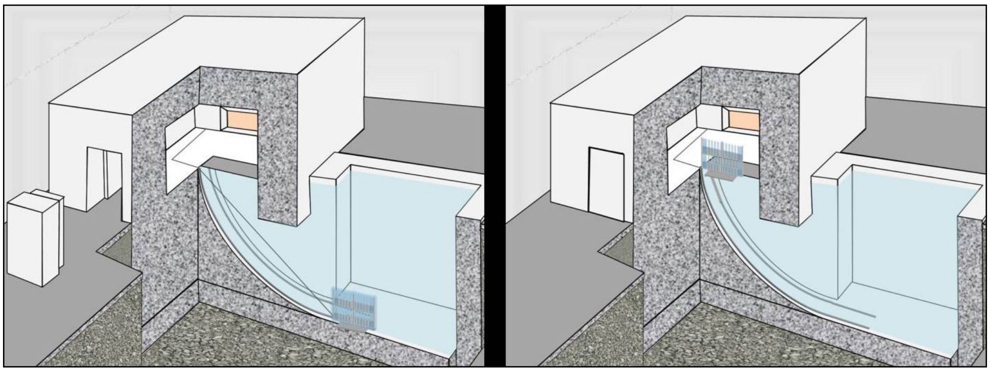

Figure 5.1: Nuclear irradiator installation scheme.

When the radiation sources are placed in the water pool, the irradiation cell is accessible through a concrete door. The irradiation sources, that are placed on a carrier-panel, are introduced in the irradiation cell when this door is completely locked. They consequently irradiate the cell and the objects it contains.

The Gray is the unit for the received irradiation dose of a material. One Gray corresponds to an energy absorption of 1 J per kg. The dose rates, proportional to irradiation intensity, are generally expressed in Gy/h in comparison to the international system unit (Gy/s). In the Arc-Nucleart installation, the dose rates are of the order of tens of Gy/h to 1 or 2 kGy/h.

The main characteristics of the Arc-Nucleart installation are:

- The principle activity authorized: 3700 TBq (terabecquerel) of ^{60}Co (100000 Ci), current activity from 1000 to 2500 TBq according to ^{60}Co decrease and sources' renewal,
- Pool depth: 4.25 m,
- Cell walls thickness: 1.50 m,
- Cell interior dimensions: 4.00 m*4.00 m with a height of 2.60 m (2.00 m useful under the overhead crane).

5.2.2 Radioactive sources of gamma irradiation

The Gamma irradiators, either for research or industrial applications, exclusively employ ^{60}Co sources. Indeed, these latters have many advantages:

- the emission of two gamma photons of 1.17 MeV and 1.33 MeV, particularly penetrating for each β disintegration,

- average convenient period of 5.27 years, allowing more than 20 years of exploitation and an easy managing of the recycling or the disposal after several tens of years of radiative decay,
- metalized stable and solid form.

This radio-element type is manufactured in nuclear reactors, by activation of the stable highly pure Cobalt. This activation principle by neutron integration and following disintegration is presented in figure 5.2.

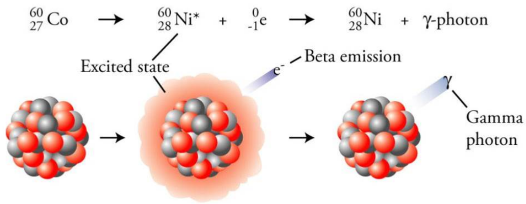

Figure 5.2: Cobalt disintegration principle.

The natural stable Cobalt has a nucleus constituted of 27 protons and 32 neutrons (59 nucleons). It is noted Cobalt 59 or ^{59}Co. If an isolated neutron goes next to the nucleus, this latter can catch it. It is then transformed in cobalt 60 noted ^{60}Co. The ^{59}Co is thus activated in ^{60}Co by neutron catching and ^{60}Co is an artificial radio-element.

To recover its stability, the ^{60}Co must transform one of its neutrons into a proton. It realizes that by β disintegration, corresponding to the emission of a high energy electron (negative charge) from the additional neutron. Simultaneously, two high energy photons are emitted (1.17 MeV and 1.33 MeV). It has thus been disintegrated into the stable nickel 60 (^{60}Ni), present in the nature. This transformation randomly occurs and a duration of more than 5 years is needed for the disintegration of half of the atoms of ^{60}Co. The half-life of the cobalt is estimated to 5.27 years.

To manufacture gamma sources, ^{60}Co samples are sealed in order to prevent from contamination risks. The radiative material, under a non-dispersible metallic form, is introduced in a double stainless steel envelope completely waterproof. However, these envelopes allow the Gamma irradiation (the Beta emission is totally stopped in the source and in the envelopes and consequently must not be considered).

5.2.3 Irradiation cell

To irradiate the cell, the sources are first disposed on the carrier-panel. This operation is realized in the pool using manipulating bars. The sources repartition is realized in a way to obtain the most homogeneous irradiation intensity all around the panel. This latter is divided into four elements with 13 emplacements, consequently leading to a total of 52 possible emplacements. After that, the whole carrier panel is introduced into the cell by a mobile cart, with two symmetric irradiation zones on each side of the panel as presented in figure 5.3.

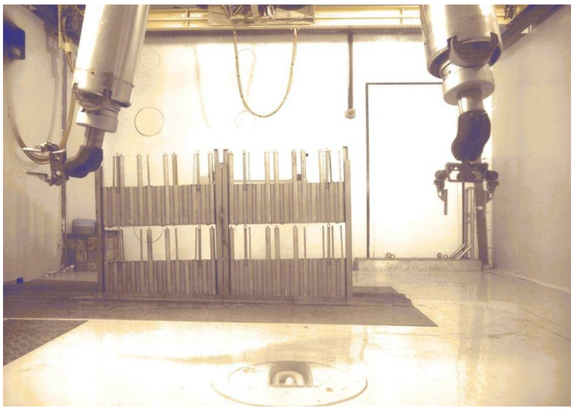

Figure 5.3: Carrier panel inserted in the irradiation cell [81].

To obtain the desired dose rate, it is possible either to control the carrier-panel composition or to define the adequate distance of the element from the sources emplacement. For the installation security, the elements are placed, at least, at 10 cm from the carrier-panel. The current rate dose is of the order of 2 kGy/h.

5.2.4 Dosimetry

The dose rates are measured thanks to optic dosimeters. Their principle relies on the optic density changes according to the dose. The dosimeters are of PMMA (poly-methylmethacrylate) type, namely the "Red Perspex" or "Amber Perspex" dosimeters from "HARWELL Dosimeters Ltd" [82]. An image of the "Red Perspex" dosimeter is presented in figure 5.4. These tinted plastic pieces with a volume of $30 * 11 * 3$ mm are individually conditioned in aluminum blisters of $65 * 50$ mm. A post-irradiated examination is realized by a spectrophotometer and a comparator for a precise measurement of the thickness in order to determine the optical density at a chosen wavelength to which the dose is associated via a calibration polynomial.

Figure 5.4: Red Perspex dosimeter

5.3 Experimental constraints

The study of the radiation impact on the ultrasonic device behavior needs to be performed for each component of the system. In this view, six ultrasonic devices were prepared, allowing the inspection of twelve ultrasonic transducers. For this purpose, one of the main parameters to be investigated is the resonance frequency. In this view, the transducers are realized with resonance frequencies dispersed over a band ranging from 38 MHz to 160 MHz.

According to the previous chapter, the adequate echo identification necessitates a coaxial cable length of 20 m linked to a second cable of 0.75 m which is introduced into the mechanical support. In a way to observe the radiation effect over the coaxial cables, two elements are submitted to the irradiation study: a first 20 m coaxial cable, and a second 20 m coaxial cable linked to the 0.75 m cable.

Each component of the ultrasonic device assembly needs also to be analyzed. For this purpose, several individual elements are realized and introduced in the irradiation cell.

The general environment conditions, such as temperature and humidity, can modify the transducers parameters. Consequently, two reference transducers are placed outside the irradiation cell and are considered as reference devices.

Knowing that the irradiation amount of 3500 kGray requires a period of more than three months, a continuous monitoring of the components' characteristics is necessary to link the observed modifications to the current irradiation amount. For these reasons, a specific experimental set-up is implemented to visualize in real-time the eventual modifications of the cables and transducers responses.

5.4 Experimental set-up

5.4.1 Experimental set-up installation

The experimental set-up is constituted of two separate parts illustrated schematically in the following figure 5.5. The first one consists in the elements to be irradiated which are placed inside the irradiation cell. The second part consists of several electronic components controlled by an acquisition and signal processing software, specifically designed for the experiment. Specific communication paths allow the passage of the cables to realize the continuous monitoring through the electronic set-up. Both parts are presented and illustrated in the following.

The first part consists of the ultrasonic devices, the cables and the separated ultrasonic device components to be irradiated. All these elements are disposed on an

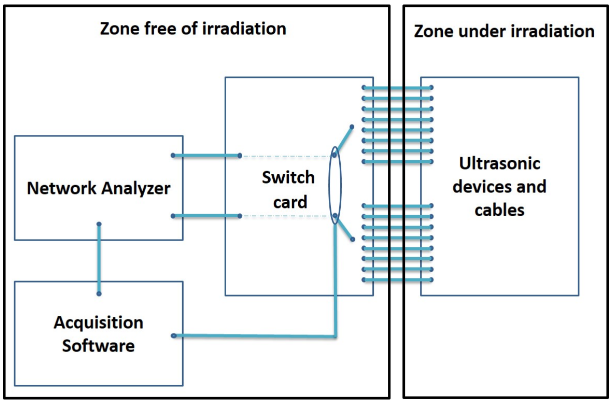

Figure 5.5: measurement system scheme.

aluminum support, which is placed next to the intended radiation sources entrance. The whole structure is displayed in figure 5.6.

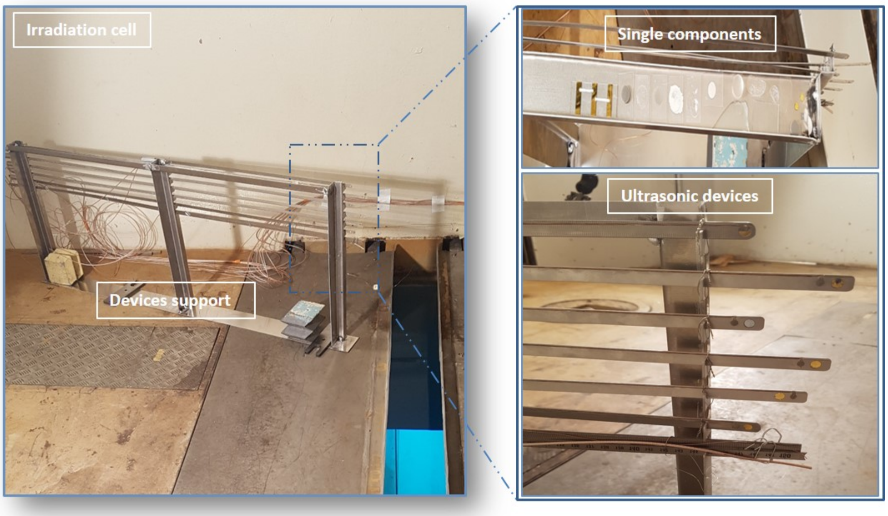

Figure 5.6: Ultrasonic devices and single elements in the irradiation cell.

The second experimental set-up part consists in the following:

1. Network analyzer: The network analyzer employed is the E8356A Agilent vector network analyzer. It provides fast scanning speed, wide dynamic range, low noise and flexible connectivity traces.

2. PXIe platform: The electronic acquisition system is integrated into a PXI platform. It uses PCI-based technology and adds a rugged CompactPCI mechanical form-factor to define hardware, electrical, software, power and cooling requirements. Then PXI adds integrated timing and synchronization. The components integrated in the chassis PXIe−1062 are:

- The PXIe−2747 switch card: It is a PXIe RF multiplexer switch module for switching RF signals in many applications. This card contains a dual 8 inputs and 2 outputs, allowing the devices monitoring.
- The PXIe−8135 controller constitutes the interface between the PXI platform components and the acquisition software.

3. Acquisition software: For the devices monitoring, the acquisition software is realized by allowing the scanning of all the transducers responses. Indeed, the program is realized according to the steps presented in the block diagram of figure 5.7. The program interface is also displayed in figure 5.8.

An image of the acquisition and monitoring system placed outside the irradiation cell is presented in figure 5.9.

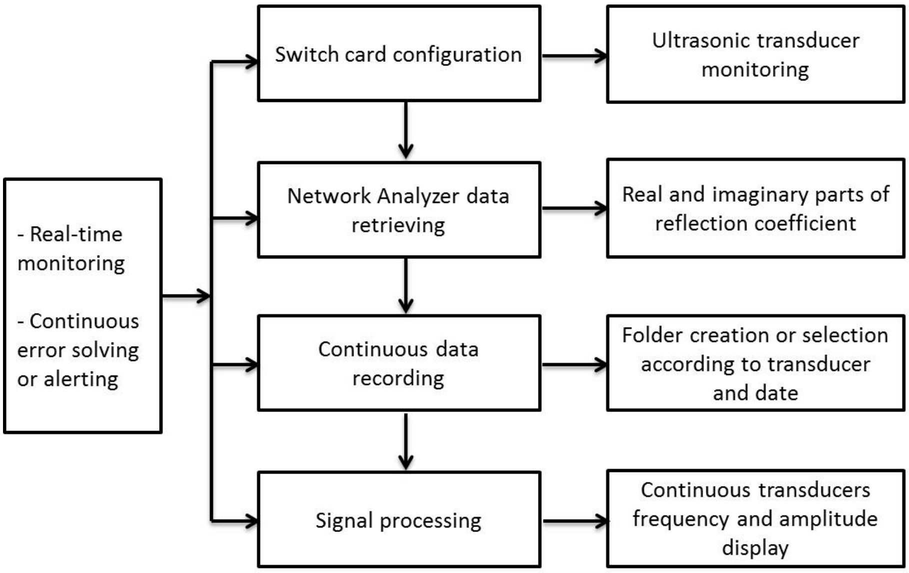

Figure 5.7: Acquisition software block diagram.

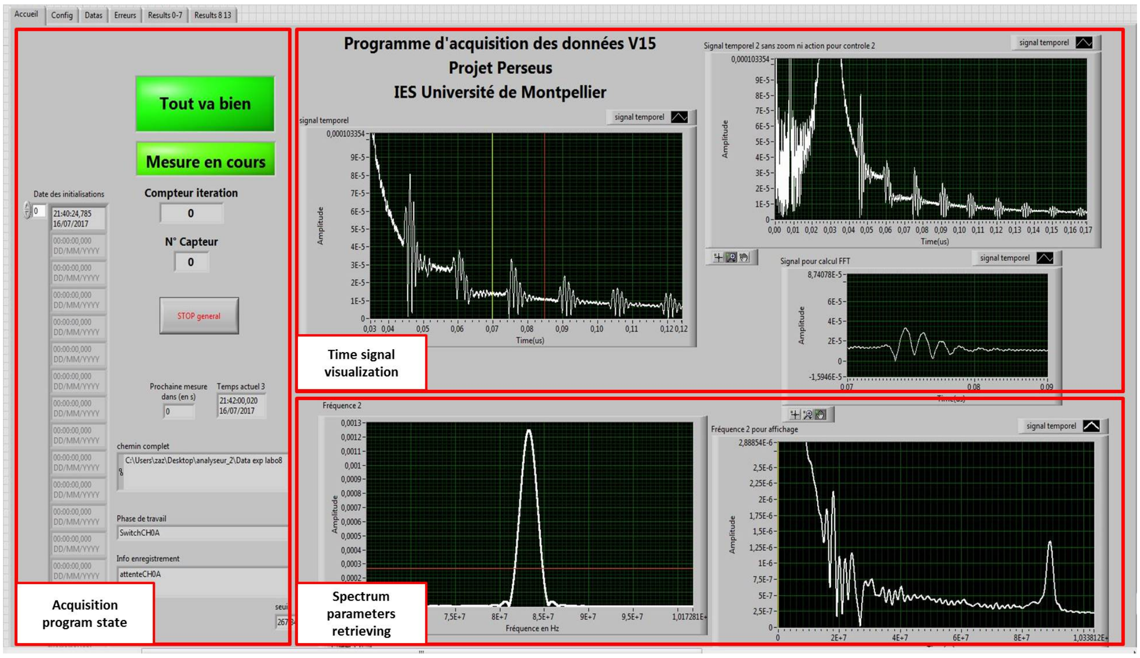

Figure 5.8: Acquisition program interface.

Figure 5.9: Acquisition and monitoring system placed outside the irradiation cell.

5.4.2 Experimental Analyzes

In a way to evaluate the irradiation influence, a comparison between each element characteristic before and after the irradiation experiment is necessary.

- For the mounted ultrasonic devices, the external electronic system allows the continuous and real-time evaluation of the transducers through a wifi network. The transducers responses are analyzed according to a specific signal processing detailed in the following section.
- For the ultrasonic device components, the analyzes to be realized consist mainly in the visualization of their forms, in their adhesion analysis and also in the measurement of their mechanical properties.

The analyzes and irradiation experiment results of both these element types are further exposed.

5.5 Ultrasonic device analyzes

5.5.1 Signal processing

In order to analyze the measurements realized through the previously described electronic installation, a specific signal processing has been developed. For all the elements, namely the irradiated transducers, an acquisition is realized each 6 minutes. It allows the retrieving of each spectrum. Indeed, the network analyzer allows the recording of both the real and imaginary parts, both employed to form the complex signal of the corresponding element.

For a specific monitoring of the acoustic echoes, the signal is subjected to an Inverse Fourier Transform in order to obtain the temporal signal. An adequate filtering is then applied according to the frequency bandwidth of each ultrasonic transducer. After that, a specific echo is extracted for its analysis all over the acquisitions. This echo parameters are then visualized and exploited to infer the ultrasonic transducers behavior along the irradiation experiment.

For the comparison of the ultrasonic devices' behavior before and after the irradiation experiment, the extracted echo parameters' evolution to be investigated concerns its frequency spectrum, namely the resonance frequency, the spectrum amplitude and the bandwidth. The experimental results are presented in the following section.

5.5.2 Measurement results

In order to organize the interpretation for each parameter, the reference ultrasonic transducers and the electrical cables results are first showed on a common figure, then those of the irradiated transducers are presented in following figures. The irradiated transducers are indexed from one to nine. For each parameter, a result interpretation is proposed.

Bandwidth spectra evolution

Reference transducers and electrical cables results

The reference transducers' and electrical cables' bandwidth spectra during three days at the laboratory are presented in figure 5.10 while those during the irradiation experiment are showed in figure 5.11.

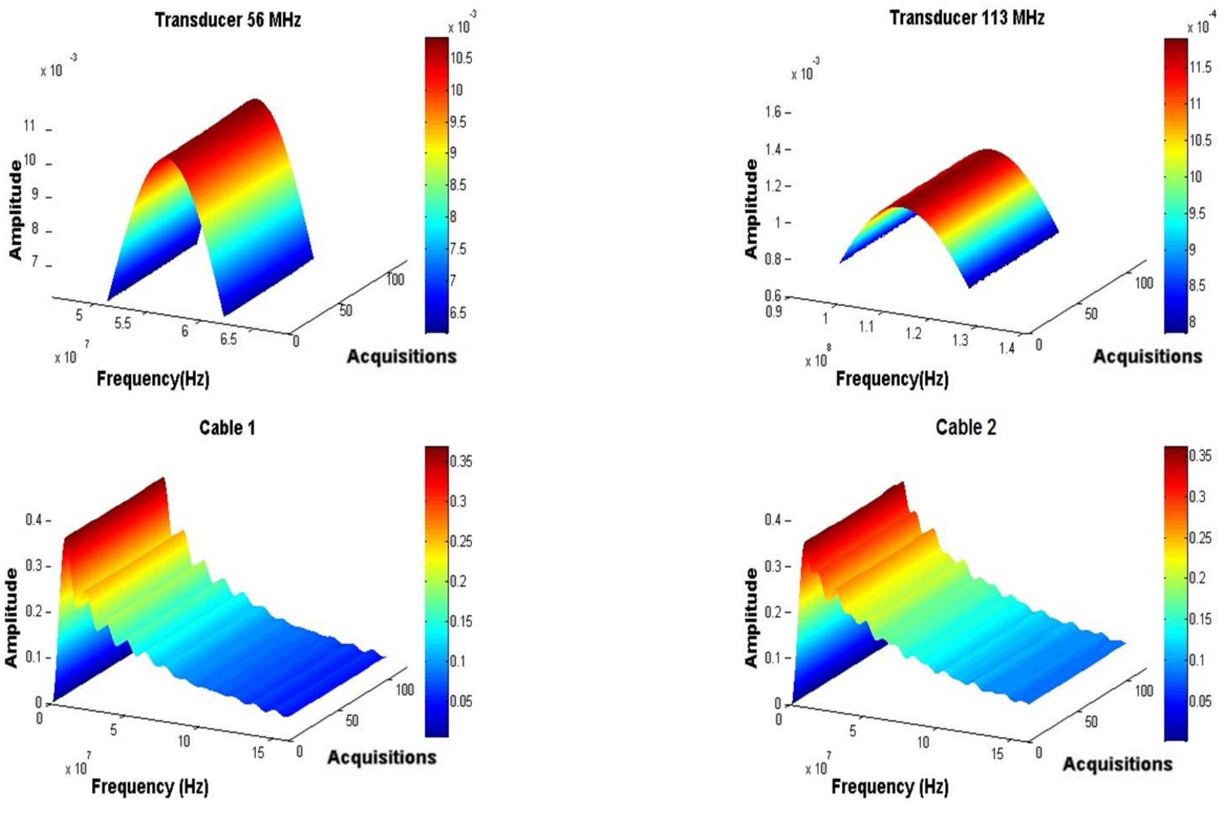

Figure 5.10: Reference transducers and cables spectra at the laboratory.

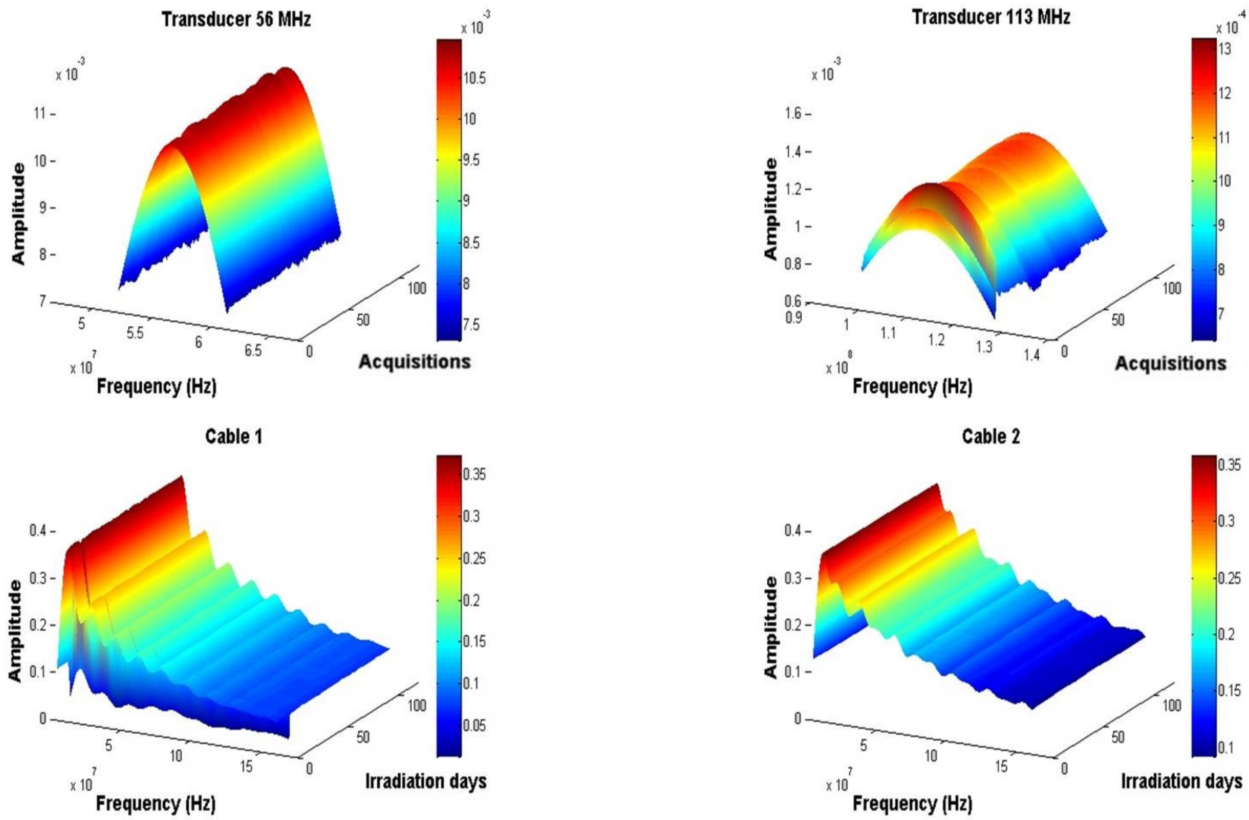

Figure 5.11: Reference transducers spectra outside the irradiation cell and irradiated cables spectra during irradiation experiment.

A general overview of the bandwidth spectra manifests a general stabilized behavior.

Along the irradiation experiment, the first reference non irradiated transducer, of a resonance frequency of 56 MHz, a smooth stable behavior of the bandwidth spectra is displayed. The second reference non irradiated transducer, of a resonance frequency of 113 MHz manifests also stable parameters values in an interval of 3 %.

For the irradiated cables, a stable behavior is retained. The 20 m cable, referred to as cable 1, except for a local amplitude variation of 3 %, manifests parameters stability. For the second cable of a 20 m cable related to the cable of 0.75 m, referred to as cable 2, the spectra stability is maintained in an interval of 1 %.

Irradiated ultrasonic transducers results

The bandwidth spectra of the irradiated ultrasonic transducers before irradiation are presented in figure 5.12 while those monitoring irradiation are displayed in figure 5.13.

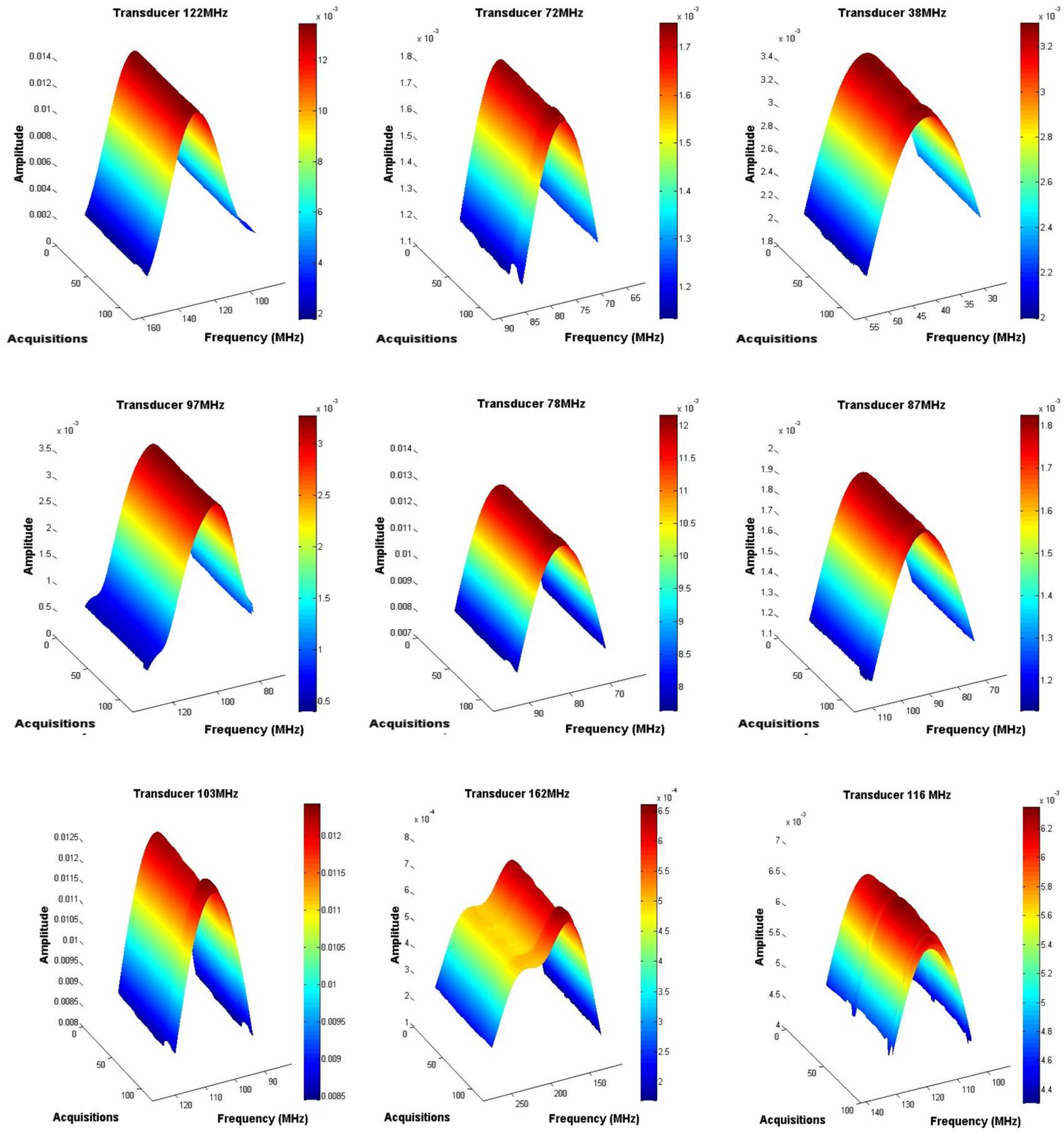

Figure 5.12: Ultrasonic transducers spectra before the irradiation experiment.

The figure 5.12 displays the transducers bandwidth spectra evolution during the three days in the laboratory conditions. Indeed, a high stabilized behavior of the transducers can be retained.

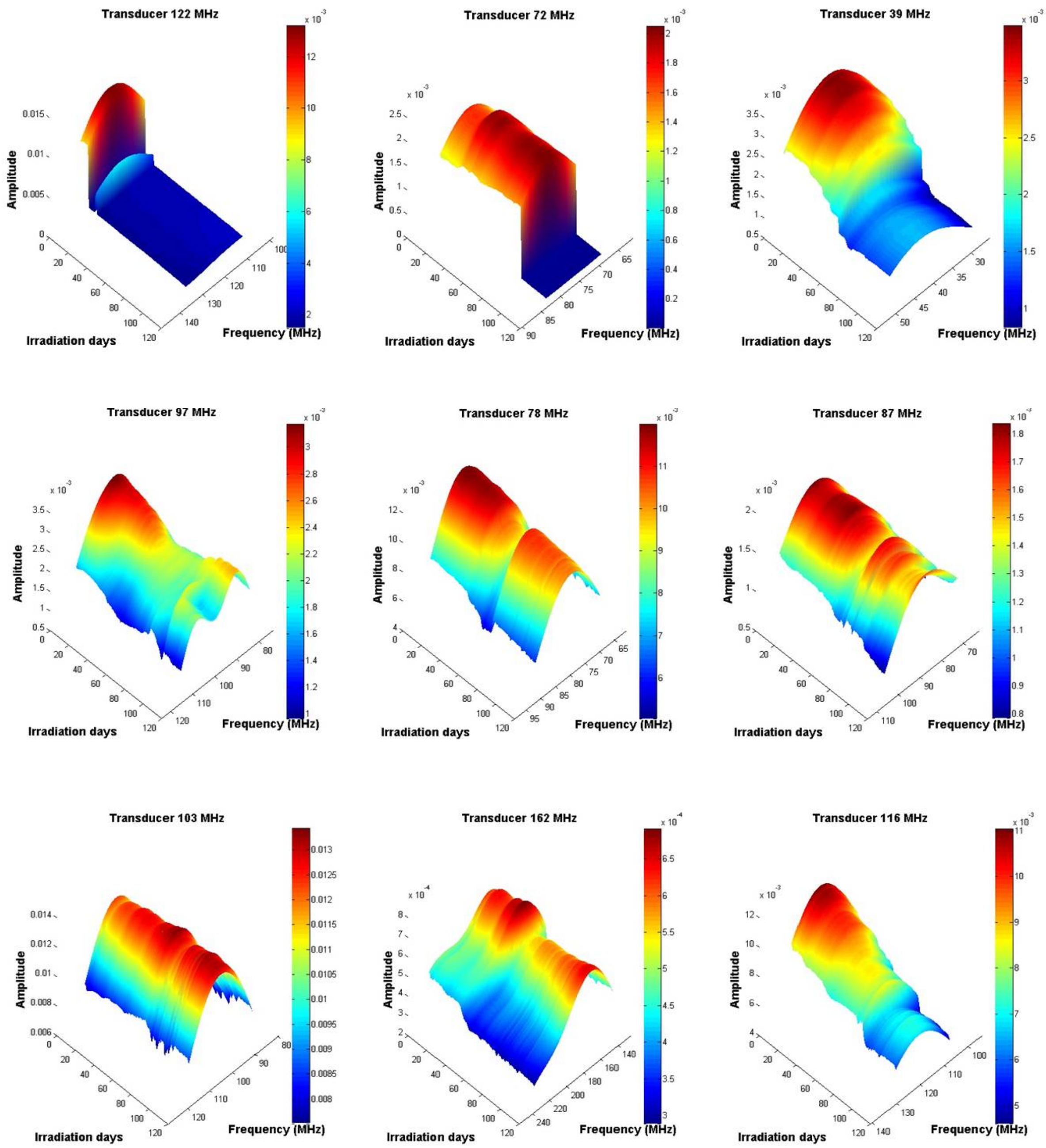

Figure 5.13: Ultrasonic transducers spectra all over the irradiation experiment days.

The bandwidth spectra evolutions allow an analysis of transducer behaviors. Indeed, it is observed that most transducers showed a small or no spectra evolution along irradiation. Only transducers 1 and 2 present significant modifications. They completely died away after several days of irradiation, leading thus to two groups: stable and unstable transducers. The cause of this defection is further investigated and explained.

Resonance frequency, spectrum amplitude and bandwidth variations

In the following figures, the red line corresponds to the frequency relative variation and the blue one is the amplitude evolution according to reference values, namely the laboratory values. Then, the green line displays bandwidth evolution in percentage.

Reference transducers and electrical cables results

Reference transducers' and cables' parameters are in figure 5.14. First line shows their laboratory evolution and that during experiment is showed in second one.

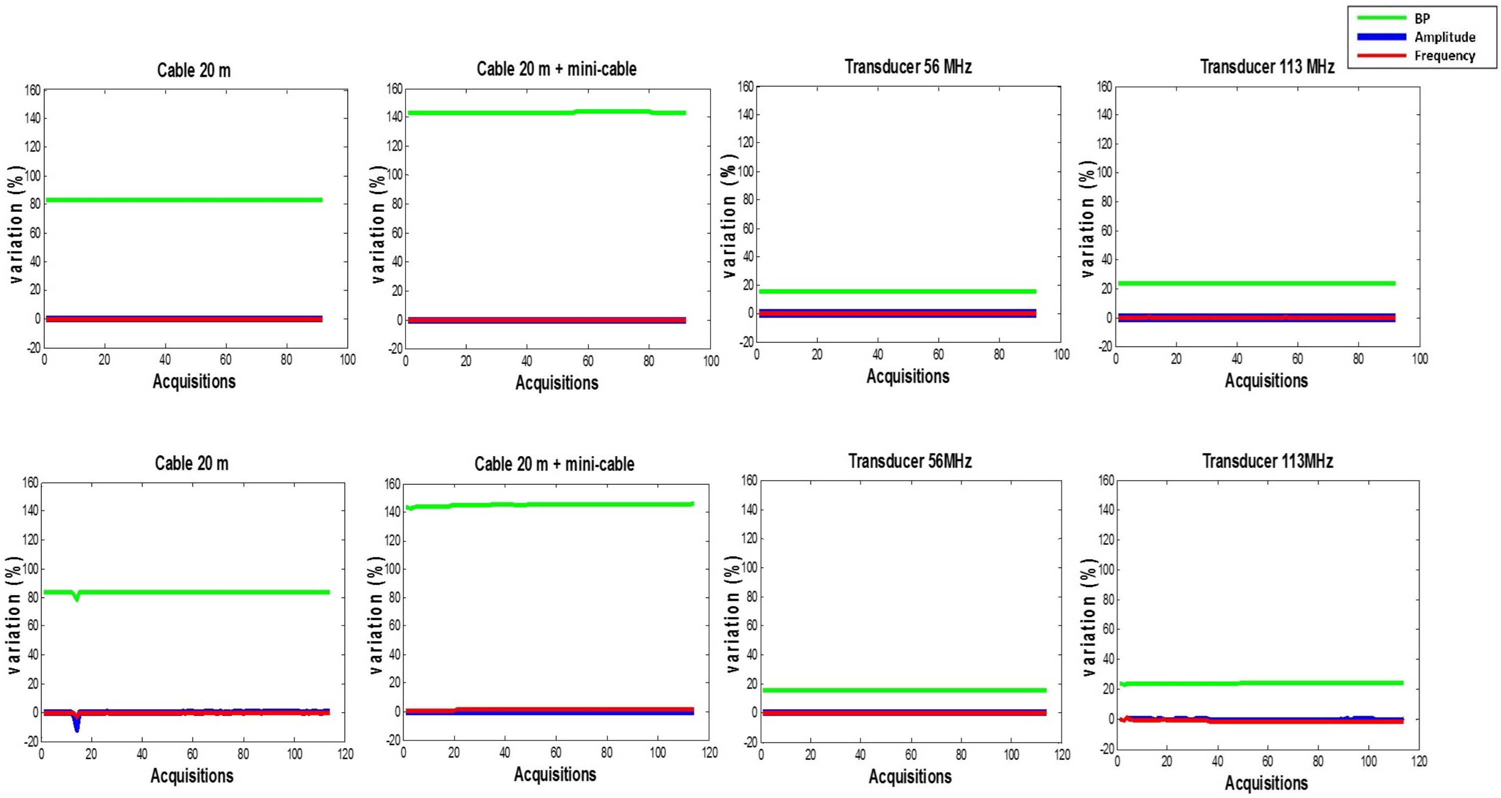

Figure 5.14: Relative frequency, amplitude and bandwidth variation of reference transducers and cables: first line graphs are at laboratory and second line graphs are outside irradiation cell for reference transducers while cables are irradiated.

Regarding the frequency:

- For reference transducers, the resonance frequencies are respectively of 56 MHz and 113 MHz. Relative frequency variation of the 1^{st} transducer is less than 0.15 %. For the 2^{nd} transducer, the maximum frequency variation is of 2 %. As a consequence, for both transducers, a high frequency stability is observed.

- For cable 1, frequency bandwidth reaches 500 MHz. Along irradiation, it is stable in an interval of 0.11 %, except for the 14^{th} day displaying a 3 % variation. No specific explanation can be found and the initial characteristic is then re-observed along the experiment. For cable 2, frequency bandwidth is also of 500 MHz. The frequency variation along the irradiation is very small, being less than 0.8 %. Consequently, a cables' frequency stability is observed.

According to the amplitude:

- For the 1^{st} transducer, the maximum amplitude variation does not exceed 0.3 % while for the 2^{nd} transducer, the maximum variation reaches 1 %. Consequently, for both transducers, a general amplitude stability is also observed.

- For cable 1, amplitude variation is less than 0.5 %, except for the 14^{th} day with a variation of 12 %. For cable 2, the amplitude variation is less than 0.06 %. Consequently, a stable behavior of the cables under irradiation is observed.

Regarding the bandwidth:

- For the 1^{st} transducer, the maximum bandwidth variation does not exceed 0.2 % of the 15.75 % initial value, while for the 2^{nd} transducer maximum variation merely attains 1.4 % of the 23.52 % first value. Indeed, a general stability is observed on bandwidth variations with a slight increasing trend.

- For cable 1, the bandwidth is stable in a 0.5 % interval of the first value of 83.7 %, except for the 14^{th} day with a variation of 5.9 %. Specific variations appear at the same days as for frequency and amplitude. For cable 2, the variation is maintained in a 3.5 % interval of the 143 % initial value. A bandwidth stability is deduced, confirming cables stable behavior under irradiation.

To sum up, the maximum parameters variations are displayed in the table 5.1.

Element	Max frequency variation	Max amplitude variation	Max bandwidth variation
Ref Transducer 56 MHz	0.15 %	3.00 %	0.2 %
Ref Transducer 113 MHz	2.00 %	1.00 %	1.4 %
Cable 1	3.00 %	12.0 %	5.9 %
Cable 2	0.80 %	0.06 %	3.5 %

Table 5.1: Parameters maximum variations of cables and reference transducers.

To conclude, the non-irradiated reference transducers manifested a stability of the analyzed parameters in environmental conditions, while for the irradiated electric cables no significant influence of irradiation was exhibited.

Irradiated transducers results

In following figures, red line is the relative frequency variation and blue one is relative amplitude evolution. Then, green line is bandwidth evolution in percentage.

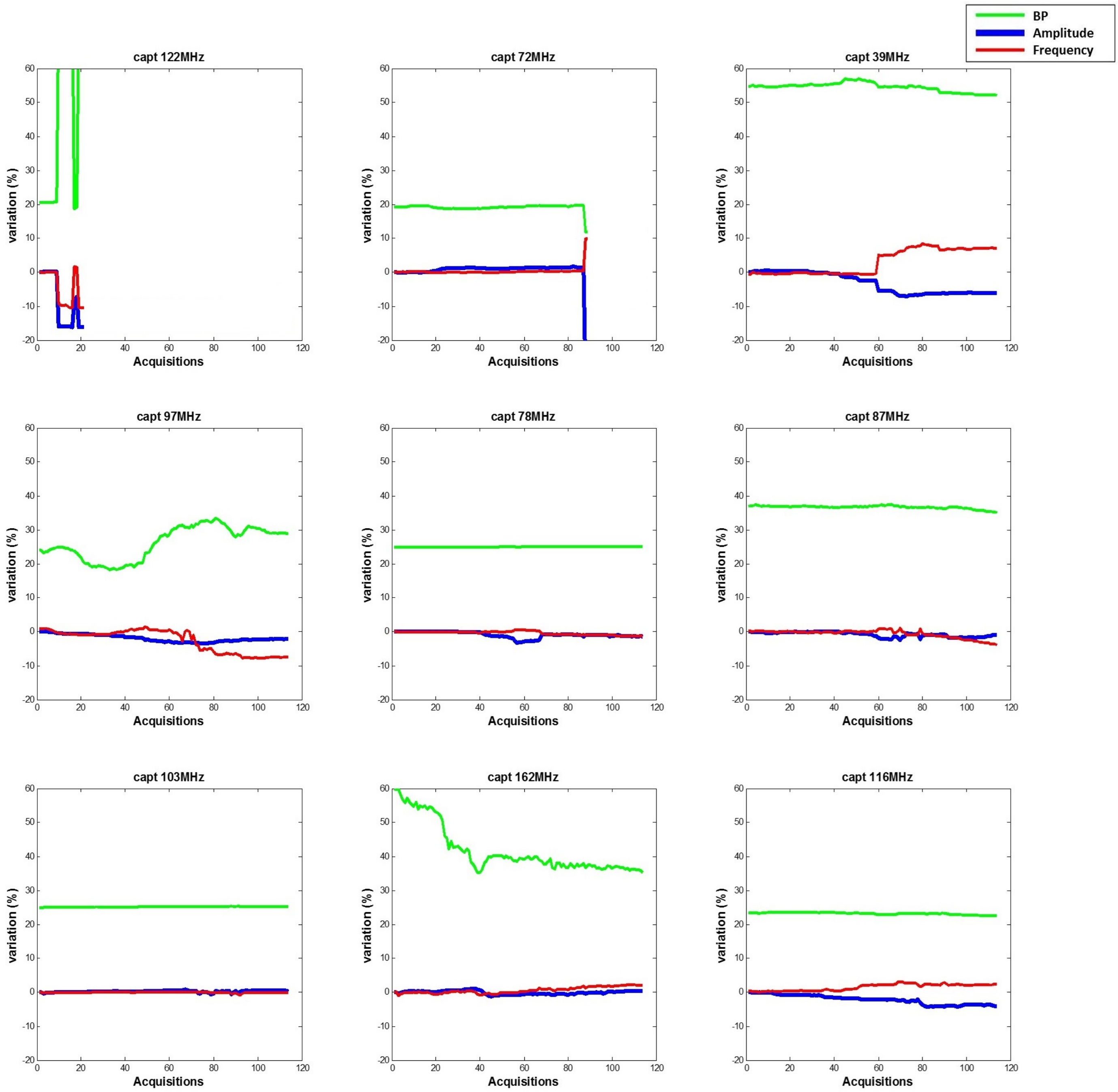

Figure 5.15: Relative frequency, amplitude and bandwidth variation of the transducers.

To summarize all the irradiated ultrasonic transducers' responses, the following table

5.2 includes their maximum variation parameter values.

Element	Max frequency variation	Max amplitude variation	Max bandwidth variation
Transducer 122 MHz	_	_	_
Transducer 72 MHz (until the 87^{th} day)	0.50 %	1.50 %	2.0 %
Transducer 39 MHz	8.00 %	5.00 %	5.0 %
Transducer 97 MHz	8.00 %	3.40 %	12 %
Transducer 78 MHz	1.50 %	3.20 %	0.4 %
Transducer 87 MHz	4.00 %	2.45 %	2.5 %
Transducer 103 MHz	1.00 %	1.00 %	0.7 %
Transducer 162 MHz	2.00 %	1.50 %	25 %
Transducer 116 MHz	3.00 %	4.50 %	1.0 %

Table 5.2: Parameters maximum variations of the experienced elements.

According to the previous table 5.2, two groups are observed in concordance with the bandwidth spectra analyzes. Each group will be separately discussed.

- Unstable transducers: This group is composed of transducers 1 and 2, manifesting a malfunction. Their parameters' variations are described hereafter.

For transducer 1, after 10 irradiation days, there are: a 10 % decrease of the center frequency value, a 16 % variation of the amplitude parameter and a 55 % variation with respect to the initial bandwidth value. Then, the 16^{th} day, for all the parameters, initial values were recovered for 2 days, before a lasting malfunction. This acoustic signal loss is probably due to a cable welding malfunction. This point and the following indicate that the welding of the cables may be weak points of the transducer structures while the piezoelectric elements are quite radiation resistant.

Transducer 2 maintained for 87 days its frequency in a range of 0.5 %, its amplitude in an interval of 1.5 % and its bandwidth parameter in a 2 % range around the initial value of 55 %. Then, a malfunction is observed similar to that of transducer 1 probably corresponding to welding failure. Indeed, for transducer 2, a 10 % frequency variation, a 42 % amplitude decrease and a 8 % bandwidth decrease appear.

To investigate the transducers 1 and 2 malfunctions, the time signal comparison before (in red) and during (in blue) the malfunctioning phenomenon is presented in figure 5.16.

In figure 5.16, the decrease in amplitude of the ultrasonic echoes can be observed while presenting a shift in their time position. This fact implies that the electric

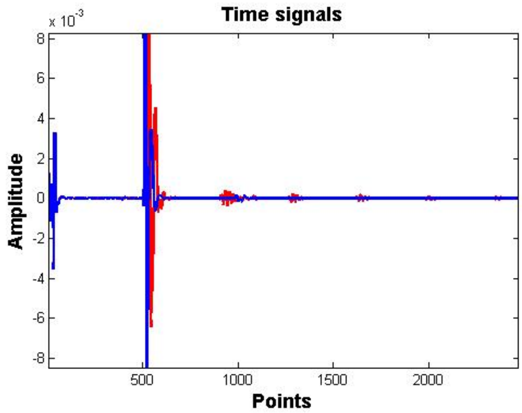

Figure 5.16: Time signal comparison between the functioning case (red) and the malfunctioning case (blue).

echoes are only received from the first cable of 20 m, confirming that the loss of the acoustic echoes is due to a damaging of the welding connecting the two cables. Assuming this fact, a new welding method has been employed for the device mounting and assures the cables' connection stability.

- Stable transducers: this group is composed of all the other irradiated ultrasonic transducers. Their parameters' variations are presented in the following.

Transducer 3 maintained its 38 MHz resonance frequency in a 0.8 % range until the 60^{th} day. A local increase of 6 % is observed and then gradually continues to 8 %. The amplitude decreases of 2.4 %, before decreasing to 5 % also at the 60^{th} day. The bandwidth first increases by 2 %, before decreasing of 3 % also after 60 days.

Transducer 4 manifests a stabilized frequency variation in a 2.5 % range until the 60^{th} day. A decrease is then observed until 6 % during 15 days. A gradual decrease finally follows until 8 %. For the amplitude, a continuous decrease is observed with a maximum percentage of 3.4 %. Finally, the bandwidth manifested a stabilized behavior in a 5 % range over the 24 % initial value for 40 days. It was followed by a gradual 12 % increase.

For transducer 5, the frequency variation along the experiment does not exceed 1.5 %. The maximum local variation is of 0.77 % observed at the 57^{th} day. For amplitude, the general variation percentage does not exceed 3.2 %. This maximum variation is also observed at the 57^{th} day. The bandwidth general variation does not exceed 0.4 % of the initial value of 25 %.

For transducer 6, the maximum frequency variation is of 4 %. Moreover, the maximum amplitude variation is of 2.45 %. Finally, the bandwidth variations do not exceed 2.5 % of the first value of 37 % in a global slight decreasing trend. Consequently, for all parameters, the transducers 5 and 6 manifested similar stable behaviors while being inversely placed in the same device. This indicates that the side emplacement of the transducers does not modify the irradiation impact.

Transducer 7 frequency variation does not exceed 1 % of the initial value. Then, the maximum amplitude variation is limited at 1 %. Finally, the maximum bandwidth variation is of 0.7 % over the 24.84 % initial value.

Transducer 8 maximum variations are of: 2 % for the frequency, 1.5 % for the amplitude and 25 % for the bandwidth. The most observable variation occurred after 40 days simultaneously for all the parameters through: a barely 1 % decrease for the frequency, a 2.5 % decrease for the amplitude and a 25 % for the bandwidth. After that, a general stabilization is observed.

For transducer 9, the frequency variation reaches 3 %. It consists of a global increase, with a slight improvement between the days 40 and 80. For the amplitude, a general decrease trend is apparent, reaching 2.5 %. In addition, a 4.5 % variation is noticed over the 80^{th} day, followed by a stabilized variation zone in a 0.8 % range. For the bandwidth, a slight decrease trend of 1 % of the initial value of 23.33 % is observed.

- Conclusion: According to the result analyzes, it can be observed that:

1. The electrical cables manifested a high parameters resistance,
2. For the malfunctioning transducers, the welding element has been identified as a potential source of failure,
3. For other transducers, the maximum variations were: 8 % for frequency, 5 % for amplitude and 25 % for bandwidth,
4. A high parameters' stability of the irradiated transducers is retained.

Consequently, except for the two first transducers' malfunction due to the welding failure, it can mainly be inferred a high resistance of the elements to radiations. This leads to stable responses of the devices validating the ultrasonic measurements of the temperature and water-channel thickness proposed in the previous chapters.

After the validation of the digital parameters stability under irradiation, the next step consists in the analysis of the material components of the ultrasonic devices.

5.6 Ultrasonic device passive components

To evaluate the irradiation impact on each device component, several elements have been realized and irradiated: the silica support, the adhesive material, the backing insulator material and the conducting material. The investigated characteristics are: the global form, the adhesion and the mechanical property modifications.

For the form and adhesion investigation, 4 elements were realized and will be referred to in the following as the multilayered structure group. The adhesive, the backing and the conducting materials are separately deposited on 3 silica supports and a second circular silica support is superposed. The 4^{th} element is a conducting material deposited without the superposed silica. This multilayered structure group comparison before and after the irradiation experiment is carried out through visual inspection and microscopic imaging.

For the mechanical property investigation, 4 elements are analyzed and will be referred to as the unilayered structure group. They consist in 2 types of silica, a backing insulator and a conducting material deposited on the silica. For the mechanical properties estimation of the unilayered structure group, acoustic signatures are realized. They allow the estimation of the Rayleigh velocity and the Young modulus values.

5.6.1 Visual inspection

The multilayered structure group images are presented on the first line of figure 5.17 (a), (b), (c) and (d). Their images after irradiation are displayed on the second line.

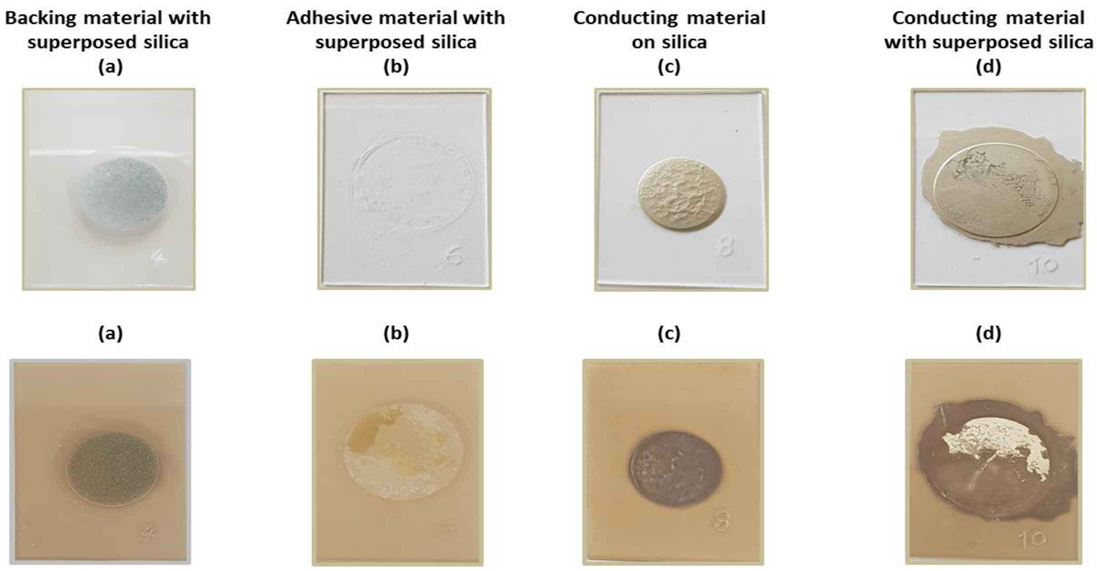

Figure 5.17: multilayered structure group images before and after the irradiation.

A first overview of the multilayered structure group shows that their general forms are maintained. For the silica supports of all the elements, a color modification is observed. This modification is due to the silica composition and mainly comes from microscopic impurities. For the elements (c) and (d), a color modification is also visible of the conducting material. This color modification does not appear in the conducting material layer inserted between the two silica parts of the element 5.17 (d).

To conclude over this analysis, the adhesion and forms are maintained after the irradiation experiment. For a specific analysis of the microscopic form modifications, the second comparison is realized thanks to the microscopic imaging.

5.6.2 Microscopic imaging

In order to investigate microscopic modifications, the industrial microscope TePla [83], available in the laboratory, is employed, using a 200 MHz ultrasonic transducer in order to acquire high resoluted images. This imaging is performed before irradiation, seen in figure 5.18 and compared to the ones realized after the irradiation exposed in figure 5.19.

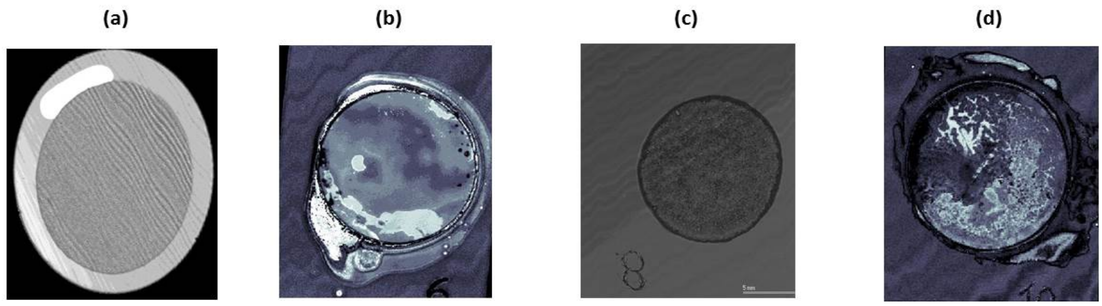

Figure 5.18: multilayered structure group microscopic images before irradiation.

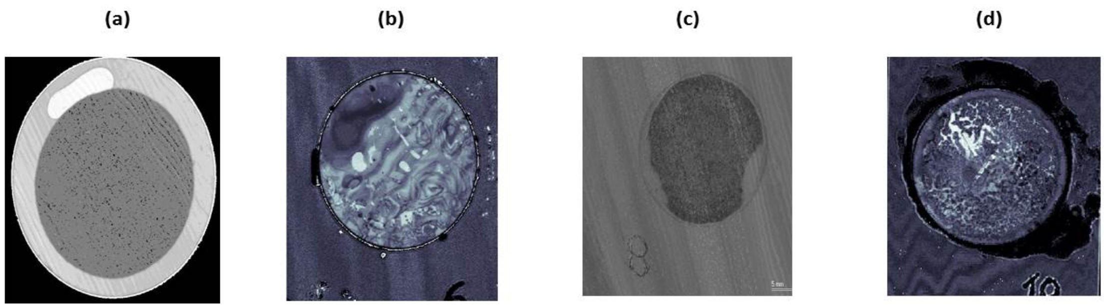

Figure 5.19: multilayered structure group microscopic images after irradiation.

Thanks to the microscopic images, the general stability previously observed is confirmed. Besides, the following remarks can be made:

- For the 1^{st} element, the comparison of images before and after irradiation implies that no significant modification can be observed.

- For the 2^{nd} element, the adhesive material observed on the contour area of the superposed silica of figure 5.18 (b) has been disbonded in figure 5.19 (b). Moreover, some new microscopic forms appear in the interstice zone.

- For the 3^{rd} element, the disbonding phenomenon is also visible over the conducting material boundaries displayed in figure 5.19 (c).

- For the 4^{th} element, the conducting element around the second silica manifests a color modification implying a signal attenuation due to the conducting element composition modification.

5.6.3 Mechanical properties assessment

For the mechanical property estimation, a focused ultrasonic transducer is used for surface acoustic wave generation [84]. The Rayleigh wave is generated inside the material by fixing the incidence of an acoustic external plane wave to a specific angle, the Rayleigh angle θ_R. During its propagation along the surface of the material, the Rayleigh wave radiates, at the same angle, energy into the coupling medium. The ray theory indicates that two main paths are available for the reflected acoustical waves. They correspond to two waves, the specular (figure 5.20(I)) and the Rayleigh (figure 5.20(II)) waves that will then recombine on the transducer surface.

By defocusing the transducer towards the sample surface along the Z axis, which means reducing the transducer-sample separating distance, ultrasonic wave interference occurs [84]. The received signal is then function of the z-evolution of the transducer amplitude and is called the acoustic signature V(z) [85]. An example of the received acoustic signature form is displayed on the figure 5.20 (b).

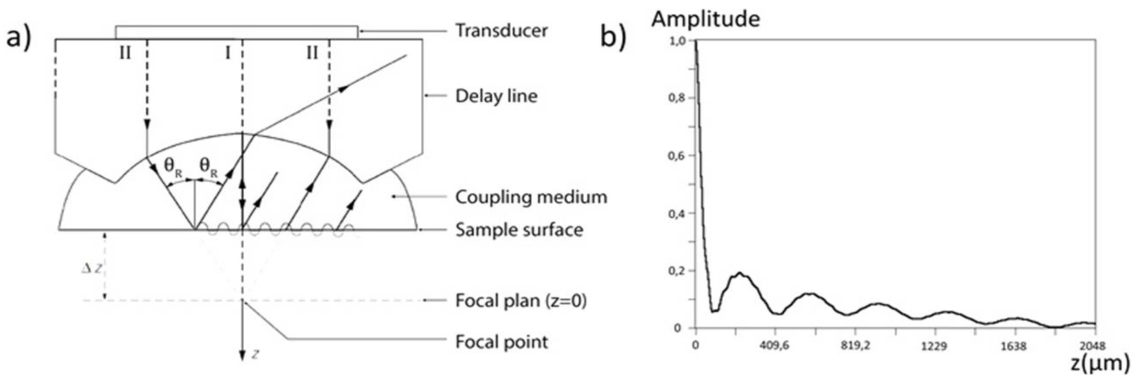

Figure 5.20: Acoustic signature process.

From the measurement of the pseudo-periodicity Δz, V_R is calculated under the following equation 5.1:

$$V_R = \frac{V_{fluid}}{\sqrt{1 - (1 - \frac{V_{fluid}}{2 * f * \Delta z})^2}} \tag{5.1}$$

where V_{fluid} is the coupling ultrasonic velocity and f is the transducer frequency.

The acoustic signature allows the measurement of the Rayleigh velocity. This latter is directly related to the material young modulus according to the article [86] through the following equation 5.2:

$$E = 3.00 * \rho * V_R^2. \tag{5.2}$$

This method has been used with a focused 140 MHz frequency transducer on the unilayered structure group. The measurement results of the Rayleigh velocity and the young modulus are presented in table 5.3.

Element	Pre-irradiation properties	Post-irradiation properties	Percentage variation
Silica type 1	$V_R = 3395$ m/s E = 71.86 GPa	$V_R = 3338$ m/s E = 71.13 GPa	1 %
Silica type 2	$V_R = 3110$ m/s E = 62.38 GPa	$V_R = 3108$ m/s E = 62.30 GPa	0.1 %
Backing material	$V_R = 4553$ m/s	$V_R = 4359$ m/s	5 %
Conducting material	$V_R = 5265$ m/s	$V_R = 5089$ m/s	3 %

Table 5.3: Rayleigh velocity and young modulus values of the analyzed elements.

From the previous table, the Rayleigh velocities and the young moduli of the unilayered structure group elements have presented a high stability under the irradiation experiment. This stability is maintained in a maximum interval of 5 %.

5.7 Conclusion

A reproducibility radiation experiment has been realized over 12 ultrasonic transducers and several samples of the ultrasonic components assembly materials. A distant and real-time monitoring and acquisition system has been controlling this experiment in a way to specifically evaluate the radiation influence. This latter has been of a 3500 kGy dose lasting for more than three months.

For the irradiated ultrasonic transducers, the parameters to be evaluated were the resonance frequency, the spectrum amplitude and the spectrum bandwidth, as the essential characteristics influencing the inter-plate distance measurement. Two ultrasonic transducers manifested an acoustical signal loss due to a welding malfunction. This latter is identified as an important element to improve and verify at each device assembly. All other transducers displayed a high stability of the investigated parameters along irradiation.

Concerning the passive material samples, the evaluated factors were the form, adhesion and mechanical properties modifications. These parameters were observed thanks to visual inspections, microscopic imaging and acoustical signatures acquisitions. Several comparisons before and after the irradiation experiment allow the identification of a high resistivity of the three investigated aspects.

Thanks to this radiation experiment, corresponding to a 10 hour duration contact to the fuel element through the 3500 kGy irradiation dose, all the ultrasonic device components ensured a significant stability. The in-situ application of this method will be presented in the following chapter.

Chapter 6

High Flux Reactor experiments

Contents

6.1 Introduction 120

6.2 Distance measurement 120

6.2.1 Measurement results 120

6.3 RHF fuel element experiment 121

6.3.1 Experimental set-up 121

6.3.2 Experimental protocol and proof-of-concept 122

6.4 Results and interpretation 130

6.5 Conclusion 133

6.1 Introduction

In the previous chapters, a new ultrasonic device was developed according to experimental constraints. The signal processing was optimized and allowed highly accurate results in laboratory measurements. In addition to this, the device components presented high stability during an irradiation experiment.

In this chapter, the ultrasonic device is tested in the High Flux Reactor fuel element for inter-plate distance estimation. The measurement results are displayed in the following.

6.2 Distance measurement

In chapter 3, the signal processing has been optimized in a way to reduce the dispersion on the water-channel thickness estimation. It is here applied to the signals acquired in-situ in the RHF reactor during the first PhD of the PERSEUS project.

6.2.1 Measurement results

During the previous thesis, an experiment was realized in the RHF fuel element allowing signal acquisition in a water channel with a manual ascending movement of the device. These signals are here reconsidered and their energy is computed thanks to equation 3.4 and is presented in figure 6.1 (a).

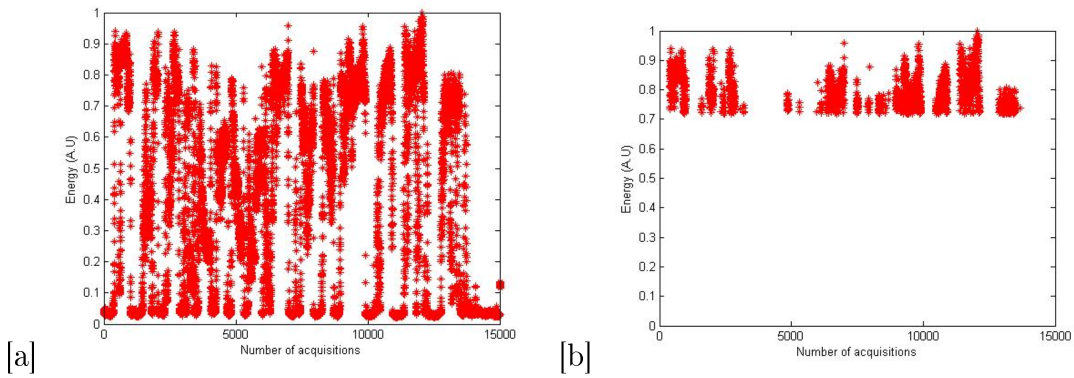

Figure 6.1: (a) Experimental signal energy measurements; (b) Selected signals for distance measurements.

This computation clearly demonstrates the impact of the orientation of the device with respect to the fuel plates. To select the most energetic signals, a threshold is proposed. This leads to selected positions with the corresponding energy presented in figure 6.1 (b).

After the signal selection, the new signal processing presented in chapter 3 is applied. In figure 6.2, a comparison between measurements realized with the previous and the new signal processing steps is presented.

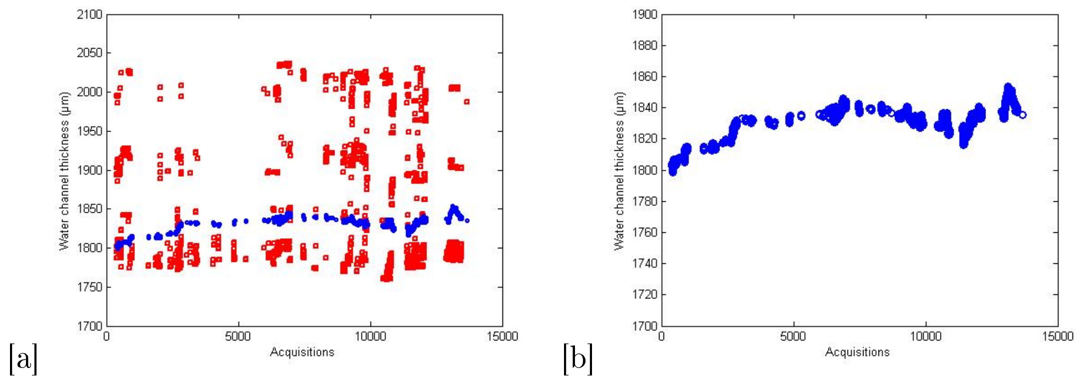

Figure 6.2: (a) Previous and new signal processing comparison; (b)New signal processing distance measurements.

In figure 6.2 (a), the comparison of the signal processing methods clearly displays the fact that the new signal processing is highly improving the inter-plate distance measurements by removing spurious values. They are mainly due to the low energy signals and the manual positioning. This latter implies a lack of the device vertical position identification.

The measurement results mainly allow the evaluation of an average inter-plate distance estimated at 1829 μm with a standard deviation of 11 μm. In addition, the device resolution is deduced through the dispersion of neighboring measurements performed at very close locations. It is here estimated to 2 μm.

6.3 RHF fuel element experiment

6.3.1 Experimental set-up

After the laboratory characterization and the validation of the new high frequency ultrasonic device prototype and signal processing, an in-situ experiment was realized in the RHF fuel element as follows: the ultrasonic device was fixed to a 4 m support handled by an operator positioned above the reactor water pool. The device support was related to the cable of the position monitoring device presented in chapter 2. This latter was placed above the operator emplacement.

In order to observe and monitor the blade introduction between the fuel plates, a waterproof and radiation resistant camera was installed above the fuel element. Images of the reactor experiment are displayed in figure 6.3.

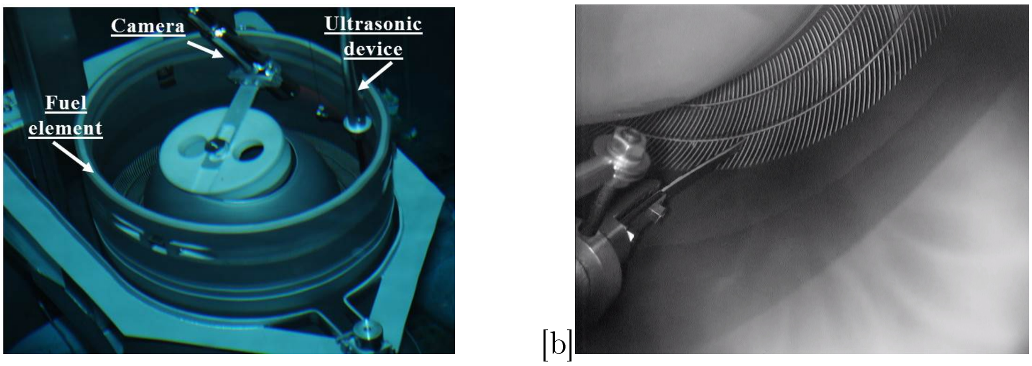

[a] [b]

Figure 6.3: New ultrasonic device in the RHF experiment [13] (a) inserted in the fuel element; (b) introduced between fuel plates.

The implemented experimental protocol allows the estimation of the water channel temperature and the inter-plate distance along the vertical blade position. This latter is recorded by the position monitoring device.

6.3.2 Experimental protocol and proof-of-concept

For the inter-plate distance evaluation, two parameters are evaluated by means of the ultrasonic device: the ultrasound velocity and the time of flight. For the RHF fuel element experiment, the investigation of each parameter is hereafter presented.

Transducers' calibration: experimental curves

As previously seen, the water channel temperature constitutes a parameter impacting the ultrasound velocity. This parameter is then analyzed through the measurement of the resonance frequencies of the transducers.

The test of the ultrasonic transducers after their conception allows the identification of their central frequency. The first transducer of the device has a central frequency of 103 MHz while the second transducer displays a central frequency of 85 MHz. In the following, the 103 MHz transducer is referred to as transducer 1 and the 85 MHz transducer as transducer 2. Figures 6.4 (a) and (b) display both simulated and experimental values of the frequency variation as a function of the temperature.

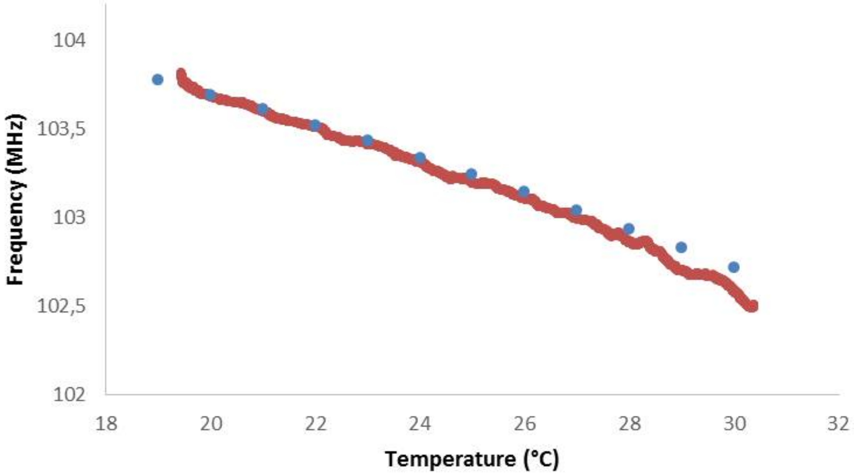

[a]

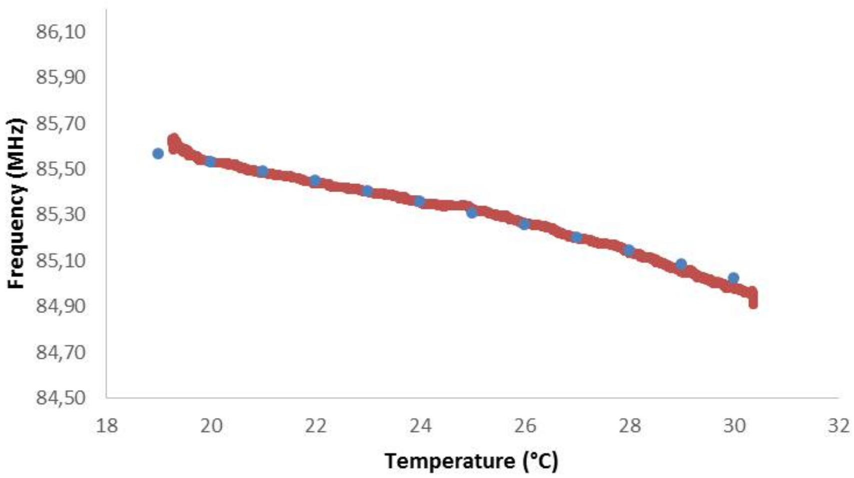

[b]

Figure 6.4: Frequency variation according to the temperature. Blue squares correspond to the simulated values and red points to the experimental data; (a) transducer 1; (b) transducer 2.

These curves will be used as references for the identification of temperature variation. Then, the ultrasonic velocity estimation in the water channel at the exact points of the inter-plate distance estimation is computed. The analysis of the experiments realized for the temperature variation will be presented below.

Reactor water pool temperature

The reflections forming the SW series are presented in figures 6.5 (a) and (b). One of the reflected echoes is selected and processed (vertical lines in figures 6.5 (a) and (b)). The frequency corresponding to the maximum energy of the transducer bandwidth (figures 6.5 (c) and (d)) is then retained and compared to data from figures 6.4 (a) and (b) to estimate the medium temperature.

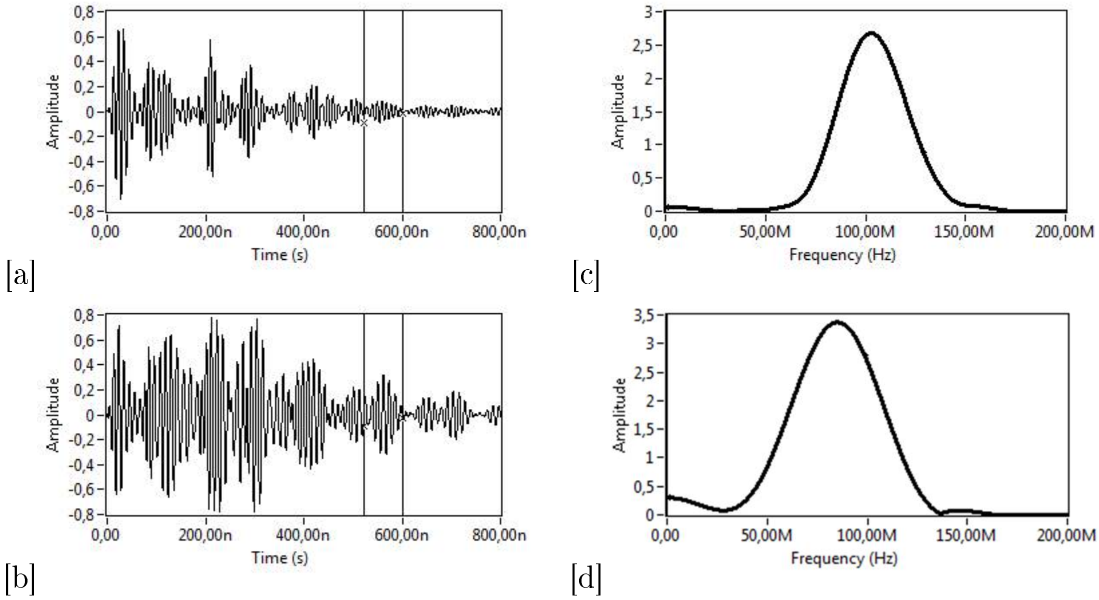

Figure 6.5: (a) and (b) Both transducers' received ultrasonic signals in the medium; (c) and (d) Both transducers' frequency spectra of the selected wave packet positioned between the two vertical lines of figures (a) and (b).

The results are given below:

- Transducer 1 resonant frequency is equal to 103.01 ± 0.05 MHz. This latter corresponds to a temperature of 26.91 ± 0.10 °C. The measurement uncertainty is equal to $\Delta T/T \approx 0.37$ %.
- Transducer 2 resonant frequency is equal to 85.21 ± 0.03 MHz. This latter corresponds to a temperature of 26.81 ± 0.05 °C. The measurement uncertainty is here equal to $\Delta T/T \approx 0.18$ %.
- The pool temperature estimated by the ILL was equal to $T = 26.76$ °C.
- The difference in the temperatures between the two ultrasonic transducers is equal to 0.10 °C and is found negligible with respect to the mean value of $T = 26.86$ °C. The difference with the ILL temperature value is $\Delta T = 0.15$ °C corresponding to an uncertainty of $\Delta T/T \approx 0.5$ %.
- The temperature difference value of 0.10 °C induces an ultrasound velocity measurement of $V = 1501 \pm 0.30$ m/s. The ultrasound velocity uncertainty is here equal to $\Delta V/V \approx 0.02$ %. This latter leads to a time of flight measurement uncertainty of $\Delta t/t \approx 0.2$ %.
- The previous uncertainty induce a general uncertainty measurement on the absolute distance of $\Delta d/d \approx 0.22$ % (such as $\Delta d \approx 3.9$ μm for $d = 1.8\ mm$).

In the following is presented the proof-of-concept process for distance estimation applied to all measurement series.

Water channel temperature measurements

The resonance frequency constitutes the varying parameter analyzed for the temperature estimation. The figure 6.6 presents the evolution of this characteristic for transducer 1 along the acquisitions when the device is inside the water channel.

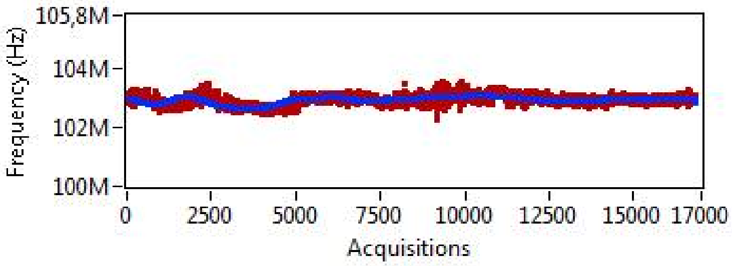

Figure 6.6: Transducer 1 resonance frequency evolution while introducing the ultrasonic device between plates 3 and 4. Red points correspond to the measured frequency and the blue squares to averaged values on 100 blue points.

The mean value of transducer 1 resonant frequency along the acquisitions is 102.9 MHz with a standard deviation of 0.1 MHz. Similar analysis using the resonant frequency values is realized for transducer 2. The water channel temperature values are then deduced from the previous resonant frequency measurements and showed in figure 6.7.

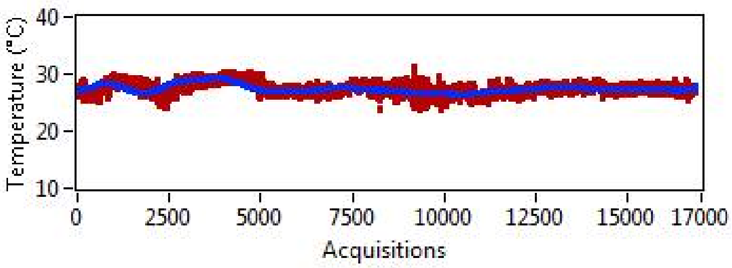

Figure 6.7: Temperature estimated by transducer 1 while introducing the ultrasonic device between plates 3 and 4. Red points correspond to the measured frequency and the blue squares to averaged values on 100 red points.

Figure 6.8 presents the comparison of the averaged temperature values estimated by both the ultrasonic transducers.
The mean temperature measured by transducer 1 is 27.4 °C with a standard deviation of ±1.4 °C. For transducer 2 the mean temperature is 27.2 °C with a standard

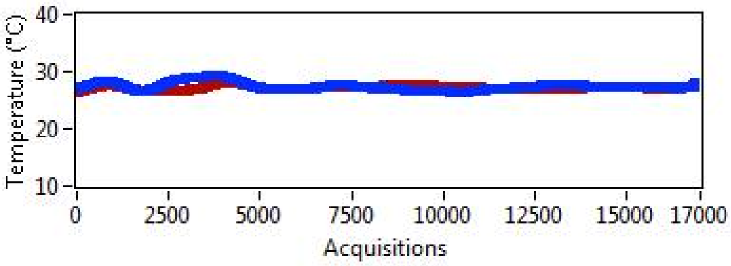

Figure 6.8: Temperature estimated by the transducers during the ultrasonic device introduction between plates 3 and 4. Blue points correspond to averaged temperature measured by transducer 1 and red squares to averaged temperature measured by transducer 2.

deviation of ±0.9 °C. The comparison of the temperatures of both transducers presented similarity along the acquisitions. Consequently, the temperature variation repeatability is confirmed and the ultrasonic velocity measurements are realized for each ultrasonic transducer according to its corresponding local temperature values along the acquisitions.

Water channel velocity estimation

The previous temperature measurements then allow the estimation of the ultrasonic velocity thanks to the figure 6.4 (a). These measurements are presented below in figure 6.9.

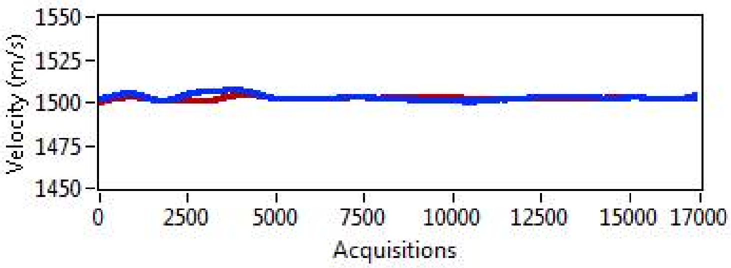

Figure 6.9: Ultrasonic velocities estimated by the transducers during the ultrasonic device introduction between plates 3 and 4. Blue points correspond to the averaged ultrasonic velocity measured by transducer 1 and the red squares to that measured by transducer 2.

The mean ultrasound velocity measured by transducer 1 is of 1502.9 m/s with a standard deviation of ± 3.5 m/s. For transducer 2 the average ultrasound velocity is of 1502.4 m/s with a standard deviation of ± 2.2 m/s. Indeed, the ultrasound velocities display a high local concordance between the transducers all along the acquisitions and consequently enable the inter-plate distance estimations.

Inter-plate distance estimation

For inter-plate distance estimation, the previous time of flight signal processing is here applied. First, the ultrasonic signals are filtered with an adequate bandpass filtering for noise decrease.

The second element to be investigated is the device positioning impact. Indeed, the ultrasonic transducers parallelism to the plates is of a high importance for the reception of the WP wave packets corresponding to the reflection on the fuel plates. In fact, in chapter 3, it was proven that an angle variation of $\Theta = 1°$ can impact the measurement results and resolution. In the following figures 6.10 (a) and (b) are presented two signals, the first without WP echo series due to a non parallel positioning of the device during its introduction and the second one containing the distinguished WP series.

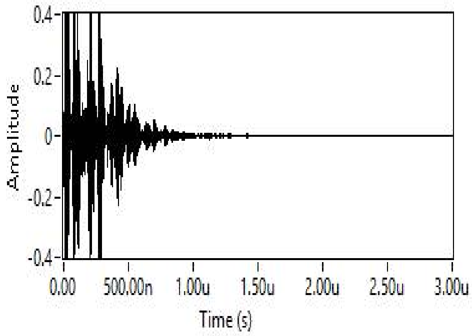

[a]

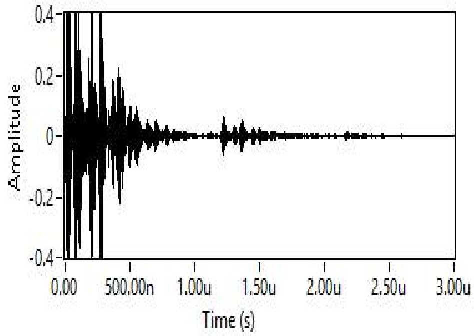

[b]

Figure 6.10: (a) Received ultrasonic signal without WP echo series; (b) Received ultrasonic signal with reflections on the fuel plate

Energy measurements

For an adequate inter-plate distance estimation, the measurement of the energy of signals received by each transducer is presented in the following.

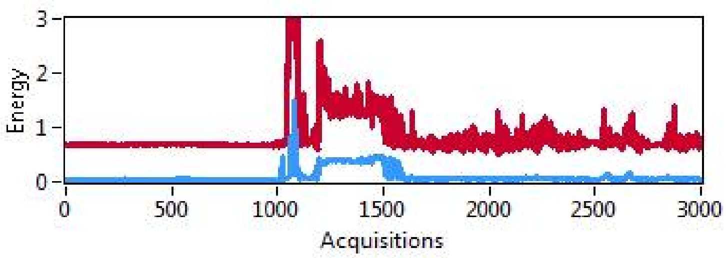

Figure 6.11: Energy measurements performed between plates 13 and 14. Red points correspond to transducer 1 energy measurements and blue squares for transducer 2.

The energy estimation shows two noticeable measurement levels:

- The first level shows a low amount of energy from the first acquisition until around the acquisition 1100, and after that from the acquisition 1600 until the end.
- The second level shows a high amount of energy from the acquisition 1100 to the acquisition 1600.

This result suggests that in the high energy part, the device was positioned with the most convenient parallelism to the fuel plates. These energy measurements allow the selection of the recorded acquisitions containing the reflection on the fuel plate, defined as the signals between the acquisitions 1200 and 1500.

Vertical position measurements

The position measurements are recorded along the experiment. As an example, the position measurements corresponding to the energies of figure 6.11 are presented in the following figure 6.12.

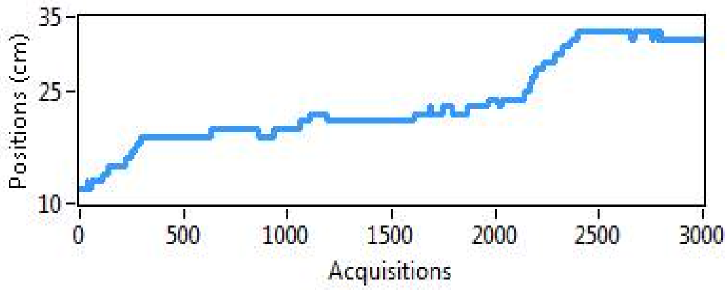

Figure 6.12: Device positionning measurements.

The positioning results display the fact that between the acquisitions 1200 and 1500, the ultrasonic device was in a stable position inside the fuel element in accordance with the fact that high energy signals were recorded. The signal processing is then realized on these signals in the following.

Reference signal subtraction

In a view to analyze only the WP echo series, the subtraction of the reference signal from the experimental signal is realized. The following figures 6.13 (a) and (b) show the signal with two sets of echoes before subtracting the reference signal.

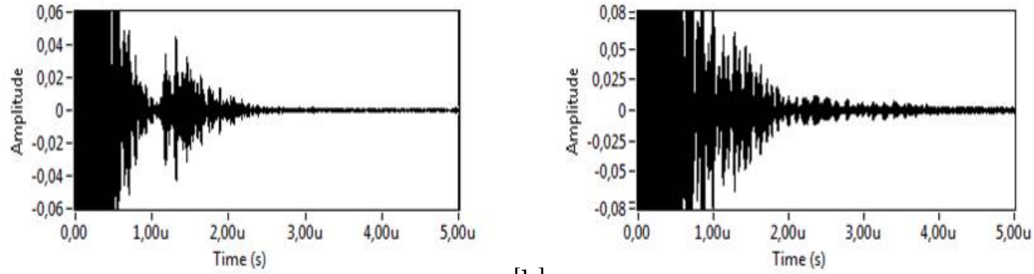

[a] [b]

Figure 6.13: (a) transducer 1 experimental signal; (b) transducer 2 experimental signal.

On transducer 1 experimental signal, the WP echo series is perfectly distinguished while on transducer 2 experimental signal, the series overlapping has clearly occurred. Such problem has been overcome thanks to the signal oversampling method for the adequate reference signal subtraction. Results are presented on the following figure 6.14

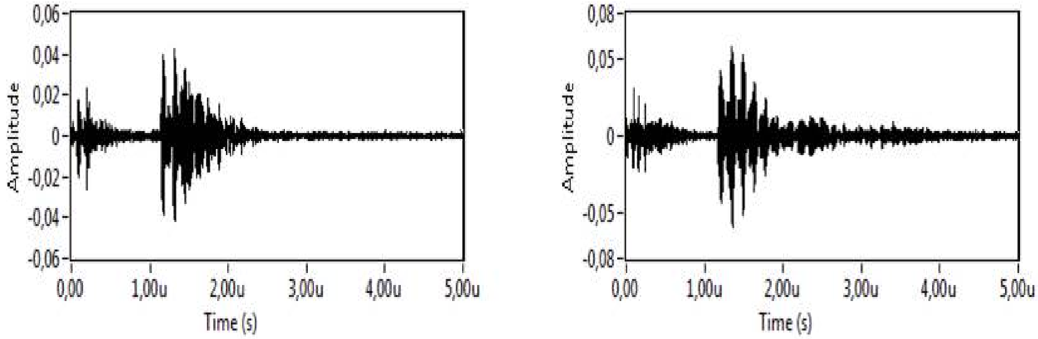

[a] [b]

Figure 6.14: Experimental signals after oversampled reference signal subtraction; (a) transducer 1 (b) transducer 2.

From figure 6.14, the WP echo series are identified for both transducers allowing cross-correlation measurements.

Distance estimation

Thanks to the cross-correlation computation between the reference signals and their corresponding in-situ signals, the time of flight measurements are realized. The corresponding inter-plate distance measurements are showed in figure 6.15.

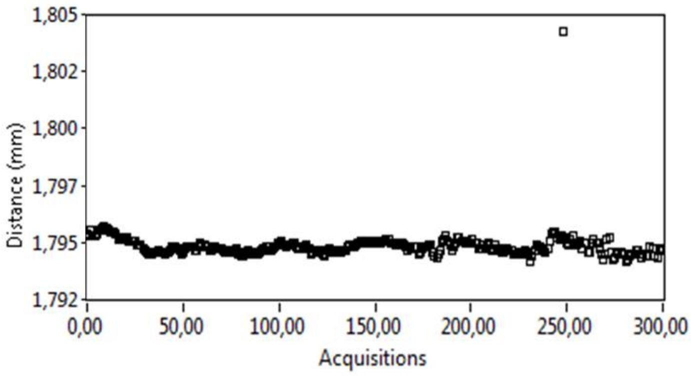

Figure 6.15: Inter-plate distance measurements.

The figure 6.15 displays stable inter-plate distance measurement results. Indeed, the average distance is estimated at $d = 1.795$ mm with a standard deviation of $\sigma = \pm 4$ μm.

Vertical position correspondence

In the following section, the previous distance measurements obtained and presented in figure 6.15 are combined with the positioning measurements previously displayed in figure 6.12.

6.4 Results and interpretation

The above protocol was followed on the reactor experiment while introducing the ultrasonic device in several water channels. The different results are presented in the following cases.

1. case 1: Inter-plate distance measurements while introducing the blade between plates 24 and 25 of the ILL fuel element.

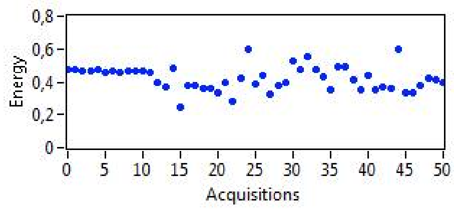

[a]

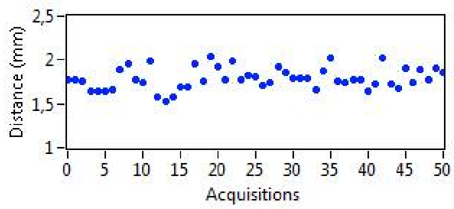

[b]

Figure 6.16: (a) Energy measurements along the acquisitions; (b) Inter-plate distance measurements along the acquisitions.

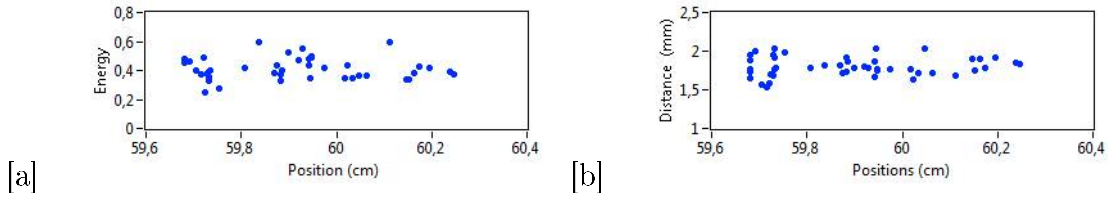

Figure 6.17: (a) Energy measurements according to the vertical position measurements; (b) Inter-plate distance measurements according to the vertical position measurements.

The energy measurements of the figure 6.16 (a) are dispersed all along the acquisitions. The inter-plate distance measurements presented in figure 6.16 (b) corresponding to these energy measurements display also highly dispersed results. Indeed the average value is estimated at $d = 1.79$ mm with a standard deviation of $\sigma = \pm 200$ μm.

Both energy and distance measurements are then correlated to the vertical positions respectively in figures 6.17 (a) and (b). Indeed, the previous dispersion is confirmed through different distances observed all along the analyzed zone and in particular on the same vertical zone between positions 59.69 cm and 59.89 cm. These distances are due to the low energy inducing a high dispersion.

2. case 2: Inter-plate distance measurements while introducing the blade between plates 13 and 14 of the ILL fuel element.

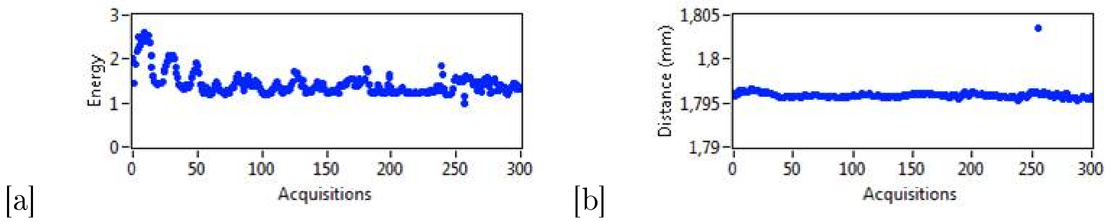

Figure 6.18: (a) Energy measurements along the acquisitions; (b) Inter-plate distance measurements along the acquisitions.

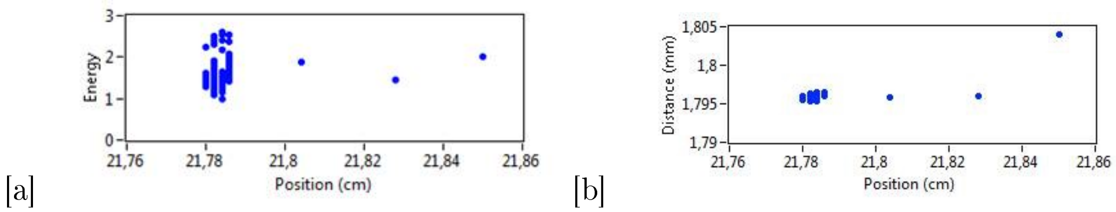

Figure 6.19: (a) Energy measurements according to the vertical position measurements; (b) Inter-plate distance measurements according to the vertical position measurements.

The energy measurements of figure 6.18 (a) display a stable amount of received energy during the acquisitions. The inter-plate distance measurements presented in the figure 6.18 (b) corresponding to these energy measurements display also very stable results.

Both energy and distance measurements are then correlated to the vertical position measurements respectively in figures 6.19 (a) and (b). The average distance is identified at $d = 1.795$ mm with a standard deviation of $\sigma = \pm 4\ \mu$m. Consequently a stable identification of the distance values can be observed in comparison to the first case results and with an advanced precision.

3. case 3: The inter-plate distance measurements while introducing the blade between the plates 3 and 4 of the ILL fuel element.

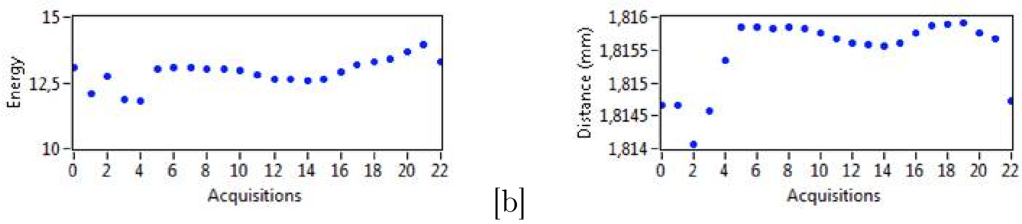

[a] [b]

Figure 6.20: (a) Energy measurements along the acquisitions; (b) Inter-plate distance measurements along the acquisitions.

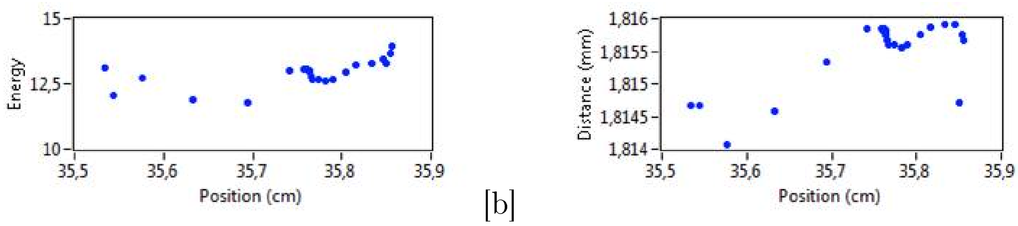

[a] [b]

Figure 6.21: (a) Energy measurements according to the vertical position measurements; (b) Inter-plate distance measurements according to the vertical position measurements.

The energy measurements presented in figure 6.20 (a) display a very high stable amount of energy received during the acquisitions, inducing very stable estimations of the inter-plate distances presented in figure 6.20 (b).

Both parameters are then correlated to the corresponding device vertical positions in figures 6.21 (a) and (b), on which their stability is confirmed. Indeed, the inter-plate distance measurements display results around the average value of $d = 1.815$ mm with a standard deviation of $\sigma = \pm\ 1\ \mu$m. In comparison with the case 2, these results display an even more stable identification of the inter-plate distance attaining a precision of $\pm\ 1\ \mu$m.

4. Comparison and analysis

   The first measurement case displays a high dispersion of distance values while the two following measurement cases display very stable measurements. These previous results were realized on selected signals with the best amount of energy received along the acquisitions. The noticed difference and the measurement dispersion probably comes from the following reason: the manual handling of the ultrasonic device induced its unstable positioning and consequently energy reception variations. Indeed, for the first case, the energy measurements were around an averaged value of 0.4 whereas for the second case they were around an averaged value of 2 and finally for the third case they attained the value of 13. This high energy difference increases the distance measurement resolution from $\pm$ 200 μm to $\pm$ 1 μm. Consequently, these results clearly prove the influence of the signal energy on the quality of the distance precision. While the actual device and associated signal processing allows the selection of signals allowing a precision of the order of the micrometer, the control of the positioning of the blade will have, in future works, to be optimized in a way to control the orientation of the sensors with respect to the plates' faces.

6.5 Conclusion

In this chapter, two elements were presented. First the new signal processing was applied to previous experiment measurements in a way to compare the distance measurement results. Second, the experiment realized in the High Flux Reactor fuel element is presented with its corresponding results.

For the first element under study, the advanced signal processing has greatly improved the inter-plate distance estimation. Indeed, for each ultrasonic transducer some inaccurate measurement results were removed. Consequently, the new signal processing methods are once again confirmed and present enough stability for distance estimation.

For the second objective, the application of the new developed ultrasonic device prototype through an experiment in the RHF fuel element has improved the reliability for evaluating both the medium temperature and the inter-plate distance and has introduced their matching to the device vertical position. In fact, the new prototype presents a unique silica support leading to several optimizations. First, the previous transducers' positioning deviation is reduced. Second, the inter-transducer parallelism is confirmed. Then, taking into account only high energy signals and applying the new signal processing, the resolution of the distance measurement is greatly improved.

Conclusion and prospects

In the framework of the LEU fuel element conversion, investigations of the selected fuel behavior are required. In this view, several programs were launched to analyze the post-irradiation aspects. One of the main aspects under study is: the fuel plate swelling. To address this issue, several destructive and non-destructive methods are proposed. The PERSEUS Project emphasizes on a direct phenomenon representing the fuel plate swelling: the water channel thickness variation. During a first project thesis, an ultrasonic device was developed and tested, allowing the validation of distance measurement feasibility through a non-destructive high frequency ultrasonic method. In this second thesis, the studies deal with the previous thesis feedback and flaws, allowing the realization of a new ultrasonic device implying a deep reflection over the device structure conception and optimization.

The new ultrasonic device and its components were fully discussed. It consists of two ultrasonic transducers implemented on one unique silica support, highly improving distance measurement precision. The device transducers frequency was studied through the ultrasonic field and the transducer multilayered composition behaviour modeling, in a way to obtain the best measurement resolution. After that, each component of the measurement chain was analyzed and its influence over acquisitions was developed. Consequently, an adequate echo identification and analysis of the acquired ultrasonic signal were realized. Then, a motorized measurement bench was mounted and included the determined axes influencing the ultrasonic field. Moreover, a linear cable sensor was introduced into the measurement bench allowing the device vertical position identification either in the laboratory or during the RHF experiments.

The signal processing was further discussed and evaluated. It was modified to improve the estimation of both time of flight and ultrasonic velocity. For time of flight evaluation, energy measurements were introduced for signals' selection, the substraction was optimized through signal oversampling up to 500 GHz and the echo type identification improved the validation of the cross-correlation results. For ultrasonic velocity, it is directly related to the water temperature estimation. Consequently, the ultrasonic echo selection allows to optimize the transducer central frequency monitoring, directly linked to the temperature value.

The previous enhancements have been investigated over reference samples by inter-faces distance reproducibility measurements. First, the identification of the distance measurement accuracy was performed thanks to a titanium element manufactured of 50 μm steps. Second, distance reproducibility measurement series were realized on a silica element with an inter-faces distance of 1800 μm $\pm$ 10 μm, corresponding to that of the fuel plates' interstice. Finally, measurements were realized in water channels of the RHF fuel element model. These experiments allow the identification of the ultrasonic device ability to achieve relative inter-plate distance measurements with a resolution estimated to 500 nm.

The new ultrasonic device characterization was completed according to the experimental constraints. During the reproducibility irradiation experiment, the 12 ultrasonic transducers and the device component samples were exposed to a 3500 kGy irradiation dose for 4 months. Corresponding to 10 hours of irradiation in contact with the fuel element, the ultrasonic device resistance to the irradiation environment is then assessed. This experiment necessitates specific electronic devices and the development of a complete software. This latter allows both the real-time and continuous monitoring of the transducers' parameters evolution and also the recording of corresponding data. The device performance stability through the materials robustness and the distance influencing parameters was then demonstrated.

To analyze the new signal processing advances, they were tested on experimental measurement series. A clear identification of inter-plate distances, initially defined as aberrant values, were then observed. Indeed, the signal processing steps definitely improve the signal acquisition flaws and validate the distance evaluation. The new developed non destructive high frequency ultrasonic device was then tested in the RHF fuel element. Through this experiment, the new device has consequently improved the reliability of both the water temperature and the water channel thickness evaluation and has introduced their link to the device vertical position.

The sensor misalignment being analyzed, the signal processing being precisely developed, the vertical position monitoring being introduced, the device irradiation resistance being studied and the water channel thickness being evaluated, several prospects can then be proposed for the non-destructive high frequency ultrasonic device.

First, the new ultrasonic device with its associated measurement bench would be tested in a future experiment in the RHF fuel element to allow high accurate line scan water channel thickness measurements. Consequently, the fuel plate swelling will be estimated, leading to the assessment of the swelling sources presented in 1.4.2.

Moreover, modeling the received ultrasonic signal, assuming a deposited oxide layer, is under study in order to analyze the most convenient parameters to implement in the ultrasonic device. On the other hand, for the plate internal structure analysis, especially for the interface between the cladding and the fuel analysis, focused transducers will be, in future works, studied and developed. In particular, employing focused transducers necessitates the development of complex models to assimilate the wave propagation in non-plane structures.

Furthermore, to monitor these studies on both sides of each fuel plate, mechanical modifications will be introduced. Indeed, a system with combined two ultrasonic devices can be proposed. A local characterization of the complete composition of the fuel plate will then be investigated. Furthermore, assuming the required ultrasonic systems positioning for the focused transducers' employment, the fuel plate imaging and its mechanical properties characterization will be explored.

Bibliography

[1] A. Leenaers et al. Leonidas e-future : Results of the destructive analyses of the U(Mo)-Al(Si) fuel plates. *JNM*, 335:39–47, 2004.

[2] John G. Stevens. Challenges of high performance research reactor conversions. 24 October 2014.

[3] Alexander Glaser. About the Enrichment Limit for Research Reactor Conversion : Why 20% ?. *The 27th International Meeting on Reduced Enrichment for Research and Test Reactors (RERTR)*, Boston, Massachusetts, 6-10 November 2005.

[4] www.heracles-consortium.eu/cp.php.

[5] B.D. Miller, J. Gan, J. Madden, J.F. Jue, A. Robinson, and D.D. Keiser Jr. Advantages and disadvantages of using a focused ion beam to prepare TEM samples from irradiated U–10Mo monolithic nuclear fuel. *Journal of Nuclear Materials*, 424, Issues 1–3:38–42, May 2012.

[6] `https://serc.carleton.edu/msu_nanotech/methods/EPMA.html`.

[7] Jong Man Park, Young Wook Tahk, Yong Ji Jeong, Kyu Hong Lee, Heemoon Kim, Yang Hong Jung, Boung-Ok Yoo, Young Gwan Jin, Chul Gyo Seo, Seong Woo Yang, Hyun Jung Kim, Jeong Sik Yim, Yeon Soo Kim, Bei Ye, and Gerard L. Hofman. Analysis on the post-irradiation examination of the HANARO miniplate-1 irradiation test for kijang research reactor. *Nuclear Engineering and Technology*, 49, Issue 5:1044–1062, August 2017.

[8] David Willingham, Benjamin E. Naes, Jay G. Tarolli, Alan Schemer-Kohrn, Mark Rhodes, Michael Dahl, Anthony Guzman, and Douglas E. Burkes. Image fusion of secondary ion mass spectrometry and energy-dispersive x-ray spectroscopy data for the characterization of uranium-molybdenum fuel foils. *Journal of Nuclear Materials*, 498:348–354, January 2018.

[9] A. Delfin and R. Mazón. Visual inspection system and sipping design for spent fuel at TRIGA MARK III reactor of Mexico. *International Meeting on Reduced Enrichment for Research and Test Reactors*, Bariloche, Argentina, November 3-8, 2002.

[10] A.A Terremoto, C.A Zeituni, J.A Perrotta, and J.E.R da Silva. Gamma-ray spectroscopy on irradiated MTR fuel elements. *Nuclear Instruments and Methods in Physics Research Section A: Accelerators, Spectrometers, Detectors and Associated Equipment*, 450, Issues 2–3:495–514, 11 August 2000.

[11] A. R. Reddy and M. V. N. Rao. Neutron radiography. *Defence Science Journal*, 32, No 3:259–273, July1982.

[12] A. Leenaers, Y. Parthoens, G. Cornelis, V. Kuzminov, E. Koonen, S. Van den Berghe, B. Yeb, G.L. Hofman, and J. Schulthess. Effect of fission rate on the microstructure of coated UMo dispersion fuel. *Journal of Nuclear Materials*, 494:10–19, October 2017.

[13] www.ill.eu.

[14] A. Bergeron, A. Tentner, and J.G. Stevens. Feasability Analyses for HEU to LEU Fuel Conversion of the Laue Langevin Institute (ILL) High Flux Reactor (RHF). Technical Report. United States: N. p. August 2010.

[15] The HERACLES Working Group CEA, AREVA-CERCA, ILL, SCK-CEN, TUM. Heracles-cp: Towards the conversion of high performance research reactors in europe. 2014.

[16] U.S. Nuclear Regulatory Commission. Safety Evaluation Report related to the Evaluation of Low-Enriched Uranium Silicide-Aluminum Dispersion Fuel for Use in Non-Power Reactors, Report NUREG-1313. July 1988.

[17] A. Travelli. Progress of the RERTR Program in 1999. *in Proceedings of the XXII International Meeting on Reduced Enrichment for Research and Test Reactors*, Budapest, Hungary, 3-8 October 1999.

[18] A. Travelli. The RERTR program: a status report. *Proceedings of the 21th International Meeting on Reduced Enrichment for Research and Test Reactors*, Sao Paulo, Brazil, 18-23 October 1998.

[19] G. Zaz, A. Dekkious, P. A. Meignen, Y. Calzavara, E. Le Clézio and G. Despaux. High Frequency Transducer Dedicated to the High-resolution in Situ Measurement of the Distance between Two Nuclear Fuel Plates. *Phys. Procedia*, 70:103–104, ICU Metz, 2015.

[20] G. Zaz, Y. Calzavara, E. Le Clézio and G. Despaux. High frequency piezoelectric transducer dedicated to the first experimentation of a high resolution measurement of inter-plate distance in a high flux reactor. INSA-CVL, Blois, France, 25-26 September 2014.

[21] www.edf.fr/edf/crayon-et-assemblage-combustible.

[22] U. Koster, Y. Calzavara, S. Fuard, M. Samuel, H. Dorrer, K. Zhernosekov, M. Harfensteller, S. Marx, M. Jensen. 319 RADIOISOTOPE PRODUCTION AT THE HIGH FLUX REACTOR OF INSTITUTE LAUE LANGEVIN. *Radiotherapy and Oncology*, 102, Supplement 1:S170, March 2012.

[23] A. Blanc, A. Chebboubi, H. Faust, M. Jentschel, G. Kessedjian, U. Köster, T. Materna, S. Panebianco, C. Sage, W. Urban. Fission Product Prompt c-ray spectrometer: Development of an instrumented gas-filled magnetic spectrometer at the ILL. *Nuclear Instruments and Methods in Physics Research Part B*, 317:333–337, 15 December 2013.

[24] Salvatore Magazù, Federica Migliardo, Antonio Benedetto, Beata Vertessy. Protein dynamics by neutron scattering: The protein dynamical transition and the fragile-to-strong dynamical crossover in hydrated lysozyme. *Chemical Physics.*, 424, 2013.

[25] G.F. Elliot, Z. Sayers, P.A. Timmins. Neutron Diffraction Studies of the Comeal Stroma. *Journal of Molecular Biology.*, 155, Issue 3:389–393, 5 March 1982.

[26] Ann Leenaers. Surface-engineered low-enriched Uranium-Molybdenum fuel for research reactors. *PhD thesis 2014, University of Ghent – SCK CEN, ISBN-9789076971223.*

[27] www.encyclopedie-energie.org/articles/les-réacteurs-de-recherche.

[28] www.atominfo.cz/2015/03/cesky-patent-zvyseni-bezpecnosti-jadernych-zarizeni-pomoci-diamantu/.

[29] http://www.world-nuclear.org/information-library/nuclear-fuel-cycle/conversion-enrichment-and-fabrication/uranium-enrichment.aspx.

[30] M.K. Meyer, J. Gan, J.F. Jue, D.D. Keiser, E. Perez, A. Robinson, D.M. Wachs, N. Woolstenhulme, G.L. Hofman, and Y.S. Kim. Irradiation performance of U-Mo monolithic fuel. *Nuclear Engineering and Technology*, 46, Issue 2:169–182, April 2014.

[31] S. Nazaré. Low enrichment dispersion fuels for research and test reactors. *Journal of Nuclear Materials*, 124:14–24, 3 May 1984.

[32] M.F. Hrovat and H.W. Hassel. Proceeding of the International Meeting on Reduced Enrichment for Research and Test Reactors. Tokai, Japan, 24-27 Oct. 1983.

[33] Y. Fanjas, Ph Dewez and B. Savonin. Proceeding of the International Meeting on Reduced Enrichment for Research and Test Reactors. Tokai, Japan, 24-27 Oct. 1983.

[34] Energy: Nuclear: Advanced reactor concepts and fuel cycle technologies. page 64, 2005.

[35] Carl E. Behrens and Carol Glover. *Nuclear: Energy advanced reactor concepts and fuel cycle technologies. Chapter 14: Nuclear fuels and materials spotlight.* 2005.

[36] S. J. B. Reed. *Electron Microprobe Analysis and Scanning Electron Microscopy in Geology.* 2005.

[37] A. Leenaers, S. Van den Berghe, J. Van Eyken, E. Koonen, F. Charollais, P. Lemoine, Y. Calzavara, H. Guyond, C. Jarousse, D. Geslin, D. Wachs, D. Keiser, A. Robinson, G. Hofman, and Y.S. Kim. Microstructural evolution of U(Mo)–Al(Si) dispersion fuel under irradiation – destructive analyses of the LEONIDAS E-FUTURE plates. *Progress in Nuclear Energy*, 441, Issues 1–3:439–448, October 2013.

[38] B. T. Bradbury, J. T. Demant, P. M. Martin, et D. M. Poole. Electron probe micro-analysis of irradiated UO2. *Journal of Nuclear Materials*, 17:227–236, 1965.

[39] Aslina Br. Gintinga and Peng Hong Liemb. Absolute burnup measurement of leu silicide fuel plate irradiated in the RSG GAS multipurpose reactor by destructive radiochemical technique. *Annals of Nuclear Energy*, 85:613–620, November 2015.

[40] S. Van den Berghe, Y. Parthoens, G. Cornelis, A. Leenaers, E. Koonen, V. Kuzminov, and C. Detavernier. Swelling of U(Mo) dispersion fuel under irradiation – Non-destructive analyses of the SELENIUM plates. *Journal of Nuclear Materials*, 442:60–68, 2013.

[41] A. Alghem, M. Kadouma, and R. Benaddad. NDT as a tool, for Post-Irradiation Examination. *Abstracts of 17th World Conference on Non-Destructive Testing*, Shanghai, China, 25-28 Oct 2008.

[42] L. Sannen, L. Borms, C. de Raedt, and A. Gys. SCK'CEN, Mol, Belgium. Gamma-spectrometric determination of the fission power of fuel rods. *Proceeding of a Technical Committee meeting held in Dimitrovgrad, Russian Federation*, 17, 2001.

[43] H. Seo, J.-M. Oh, H.-S. Shin, H. Kim, S. K. Lee, H. S. Lee, et S.-H. Park. Burnup Measurement of Spent Fuel Assembly by CZT-based Gamma-Ray Spectroscopy for Input Nuclear Material Accountability of Pyroprocessing. *IEEE Transactions on Nuclear Science*, 61:2169–2174, August 2014.

[44] S. Van den Berghe, Y. Parthoens, F. Charollais, Y.S. Kim, A. Leenaers, E. Koonen, V. Kuzminov, P. Lemoine, C. Jarousse, H. Guyon, D. Wachs, D. Keiser Jr, A. Robinson, J. Stevens, and G. Hofman. Swelling of U(Mo)–Al(Si) dispersion fuel under irradiation – non-destructive analyses of the LEONIDAS E-FUTURE plates. *Journal of Nuclear Materials*, 430:246–258, November 2012.

[45] A. Bergerion, B. Dionne, Y. Calzavara. Neutronics Conversion Analyses of the Laue-Langevin Institute (ILL) High Flux Reactor (RHF). *Nuclear Engineering Division, Argonne National Laboratory, United States*, September 2014.

[46] Y. Calzavara, F. Frery, F. Thomas, H. Guyon, A. Beregeron, A. Tentner, J. Stevens and W. Haeck. TOUTATIS: ILL conversion feasibility study. *in the 32th International Meeting on Reduced Enrichment for Research and Test Reactors, Lisbon, Portugal*, October 2010.

[47] G. Zaz, Y. Calzavara, E. Le Clézio and G. Despaux. Mesure haute résolution in situ de la distance entre deux plaques combustibles nucléaires. pages 1191–1195, CFA, Poitiers, 22–25 Avril 2014.

[48] Daniele Marioli and Emilio Sardini and Andrea Taroni. Ultrasonic Distance Measurement for Linear and Angular Position Control. *IEEE Transactions on instrumentation and measurement*, 37, December 1988.

[49] G. Zaz, Y. Calzavara, E. Le Clézio and G. Despaux. Adaptation of a High Frequency Ultrasonic Transducer to the Measurement of Water Temperature in Nuclear Reactor. *Physics Procedia*, 70:195–198, ICU, Metz, 2015.

[50] G. Zaz, E. Le Clézio, A. Dekious, M. Chrifi Alaoui, Y. Calzavara and G. Despaux. In-situ high-resolution measurement of RHF nuclear fuel plates' spacing. *IEEE Transactions on Nuclear Science*, 65, november 2018.

[51] G. ZAZ. *PhD Thesis: Post Examination of a High Flux Reactor Single Element with Ultra-Sounds.* 2015.

[52] G. Zaz, E. Le Clézio, Y. Calzavara and G. Despaux. Mesure de distance interplaques par méthode ultrasonore haute fréquence. JAPSUS, Montpellier, 12-14 Juin 2013.

[53] G. Zaz, Y. Calzavara, E. Le Clézio and G. Despaux. Post examination of the reactor high flux single element with ultra-sounds. HERCALESUS, Technical Meeting, Argonne National Laboratory Nuclear Engineering Division Argonne, Illinois on October 28-30, 2013.

[54] D. Marioli, C. Narduzzio, C. Offelli, D. Petri, E. Sardini and A. Taroni. Digitial Time-of-Flight Measurement for Ultrasonic Sensors. *IEEE Transactions on Instrumentation and Measurement*, 41, February 1992.

[55] A.N. Sinclair, A.M. Chertov. Radiation endurance of piezoelectric ultrasonic transducers – A review. *Ultrasonics*, 57:1–10, 2015.

[56] D. L. Folds and C. D. Loggins. Transmission and reflection of ultrasonic waves in layered media. *The Journal of the Acoustical Society of America*, 62:1102, 1998.

[57] A.L. Shuvalov, E. Le Clézio, G. Feuillard. The state-vector formalism and the Peano-series solution for modelling guided waves in functionally graded anisotropic piezoelectric plates. *International Journal of Engineering Science*, 46, Issue 9:929–947, September 2008.

[58] M. Lam, E. Le Clézio, H. Amorín, M. Algueró, Janez Holc, Marija Kosec, A.C. Hladky-Hennion, G. Feuillard. Acoustic wave transmission through piezoelectric structured materials. *Ultrasonics*, 49, Issues 4–5:424–431, May 2009.

[59] Thomas L. Szabo. *Diagnostic ultrasound imaging: inside out.* May 2004.

[60] J.W. Strutt, B. Rayleigh. *Theory of sound Volume II.* 1896.

[61] www.nde-ed.org/EducationResources/CommunityCollege/communitycollege.php.

[62] W. G. McMullan, B. A. Delanghe, and J. S. Bird. A simple Rising-Edge Detector for Time-of-Arrival Estimation. *IEEE Transactions on Instrumentation and Measurement.*, 45, Issue 4:823 – 827, August 1996.

[63] Billur Barsham. Fast processing techniques for accurate ultrasonic range measurements. *Measurement Science Technology*, 11, 2000.

[64] Y. Xu, Y. Li, Z. Qu, S. Jin, and C. Jiang. A TOF Estimation Method for Underwater Acoustic Signal in Confined Underwater Space. *Comput. Inf. Syst.*, 8:1689–1696, 2012.

[65] R. Queiros, F. Correa Algeria, P. Silva Girao, and A. Cruz Serra. Cross-Correlation and Sine-Fitting Techniques for High-Resolution Ultrasonic Ranging. *IEEE Transactions on Instrumentation and Measurement.*, 59, Issue 12:3227 – 3236, May 2010.

[66] J. C. Jackson, R. Summan, G. I. Dobie, S. M. Whiteley, S. G. Pierce, and G. Hayward. Time-of-flight measurement techniques for airborne ultrasonic ranging. *IEEE Transactions on Ultrasonics, Ferroelectrics and Frequency Control*, 60, Issue 2:343 – 355, February 2013.

[67] J. A. Capp and L. T. Robinson. Thermocouples and resistance coils for the determination of local temperatures in electrical machines. *Transactions of the Amercian Institute of Electrical Engineers*, 32, Issue 3:701 – 708, 1913.

[68] A. S. Morris. *Measurement and instrumentation principles.* 2001.

[69] S. Basu and A. Debnath. Power Plant Instrumentation and Control Handbook: A Guide to Thermal Power Plants. *Academic Press.*, 2014.

[70] R. Usamentiaga, P. Venegas, J. Guerediaga, L. Vega, J. Molleda, and F. Bulnes. Infrared Thermography for Temperature Measurement and Non-Destructive Testing. *Sensors*, 14:12305–12348, 2014.

[71] N. Bilaniuk et G. S. K. Wong. Speed of sound in pure water as a function of temperature. *The journal of the Acoustical Society of America.*, 93, Issue 3, 1993.

[72] https://goochandhousego.com.

[73] Xuefeng Li, Shuo Lin, Jinxing Liang, Yupeng Zhang, H. Oigawa, and T. Ueda. Fiber-Optic Temperature Sensor Based on Difference of Thermal Expansion Coefficient Between Fused Silica and Metallic Materials. *IEEE Photonics*, 4:155 – 162.

[74] C. J. Bell, S. Reid, J. Faller, G. D. Hammond, J. Hough, I. W. Martin, S. Rowan, and K. V. Tokmakov. Experimental results for nulling the effective thermal expansion coefficient of fused silica fibres under a static stress. *Classical and Quantum Gravity*, 31, 2014.

[75] U. Rössler. Solid State Theory: An Introduction. *Springer Science and Business Media.*, 2013.

[76] R. T. Smith and F. S. Welsh. Temperature Dependence of the Elastic, Piezoelectric, and Dielectric Constants of Lithium Tantalate and Lithium Niobate. *J. Appl. Phys*, 42, 1971.

[77] S. C. Abrahams, H. J. Levinstein, and J. M. Reddy. Ferroelectric lithium niobate. 5. Polycrystal X-ray diffraction study between 24° and 1200°C. *J. Phys. Chem. Solids*, 27, Issues 6–7:1019–1026, 1966.

[78] F. Pignatiello, M. De Rosa, P. Ferraro, S. Grilli, P. De Natale, A. Arie, and S. De Nicola. Measurement of the thermal expansion coefficients of ferroelectric crystals by a moiré interferometer. *Optics Communications*, 277:14–18, 2007.

[79] J. D. James, J. A. Spittle, S. G. R. Brown, and R. W. Evans. A review of measurement techniques for the thermal expansion coefficient of metals and alloys at elevated temperatures. *Meas. Sci. Technol*, 12:R1–R15, 2001.

[80] Daniel Kremer. Usinage par électroérosion. *Techniques de l'ingénieur*, 2000.

[81] www.arc-nucleart.fr.

[82] www.harwell-dosimeters.co.uk.

[83] www.pva-analyticalsystems.com.

[84] Pierre-Antoine Meignen, Emmanuel Le Clézio, Gilles Despaux. High Frequency Acoustic Sensor Dedicated to the High Resolution Measurement of Mechanical Properties. *Physics Procedia*, 70:424–427, 2015.

[85] D. Laux, D. Baron, G. Despaux, A.I. Kellerbauer, M. Kinoshita. Determination of high burn-up nuclear fuel elastic properties with acoustic microscopy. *Journal of Nuclear Materials*, 420:94–100, 2012.

[86] D. Laux, W. de Weerd, D. Papaioannou, S. Kitajima, V.V. Rondinella, G. Despaux. Scanning acoustic microscope for mechanical characterization and density estimation of irradiated nuclear fuel. *Progress in Nuclear Energy*, 72:63–66, 2014.

Communications

International article

G. Zaz, E. Le Clézio, A. Dekious, M. Chrifi Alaoui, Y. Calzavara and G. Despaux, **"In-situ high-resolution measurement of RHF nuclear fuel plates' spacing"**, IEEE Transactions on Nuclear Science, Volume: 65, Issue: 11, Nov. 2018

Communications with proceedings in an international congress

Dr G. Zaz, Pr. E. La Clézio, M. Chrifi Alaoui Dr Y. Calzavara, Pr. G. Despaux, **"High-resolution ultrasonic sensor dedicated to in-situ nuclear fuel swelling measurements"**, IEEE Sensors 2016, Orlando (USA), 30 Octobre - 2 Novembre 2016.

M. Chrifi Alaoui, Dr G. Zaz, Pr. E. Le Clézio, Dr Y. Calzavara, Pr. G. Despaux, **"Mesure de distance inter-plaques d'un réacteur RHF par méthode ultrasonore haute fréquence "**, 3ème Colloque International sur le Monitoring des Systèmes Industriels, CIMSI'2016, Fès (Maroc), 19-20 Octobre 2016.

Communications with proceedings in a national congress (France)

M. Chrifi Alaoui, Dr G. Zaz, Pr. E. Le Clézio, Dr Y. Calzavara, Pr. G. Despaux, **"Caractérisation ultrasonore de distances inter-plaques au sein d'un réacteur RHF"**, 13ème Congrès Français d'Acoustique et 20ème colloque Vibrations, Shocks and Noise (CFA/VISHNO), Le Mans (France) 2016.

M. Chrifi, Dr G. Zaz, Pr. E. Le Clézio, Dr Y. Calzavara, Pr. G. Despaux, **"Caractérisation ultrasonore hautes fréquences de la distance inter-plaques au sein de réacteurs RHF"**, 7ème Colloque Interdisciplinaire en Instrumentation (C2I), Saint-Nazaire (France) 2016.

Communications without proceedings in national and international congress

M. Chrifi Alaoui, E. Le Clézio, Y. Calzavara, G. Despaux, **"Tenue aux radiations de capteurs ultrasonores haute fréquence dédiés à la mesure de distance au sein de réacteurs à haut flux"**, 14ème Congrès Français d'Acoustique, Le Havre (France) Avril 23-27, 2018.

M. Chrifi Alaoui, E. Le Clézio, Y. Calzavara, G. Despaux, **"High-resolution ultrasonic sensor for channel gap thickness measurement"**, Reduced Enrichment for Research and Test Reactors meeting (RERTR Meeting) 2017 Chicago (USA) November 12-16, 2017.

M. Chrifi Alaoui, G. Zaz, E. Le Clézio, Y. Calzavara, G. Despaux, **"Ultrasonic transducer dedicated to in situ high-resolution measurement of inter-fuel-plate distance"**, Anglo French Physical Acoustic Conference (AFPAC), 2017 Marseille (France), 23-25 Janvier 2017.

List of Figures

1 Imagerie d'une plaque combustible dévoilant un gonflement. . 11

2 Image de l'élément combustible du RHF. 12

3 Composition multicouche du transducteur ultrasonore et signal reçu suite à la propagation des ondes jusqu'à l'interface eau/plaque. 13

4 Image du sabre et signal ultrasonore à échos électriques (en rouge) et échos acoustiques (en bleu). 15

5 Banc de mesure. 15

6 Superposition des signaux avant (rouge) et après (noir) soustraction optimisée de référence. 16

7 Résultat de corrélation via le positionnement du signal de référence (rouge) à l'emplacement de détection de la seconde série (noir). 16

8 Résultat de 10 mesures de reproductibilité sur l'élément en silice de 1800 μm $\pm$ 10 μm d'interstice. 17

9 (a) Installation des dispositifs et ses composants en cellule d'irradiation, (b) Composants électroniques pour le suivi des dispositifs sous irradiation. 18

10 Image du sabre introduit entre deux plaques combustibles et graphe de mesure de distance en fonction de la position verticale. 19

1.1 Scheme of the High Flux Reactor installation of the Institute Laue Langevin of Grenoble in France. 27

1.2 Schematic overview of the neutron capture by a ^{235}U nucleus [26]. 28

1.3 Curved and flat fuel plate assemblies [27]. 28

1.4 (a) Monolithic Fuel Cross-section, (b) Dispersion Fuel Cross-section. 30

1.5 Irradiation comprehension phase steps of the HERACLES program. 32

1.6 The High Flux Reactor structure [13], (a) main components of the reactor building, (b) specified components of the High Flux Reactor. 36
1.7 (a) General structure of the RHF fuel element [13], (b) zoom over fuel plates. 37
1.8 The fuel plate dimensions [45]. 37
1.9 General principle of inter-plate distance measurement. 39
1.10 Experimental ultrasonic signal displaying two echo series, (I) reflected echo series on the silica support, (II) reflected echo series on the plate. 40
1.11 Inter-plate distance measurements. 40

2.1 General principle of inter-plate distance measurement. 45
2.2 Innovative structure improvement illustration. 46
2.3 Multilayered composition of the transducer. 48
2.4 Modeled ultrasonic signal of a 90 MHz central frequency transducer displaying two echo series, (a) reflected echo series on the silica/water interface, (b) reflected echo series on the water/plate interface. 49
2.5 (a) Modeled received ultrasonic signal with an adhesive layer thickness of 13 μm; (b) Reflected series on the WP interface. . 50
2.6 Modeled received ultrasonic signal with an adhesive layer thickness of 10 μm; (b) Reflected series on the WP interface. 50
2.7 Ultrasonic field generated in water by a 1 mm diameter plane surface at 90 MHz. 51
2.8 Ultrasonic field generated in silica and water by a 1 mm diameter plane surface at 90 MHz. (a) displayed in the silica of 0.4 mm, (b) displayed until 20 mm. 52
2.9 Ultrasonic field generated in silica and water by a 0.5 mm diameter plane surface at 90 MHz. (a) displayed until 2 mm, (b) displayed until 20 mm. 53
2.10 Blade to support connection and stainless tube support. . . . 53
2.11 Assembled ultrasonic device. 54
2.12 The chassis including electronic instruments. 54
2.13 Signal received through a cable of 8 m: (a) before (b) after filtering. 55

2.14 Electric (black) and acoustic (red) echoes considering a cable of 8 m. 55
2.15 (a) Reflected signal on the cable (b) reflected signal through the transducer. 56
2.16 Two signals: (red) signal received after the transducer excitation and filtered; (black) signal received after the transducer excitation without filtering. 56
2.17 Scheme of the blade positioning between two plates. 57
2.18 Measurement bench design: (1) ULM-TILT, (2) rotational motor, (3) mounting support, (4) dual translation plates, (5) translation plate. 58
2.19 (a) NI−9411 card for counting and position indicating; (b) Linear cable sensor. 59
2.20 Laboratory experimental bench. 60

3.1 Ultrasonic wave propagation through the mediums and the corresponding acquired signal including two echo series. 62
3.2 (a) Acquired ultrasonic signal before bandpass filtering; (b) Acquired ultrasonic signal after bandpass filtering. 65
3.3 An ultrasonic signal with three reflected echo series from the facing sample surface. 66
3.4 (a) Acquired ultrasonic signal with distinguished reflected series; (b) Acquired ultrasonic signal with overlapped reflected series. 66
3.5 (a) First case ultrasonic signal after reference signal subtraction; (b) Second case ultrasonic signal after reference signal subtraction. 67
3.6 (a) Supperposition of the acquired ultrasonic signal and the reference signal; (b) One time period of both the signals in points. 67
3.7 Time of flight measurement results. 68
3.8 An ultrasonic signal superposed with its oversampled signal, (a) ultrasonic echo, (b) a zoom over 2 ns. 68
3.9 First case after reference signal subtraction; (a) without oversampling, (b) with oversampling. 69
3.10 Second case after reference signal subtraction; (a) without oversampling, (b) with oversampling. 69
3.11 Superposed reference and experimental signals: delayed reference signal in red and subtracted signal in black, (a) visualization of complete signals (b) a zoom on the WP series. 70

3.12 Ultrasound velocity in function of temperature. 72

3.13 Temperature measurement bench. 74

3.14 Ultrasonic signals received by the transducer 1 (a) and the transducer 2 (b) under the first device positioning 1. 75

3.15 Frequency variation according to the temperature. Blue squares correspond to the simulated values and red points to the experimental data 75

3.16 Ultrasound velocity in function of central frequency. 76

4.1 (a) Titanium element scheme (b) Optic imaging of the titanium element steps. 78

4.2 Titanium element relative measurements. 79

4.3 Ultrasonic signals received by the transducer 1 (a) and the transducer 2 (b) under the first device positioning 1. 80

4.4 Ultrasonic signals received by the transducer 1 (a) and the transducer 2 (b) under the second device positioning 80

4.5 Scheme of the ultrasonic device inside the silica sample assuming a $\Theta = 1\,°$ transducers' parallelism difference. 81

4.6 Scheme of the ultrasonic transducer positioning. 81

4.7 Configuration 1 measurement results. 82

4.8 Configuration 2 measurement results. 83

4.9 Configurations 1 and 2 measurement results. 84

4.10 Configuration 3 measurement results. 84

4.11 Configuration 4 measurement results. 85

4.12 Configuration 5 measurement results. 86

4.13 Configuration 5 measurement results over the zone (a). 86

4.14 Configuration 5 measurement results over the zone (b). 87

4.15 All positioning configurations measurement results. 88

4.16 The RHF fuel element model. 89

4.17 (a) Developing circle form modeling (b) Two plates with 1.8 mm segments. 89

4.18 Ultrasonic device emplacements' modeling between two plates. 90

4.19 Results of a RHF model water channel thickness measurements. 91

4.20 Results of a RHF model water channel thickness measurements. 91

5.1 Nuclear irradiator installation scheme. 95

5.2 Cobalt disintegration principle. 96

5.3 Carrier panel inserted in the irradiation cell [81]. 97

5.4 Red Perspex dosimeter 97

5.5 measurement system scheme. 99

5.6 Ultrasonic devices and single elements in the irradiation cell. . 99

5.7 Acquisition software block diagram. 100

5.8 Acquisition program interface. 101

5.9 Acquisition and monitoring system placed outside the irradiation cell. 101

5.10 Reference transducers and cables spectra at the laboratory. . . 103

5.11 Reference transducers spectra outside the irradiation cell and irradiated cables spectra during irradiation experiment. 104

5.12 Ultrasonic transducers spectra before the irradiation experiment. 105

5.13 Ultrasonic transducers spectra all over the irradiation experiment days. 106

5.14 Relative frequency, amplitude and bandwidth variation of reference transducers and cables: first line graphs are at laboratory and second line graphs are outside irradiation cell for reference transducers while cables are irradiated. 107

5.15 Relative frequency, amplitude and bandwidth variation of the transducers. 109

5.16 Time signal comparison between the functioning case (red) and the malfunctioning case (blue). 111

5.17 multilayered structure group images before and after the irradiation. 113

5.18 multilayered structure group microscopic images before irradiation. 114

5.19 multilayered structure group microscopic images after irradiation. 114

5.20 Acoustic signature process. 115

6.1 (a) Experimental signal energy measurements; (b) Selected signals for distance measurements. 120

6.2 (a) Previous and new signal processing comparison; (b)New signal processing distance measurements. 121

6.3 New ultrasonic device in the RHF experiment [13] (a) inserted in the fuel element; (b) introduced between fuel plates. 122
6.4 Frequency variation according to the temperature. Blue squares correspond to the simulated values and red points to the experimental data; (a) transducer 1; (b) transducer 2. 123
6.5 (a) and (b) Both transducers' received ultrasonic signals in the medium; (c) and (d) Both transducers' frequency spectra of the selected wave packet positioned between the two vertical lines of figures (a) and (b). 124
6.6 Transducer 1 resonance frequency evolution while introducing the ultrasonic device between plates 3 and 4. Red points correspond to the measured frequency and the blue squares to averaged values on 100 blue points. 125
6.7 Temperature estimated by transducer 1 while introducing the ultrasonic device between plates 3 and 4. Red points correspond to the measured frequency and the blue squares to averaged values on 100 red points. 125
6.8 Temperature estimated by the transducers during the ultrasonic device introduction between plates 3 and 4. Blue points correspond to averaged temperature measured by transducer 1 and red squares to averaged temperature measured by transducer 2. 126
6.9 Ultrasonic velocities estimated by the transducers during the ultrasonic device introduction between plates 3 and 4. Blue points correspond to the averaged ultrasonic velocity measured by transducer 1 and the red squares to that measured by transducer 2. 126
6.10 (a) Received ultrasonic signal without WP echo series; (b) Received ultrasonic signal with reflections on the fuel plate . . . 127
6.11 Energy measurements performed between plates 13 and 14. Red points correspond to transducer 1 energy measurements and blue squares for transducer 2. 127
6.12 Device positionning measurements. 128
6.13 (a) transducer 1 experimental signal; (b) transducer 2 experimental signal. 129
6.14 Experimental signals after oversampled reference signal subtraction; (a) transducer 1 (b) transducer 2. 129
6.15 Inter-plate distance measurements. 130
6.16 (a) Energy measurements along the acquisitions; (b) Inter-plate distance measurements along the acquisitions. 130

6.17 (a) Energy measurements according to the vertical position measurements; (b) Inter-plate distance measurements according to the vertical position measurements. 131
6.18 (a) Energy measurements along the acquisitions; (b) Inter-plate distance measurements along the acquisitions. 131
6.19 (a) Energy measurements according to the vertical position measurements; (b) Inter-plate distance measurements according to the vertical position measurements. 131
6.20 (a) Energy measurements along the acquisitions; (b) Inter-plate distance measurements along the acquisitions. 132
6.21 (a) Energy measurements according to the vertical position measurements; (b) Inter-plate distance measurements according to the vertical position measurements. 132

List of Tables

3.1 Coefficients of the polynomial approximation of the temperature dependance of the ultrasonic velocity in water. 72

5.1 Parameters maximum variations of cables and reference transducers. 108

5.2 Parameters maximum variations of the experienced elements. . 110

5.3 Rayleigh velocity and young modulus values of the analyzed elements. 116

High Frequency Ultrasonic Device development for Non-Destructive Post-Irradiation Examination of the RHF Fuel Element

The future HPRR LEU fuel plates will have to withstand aggressive irradiations leading to a potential swelling phenomenon. This latter induces structure modifications and impacts the initial inter-plate distance. This distance is investigated, under the access and microscopic resolution constraints, within the PERSEUS Project aiming to the development of a non-destructive ultrasonic device. With a thickness of 1 mm to be inserted into the 1.8 mm water channel width of the High flux Reactor (RHF), the device relies on two ultrasonic transducers connected to an electronic system. It allows time of flight and ultrasonic velocity estimations. The feasibility being already proved, optimizations of the components of the measurement chain and signal processing have led to a new device. A developed motorized bench has allowed reproducibility measurements corresponding to a 500 nm resolution. Then, a devices' radiation resistance experiment, carried out in the Arc-nucleart Institute, demonstrated the parameter stability under 3500 kGray. Experiments were also realized on the RHF fuel element where vertical position, distance and temperature were evaluated, with a 1 μm precision on the relative thickness variation. Future works will explore waves ability to be focused in the depth of the plates.
Key words: HPRR, RHF, ultrasonic device, radiations, signal processing.

Développement d'un dispositif ultrasonore hautes fréquences pour la caractérisation post-irradiation de l'élément combustible du RHF

Les prochaines plaques combustibles faiblement enrichies des réacteurs HPRR devront résister à de hautes radiations et dévoileront probablement un gonflement. Ce dernier modifie la structure et influence la distance inter-plaque. La mesure de celle-ci avec une précision micrométrique constitue l'objectif du projet PERSEUS via le développement d'un dispositif ultrasonore non-destructif. Réduit à 1 mm pour s'insérer dans l'interstice inter-plaque de 1.8 mm du Réacteur à Haut Flux (RHF), le dispositif comprend deux transducteurs ultrasonores reliés à un système électronique. Il permet les mesures de temps de vol et de vitesse ultrasonore. La faisabilité de mesure précédemment prouvée, des optimisations de la chaîne de mesure et du traitement du signal ont été intégrées, induisant une nouvelle génération de dispositif. Un banc motorisé a été développé et a permis des mesures de reproductibilité précises à 500 nm. La résistance aux radiations, expérimentée à l'Institut Arc-Nucléart, a démontré la stabilité des dispositifs à 3500 kGray. De plus, une expérience de mesure de distance inter-plaque sur l'élément combustible du RHF a permis les mesures de position verticale, de distance et température avec 1 μm de précision sur la variation relative de l'épaisseur du canal d'eau. Une étude de faisabilité de focalisation d'ondes est prévue pour analyser les plaques en profondeur.
Mots-clés: HPRR,RHF, système ultrason, radiation, traitement du signal.